1

7

"STUDIES OF THE SUDBURY NEUTRINO OBSERVATORY DETECTOR AND SONOLUMINESCENCE USING A SONOLUMINESCENT SOURCE"

Douglas S. McDonald

A DISSERTATION

in

PHYSICS

Presented to the Faculties of the University of Pennsylvania in Partial Fulfillment of the Requirements for the Degree of Doctor of Philosophy

1999

Eugene Beier

Supervisor of Dissertation

Nigel Lockyer

Graduate Group Chairperson

# DEDICATION

This work is dedicated to

my parents,

my wife, Sonu, and my son, Adil

**ACKNOWLEDGEMENTS** Many people contributed to the work here and especially to my overall education and training as a PhD. student in physics. This space is too short to properly convey my gratitude. Primarilly I'd like to thank the entire SNO group at Penn. My advisor, Gene Beier, has been a fountain of knowledge and his mixture of laissez-faire and hands-on tactics in training me tended to maximize my efficiency in learning the difficult material. Bill Frati has been an inspiration and showed me many of the experimental techniques I've used. Thanks to Doug Cowen, without whom the intensity interferometry experiments may never have happened. The post docs in the group, Josh Klein and Richard Van de Water, have taught me the most. It is incredible how willing they were to help at any time they were needed. Peter, Mark and Ignacio, my fellow graduate students, also taught me a lot - even though it was I who should have been teaching them! I will always remember the good times we had. The engineering group at Penn is top notch and I was lucky to have worked them. Rick Van Berg has the most amazing volume of relevant information in his mind. Mitch Newcomer has the most unique mind I'll ever know, the degree with which he understands electronics is incredible. I'll always remember to use tin foil! Paul Keener always answered my questions and solved my computer problems patiently - even when the questions were inane! Ronnie Pearce put up with my lack of forsight and organization and built me many contraptions used in the experiments. Godwin Mayers helped out with many electronics tasks. Jim Cook, Chuck Alexander, Charlie Henry and Walter Konenenko have all been very helpful and available. I'd like to thank Jean and Pauline for their assistance with travel and other issues. The Penn high energy physics group as a whole has been good to me - I thank each member. For PMTIC testing, I'd like to thank Rich Helmer at TRIUMF who kept the project going and also made it fun. Thanks also to his crew at TRIUMF. Sid Barry of Queens University helped develop the tests, Barry and Peter from Oxford worked long hours testing. Karin Hayward of Sudbury really pushed the project to completion and deserves a special mention. SNO collaborators who helped me with the experiments include: Frasier, Brice, and Richard from Queens University, Dave Wark from Oxford, Jarret Heise from UBC and many others. Finally, I'd like to thank Art McDonald and the entire SNO collaboration for all their help, friendship and kinship during my time in the collaboration. I wish them luck in their endeavors as a world class scientific experiment.

**ABSTRACT**

"STUDIES OF THE SUDBURY NEUTRINO OBSERVATORY DETECTOR AND SONOLUMINESCENCE USING A SONOLUMINESCENT SOURCE"

Douglas S. McDonald

Eugene Beier

The Sudbury Neutrino Observatory (SNO) is the first heavy water Cerenkov solar neutrino detector. 1000 metric tonnes of heavy water is used as a neutrino target and detection medium. SNO is designed to measure the flux and energy spectrum of high energy solar electron neutrinos via charged current interactions of electron neutrinos with deuterons in the heavy water. SNO can also measure the total high energy solar neutrino flux of neutrinos of all flavors via neutral current interactions with deuterons. These measurements have the potential to provide direct evidence of neutrino oscillations in the solar neutrino sector. The physics of solar models and solar neutrinos is presented. The physics of SNO and the SNO detector are described in detail.

Two sonoluminescence sources were developed for use in calibrations of the SNO detector. The sonoluminescence source outperformed the standard SNO optical source, a nitrogen laser with a diffuser ball, by 25% in measurements of photomultiplier tube timing accuracy. Two systematic effects with the SNO electronics were discovered. Electronic crosstalk between channels, although not unexpected, has been

measured for charges greater than 5 photoelectrons. An efficient cut has been developed to minimize this systematic error with an upper limit on signal loss of 0.4% times the PMT occupancy. Electronics crosstalk will affect solar neutrino analyses as it falsely adds PMT hits to some fraction of the events. The effect is small, as solar neutrino events have low detector occupancy and relatively small PMT charges. A small anticorrelation of photomultiplier charges for electronics channels in close proximity has been measured. It has been shown that this subtle effect does not affect the number of photons detected, only the photomultiplier charges - it will not affect solar neutrino analyses.

A SL source and the SNO detector were used to study fundamental aspects of sonoluminescence. Three properties of sonoluminescence have been studied. An analysis of SL data with regard to back-to-back photon correlations is presented. The results are consistent with no back-to-back photon correlations with an upper limit on the strength of back-to-back photon correlations of 3.16% for unfiltered SL light, and 0.5% for filtered SL light ($\lambda = 420 \pm 10$ nm) at the 95% confidence level. These limits can be interpreted as limits on the percentage of photon pairs which have back-to-back correlations. The SL photon angular distribution has been measured using angular correlation functions. Attempts to fit the data to distributions with: 1) a small dipole component, and 2) a coherent sum of a dipole and a quadrupole, give poor fits. The best fit yields significant dipole and quadrupole strengths of $(1.80 \pm 0.14)$%

and $(0.16 \pm 0.03)\%$ respectively. Higher order multipole components are necessary for a better fit to the data. The angular distribution may be due to complex bubble motions rather than motions of charges in the bubble interior [1]. Intensity interferometry, the method of Hanbury Brown and Twiss, has been used to attempt a measurement of the size of the light emitting region of a SL bubble. The angular correlation distributions at three different wavelengths, $\lambda = 420 \pm 10$ nm, $334 \pm 10$ nm and $487 \pm 1$ nm, are all consistent with uncorrelated signals. A fit of the $\lambda = 420 \pm 10$ nm correlation distribution to a model of SL intensity interferometry [2] has been carried out. A small region of paramter space is excluded by the results at the 95% confidence level: $\tau_{SL} < 2.5ps$ for $R_{SL} = 200nm$ and $\tau_{SL} < 0.35ps$ for $R_{SL} = 500nm$. Here, $\tau_{SL}$ and $R_{SL}$ are the sonoluminescence pulse width and spot size (light emitting region of the SL bubble) respectively. The excluded region of parameter space does not place any new limitations on the parameters $\tau_{SL}$ and $R_{SL}$.

**Contents**

**1 Introduction** **1**

1.1 The Solar Neutrino Problem . . . . . . . . . . . . . . . . . . . . . . . 3

1.1.1 Stellar Evolution and Standard Solar Models . . . . . . . . . . 4

1.1.2 Solar Neutrino Experiments . . . . . . . . . . . . . . . . . . . 8

1.2 Possible Explanations of the Solar Neutrino Deficit . . . . . . . . . . 14

1.2.1 Are The Solar Models Or Experiments Wrong? . . . . . . . . 14

1.2.2 Neutrino Oscillations . . . . . . . . . . . . . . . . . . . . . . . 16

1.3 The role of SNO . . . . . . . . . . . . . . . . . . . . . . . . . . . . . 23

1.4 SL and SNO . . . . . . . . . . . . . . . . . . . . . . . . . . . . . . . 24

1.5 Sonoluminescence . . . . . . . . . . . . . . . . . . . . . . . . . . . . 24

1.5.1 Discovery and History of SL . . . . . . . . . . . . . . . . . . . 25

1.5.2 Characterization of SL . . . . . . . . . . . . . . . . . . . . . . 26

1.6 SL Theory . . . . . . . . . . . . . . . . . . . . . . . . . . . . . . . . 30

1.6.1 Classical physics SL theories . . . . . . . . . . . . . . . . . . . 31

1.6.2 QED SL theories . . . . . . . . . . . . . . . . . . . . . . . . . 34

1.6.3 Comparison of the QED or Casimir models . . . . . . . . . . . 39

1.7 Outline of this thesis . . . . . . . . . . . . . . . . . . . . . . . . . . . . 40

**2 The SNO Detector** **42**

2.1 A Brief Description of the SNO Detector . . . . . . . . . . . . . . . . 42

2.2 Acrylic Vessel . . . . . . . . . . . . . . . . . . . . . . . . . . . . . . . 45

2.3 PMT Support Structure . . . . . . . . . . . . . . . . . . . . . . . . . 46

2.4 Photomultiplier Tubes . . . . . . . . . . . . . . . . . . . . . . . . . . 47

2.5 Heavy and Light Water Systems . . . . . . . . . . . . . . . . . . . . . 48

2.5.1 Filtering and Monitoring . . . . . . . . . . . . . . . . . . . . . 49

2.5.2 Salt Addition/Removal . . . . . . . . . . . . . . . . . . . . . . 50

2.5.3 Cover Gas System . . . . . . . . . . . . . . . . . . . . . . . . 51

2.6 Electronics . . . . . . . . . . . . . . . . . . . . . . . . . . . . . . . . . 51

2.6.1 High Voltage System . . . . . . . . . . . . . . . . . . . . . . . 54

2.6.2 Signal Processing . . . . . . . . . . . . . . . . . . . . . . . . . 55

2.6.3 Trigger System . . . . . . . . . . . . . . . . . . . . . . . . . . 57

2.7 Data Acquisition System . . . . . . . . . . . . . . . . . . . . . . . . . 59

2.8 Calibrations . . . . . . . . . . . . . . . . . . . . . . . . . . . . . . . . 60

2.8.1 Calibration Source Manipulator System . . . . . . . . . . . . . 60

2.8.2 Electronics Calibrations . . . . . . . . . . . . . . . . . . . . . 61

2.8.3 Optical Calibrations . . . . . . . . . . . . . . . . . . . . . . . 62

2.8.4 Energy Calibrations . . . . . . . . . . . . . . . . . . . . . . . 63

2.8.5 Electron and Neutron Response Calibrations . . . . . . . . . . 64

2.8.6 Angular Resolution . . . . . . . . . . . . . . . . . . . . . . . . 66

2.9 Detector and Physics Monte Carlo Simulations: SNOMAN . . . . . . 66

2.10 Summary . . . . . . . . . . . . . . . . . . . . . . . . . . . . . . . . 67

**3 Sonoluminescence: Experimental and Theoretical Methods 68**

3.1 SL Sources . . . . . . . . . . . . . . . . . . . . . . . . . . . . . . . . 69

3.2 SL Source Operation . . . . . . . . . . . . . . . . . . . . . . . . . . 71

3.3 SL Data: A First Look . . . . . . . . . . . . . . . . . . . . . . . . . 74

3.3.1 NHIT and NHIT vs. Time . . . . . . . . . . . . . . . . . . . . 74

3.3.2 Time Interval Between Events . . . . . . . . . . . . . . . . . . 80

3.3.3 PMT Hit Time and Charge . . . . . . . . . . . . . . . . . . . 80

3.3.4 SL Data With Combined Cuts . . . . . . . . . . . . . . . . . . 86

3.4 PMT Timing Residuals . . . . . . . . . . . . . . . . . . . . . . . . . 87

3.5 Photon Correlation Functions . . . . . . . . . . . . . . . . . . . . . 92

3.5.1 Dynamic Correlation Functions . . . . . . . . . . . . . . . . . 93

3.5.2 Static Correlation Functions . . . . . . . . . . . . . . . . . . . 99

3.5.3 Monte Carlo Comparison of Static and Dynamic Correlation Functions . . . . . . . . . . . . . . . . . . . . . . . . . . . . . 100

3.5.4 Laserball and Sonoluminescence Static Correlation Functions . 103

3.5.5 Time Autocorrelation Functions . . . . . . . . . . . . . . . . . 103
3.5.6 Electronics Channel Correlation Functions . . . . . . . . . . . 106
3.6 Applying Photon Correlations to Fundamental SL Investigations . . . 107
3.6.1 Back-to-Back Photon Correlations . . . . . . . . . . . . . . . . 108
3.6.2 Angular Distribution of Photons . . . . . . . . . . . . . . . . . 109
3.6.3 Intensity Interferometry: Measuring the Spot Size of SL . . . 111
3.7 Summary . . . . . . . . . . . . . . . . . . . . . . . . . . . . . . . . 118

**4 Angular Distribution and Angular Correlations 119**

4.1 Introduction . . . . . . . . . . . . . . . . . . . . . . . . . . . . . . 119
4.2 Systematic Studies Using the Laserball . . . . . . . . . . . . . . . . 120
4.2.1 Electronic Cross Talk . . . . . . . . . . . . . . . . . . . . . . . 123
4.2.2 Daughter Card Charge Anticorrelation . . . . . . . . . . . . . 127
4.2.3 Comparison of LB Data With PMT Hit and Charge Correlation Functions . . . . . . . . . . . . . . . . . . . . . . . . . . . . 133
4.2.4 Laserball Time Correlations . . . . . . . . . . . . . . . . . . . 135
4.2.5 Discussion of the Systematic Effects . . . . . . . . . . . . . . . 138
4.3 Back-To-Back Photon Correlations . . . . . . . . . . . . . . . . . . 139
4.3.1 Monte Carlo Studies . . . . . . . . . . . . . . . . . . . . . . . 139
4.3.2 Systematic Error Estimation . . . . . . . . . . . . . . . . . . . 145
4.3.3 Experimental Results . . . . . . . . . . . . . . . . . . . . . . . 146

4.3.4 Fits To the Data . . . 148

4.4 Angular Distribution of SL Photons . . . 151

4.4.1 Monte Carlo Studies of Angular Distributions . . . 154

4.4.2 Experimental Results . . . 156

4.4.3 Discussion of Angular Distribution Experimental Results . . . 164

4.5 Intensity Interferometry: The Method of Hanbury-Brown and Twiss . 164

4.5.1 MC Simulations of Intensity Interferometry . . . 165

4.5.2 Experimental Results . . . 168

4.5.3 Systematic Checks . . . 172

4.5.4 Quantitative Results For SL Intensity Interferometry . . . 181

4.6 Summary and Discussion of Results . . . 185

**5 Conclusions 187**

5.1 Sonoluminescence Studies of the SNO Detector . . . 187

5.2 Fundamental SL Investigations . . . 189

5.3 Future Work and Experiments . . . 191

**A SNO Neutrino Physics 193**

A.1 Scientific Motivation . . . 193

A.2 Neutrino Interactions In SNO . . . 195

A.2.1 CC Interaction . . . 195

A.2.2 NC Interaction . . . . . . . . . . . . . . . . . . . . . . . . . . 197

A.2.3 ES Interactions . . . . . . . . . . . . . . . . . . . . . . . . . . 202

A.2.4 $\overline{\nu_e}$ Interactions . . . . . . . . . . . . . . . . . . . . . . . . . . 203

A.3 Distinguishing The Interactions . . . . . . . . . . . . . . . . . . . . . . 204

A.4 Sources of Background . . . . . . . . . . . . . . . . . . . . . . . . . . 205

A.4.1 Backgrounds To CC Events . . . . . . . . . . . . . . . . . . . . 206

A.4.2 Backgrounds To NC Events . . . . . . . . . . . . . . . . . . . . 207

A.4.3 Muons . . . . . . . . . . . . . . . . . . . . . . . . . . . . . . . . 208

A.5 SNO Physics . . . . . . . . . . . . . . . . . . . . . . . . . . . . . . . . 209

A.6 Summary of SNO Physics . . . . . . . . . . . . . . . . . . . . . . . . . 214

**B The SNO PMT Interface and High Voltage System 215**

B.1 Design Criteria . . . . . . . . . . . . . . . . . . . . . . . . . . . . . . . 216

B.2 PMT Interface Card (PMTIC) . . . . . . . . . . . . . . . . . . . . . . . 218

B.2.1 High Voltage Path . . . . . . . . . . . . . . . . . . . . . . . . . 221

B.2.2 PMT Base Current . . . . . . . . . . . . . . . . . . . . . . . . . 223

B.2.3 Signal Path . . . . . . . . . . . . . . . . . . . . . . . . . . . . . 224

B.2.4 Charge Injection . . . . . . . . . . . . . . . . . . . . . . . . . . 225

B.3 High Voltage Backplane (HVBP) . . . . . . . . . . . . . . . . . . . . . 226

B.4 HV Power Distribution and Architecture . . . . . . . . . . . . . . . . . 227

B.5 Outward Looking PMTs . . . . . . . . . . . . . . . . . . . . . . . . . . 228

B.6 Low Gain PMT Channel Modification . . . . . . . . . . . . . . . . . 229

B.7 Testing . . . . . . . . . . . . . . . . . . . . . . . . . . . . . . . . . . . 230

B.7.1 PMTIC Testing . . . . . . . . . . . . . . . . . . . . . . . . . . 230

B.7.2 System Testing . . . . . . . . . . . . . . . . . . . . . . . . . . 232

B.8 PMTIC and HV System Performance . . . . . . . . . . . . . . . . . . 232

## List of Figures

1.1 Bahcall-Pinsonneault SSM (1998) predictions of the neutrino energy spectra . . . . . . . . . . . . . . . . . . . . . . . . . . . . . . . . . . . 7

1.2 Bahcall-Pinsonneault SSM (1998) comparison of expected event rates with measured rates for five neutrino experiments. Theoretical and experimental uncertainties are shown and cannot explain the discrepancy 11

1.3 Results of a model independent analysis where global fits of the event rates of four major neutrino experiments were fit to the predictions from the Bahcall-Pinsonneault SSM (1995) with the fluxes left as free parameters. Shown are the 90% confidence level inclusion regions of the $^{8}$B vs $^{7}$Be fitted flux plotted for each experiment. It is seen that there is a very small region of agreement at 0.34 on the y-axis and 0 on the x-axis . . . . . . . . . . . . . . . . . . . . . . . . . . . . . . . 13

1.4 Combined fit of data from all experiments to the vacuum oscillation hypothesis where the 95% contours are shown . . . . . . . . . . . . . 20

1.5 Combined fit of data from all experiments to the MSW oscillation hypothesis over the range of parameter space relevant to solar neutrino energies. The inclusion regions for each experiment as well as the combined result 95% confidence level contours are shown . . . . . . . 21

2.1 Schematic diagram of the SNO detector . . . . . . . . . . . . . . . . 43

2.2 Schematic diagram of the SNO electronics and data acquisition system. 52

3.1 The water fill SL source. Note the outer acrylic shell to keep the inner flask away from the heavy water. The peizo-electric crystals are shown on the right and left hand sides of the equator on the inner flask. . . 70

3.2 SL Experimental Setup . . . . . . . . . . . . . . . . . . . . . . . . . . 72

3.3 SL Run 179: Raw NHIT Distribution. The dotted line represents the NHIT threshold setting. . . . . . . . . . . . . . . . . . . . . . . . . . . 75

3.4 SL Run 179: Raw NHIT vs. Time (min.) . . . . . . . . . . . . . . . . 75

3.5 SL Run 1279 unfiltered light, full detector - $NHIT$ vs. $t_{event}$. Source could not be properly degassed before the run resulting in bubble-, and therefore intensity-, instability. . . . . . . . . . . . . . . . . . . . . . . . 81

3.6 SL Run 179: Time between events, $\Delta t_{event}$ in $msec$. If adjacent events occur with $\Delta t \neq 1000\tau_{SL}$ then they can be cut as they are probably not SL events. . . . . . . . . . . . . . . . . . . . . . . . . . . . . . . . . 82

3.7 SL Run 179: PMT hit time (ns) with arbitrary time offset. Note the direct and reflected light peaks. . . . . . . . . . . . . . . . . . . . . . . 84

3.8 SL Run 179: PMT Charge (QHL) in pedestal subtracted ADC counts. There are approximately 40 ADC counts per photoelectron. . . . . . 85

3.9 SL Run 179: NHIT Distribution for $11min. < Event\ \ Time < 16min.$ after NHIT cuts. Also shown is a Gaussian fit and fit parameters. The $\chi^2$ per degree of freedom is just less than 1. The ratio of the fit deviation to the square root of the mean is: $\sigma/$ . . . . . . . . . . . . . 87

3.10 PMT time residuals for the LB (solid histogram) and SL source (dashed histogram). (The author thanks Bill Frati for the use of this plot.) . . 90

3.11 Reconstructed x, y and z position residuals for the LB (solid histogram) and SL source (dashed histogram). The results of the Gaussian fits to these histograms are shown in table 3.1. (The author thanks Bill Frati for the use of this information.) . . . . . . . . . . . . . . . . . . . . . . 91

3.12 SNOMAN SL Monte Carlo simulation of a 23.1% stationary dipole. Shown are the "dynamic" and "stationary" same event (SE) correlation analyses. It is seen that the dynamic analysis shows no correlation. . 101

3.13 SNOMAN SL Monte Carlo simulation of a 10% dynamic dipole. Shown are the "dynamic" and "stationary" same event (SE) correlation analyses. Both correlation functions detect the dipole. . . . . . . . . . . . 102

3.14 LB run 996 and SL run 179 “static” same event correlation functions. The LB static angular distribution is far less isotropic than that of the SL source. . . . . . . . . . . . . . . . . . . . . . . . . . . . . . . . . . 104

4.1 Laserball Run 996: “PMT hit” and “charge” same event correlation functions. Note the slight positive correlation for the PMT hit SE function and the anticorrelation of the charge SE function at small angles. Also note the 0.4% positive correlation offset at all angles. . . 122

4.2 Laserball run 996: $QHL_{min}$ vs. $QHL_{max}$ for all photon coincidences in: adjacent electronics channels (top plot), and adjacent PMTs which are not in adjacent electronics channels (bottom plot). The cross talk region at low charge is populated in the top plot, but not in the bottom plot. . . . . . . . . . . . . . . . . . . . . . . . . . . . . . . . . . . . . 125

4.3 Laserball run 996: A closeup of the top plot in Figure 4.2 showing the separation of the crosstalk background from the signal. The crosstalk cut line is shown. The smaller of the two charges from entries below and to the right of the cut line are discarded. . . . . . . . . . . . . . . 126

4.4 Laserball run 996: Similar to Figures 4.2 and 4.3 but using QHL pedestal subtracted ADC counts for the charge rather than calibrated charge. The top plot shows the uncut signal plus crosstalk background and the bottom plot has the crosstalk cut applied. The number of entries on each plot can be used to calculate that 2.8% of the PMT hits that were cut. . . . . . . . . . . . . . . . . . . . . . . . . . . . . . 128

4.5 Laserball run 996: Similar to Figure 4.4 but with next-to-adjacent channels rather than adjacent channels. The units of charge on both axes are pedestal subtracted ADC counts. The number of entries in each plot can be used to calculate that 0.4% of the PMT hits were cut. 129

4.6 Laserball run 996: SE Correlation functions vs. $\Delta channel$, the difference between the channel numbers of two given electronics channels. This is done for "same daughter card" (or "same DB") coincidences (filled circles), "same SNOD discriminator chip" coincidences (open diamonds), "adjacent SNOD chip, same daughter card" coincidences (large X's) and "adjacent daughter card" (or "adjacent DB") coincidences (open triangles). All SE functions show an anticorrelation except the adjacent daughter card case which is consistent with the 0.4% positive correlation offset mentioned above. . . . . . . . . . . . . 131

4.7 LB run 996 and a SNOMAN SL Monte Carlo simulation of the daughter card systematic. The results show good agreement between the simulation and the data but for the 0.4% positive correlation offset which will be discussed further below. . . . . . . . . . . . . . . . . . . . 132

4.8 LB Run 996: PMT hit and charge SE correlation functions before and after the crosstalk cut is applied. Note that after the crosstalk cut is applied, the PMT hit SE function is consistent with a uniform distribution at all angles. . . . . . . . . . . . . . . . . . . . . . . . . . . 134

4.9 Laserball run 996: Same event and different events dynamic PMT hit correlation functions after the crosstalk cut has been made. Note that both functions are flat over the entire angular range but that the SE function has a positive correlation offset while the DE function does not. 136

4.10 LB Run 996: Time autocorrelation function for the LB. It is seen that intensity fluctuations occur with a period of approximately $150 - 200$ *msec* and a *correlation* amplitude of $\sim 3.5\%$. The actual amplitude of the intensity fluctuations is measured to be 9.5%. . . . . . . . . . . . 137

4.11 SNOMAN SL Monte Carlo simulation of 100%, 44%, 17% and 2% back-to-back pairs of photons. . . . . . . . . . . . . . . . . . . . . . . . 140

4.12 SNOMAN SL Monte Carlo simulation of 100% back-to-back pairs of photons. The effect of Fresnel scattering, Fresnel + Rayleigh scattering, acrylic vessel (AV) absorption and PMT quantum efficiency on the correlation are shown. . . . . . . . . . . . . . . . . . . . . . . . . . 142

4.13 SNOMAN SL Monte Carlo simulation of 100% back-to-back pairs of photons. Moving the SL source away from the detector center while assuming it is at the center in analysis causes a spread in the correlation. When the analysis uses the correct source location, most of the spreading disappears. . . . . . . . . . . . . . . . . . . . . . . . . . . . 144

4.14 SL Run 179: Same event and different events dynamic PMT hit correlation functions with unity subtracted and normalized by the correlation at zero lag. Aside from the positive correlation offset, which is due to intensity fluctuations of the SL light, no significant back-to-back correlations are seen. . . . . . . . . . . . . . . . . . . . . . . . . . . . 147

4.15 SL Run 1267: Same event and different events dynamic PMT hit correlation functions with unity subtracted and normalized by the correlation at zero lag. No significant back-to-back correlations are seen. . 149

4.16 SNOMAN SL Monte Carlo simulation of 40%, 30%, 20% and 10% back-to-back pairs of photons with all photon collection inefficiencies included. The source location is $(x, y, z) = (10cm, -25cm, 0cm)$ in detector coordinates which is the reconstructed location of the source for the SL data sets described below. . . . . . . . . . . . . . . . . . . 150

4.17 $\chi^2$ from a least squares fit of the last 5 data points of the SE correlation function from SL run 179 to Monte Carlo simulations of the effect. The strength of the correlation, or equivalently, the percentage of correlated pairs, is the fitting parameter. The 95% confidence level upper limit of the strength of correlated photon pairs is shown with a thick dot-dased line. . . . . . . . . . . . . . . . . . . . . . . . . . . . . . . . . . . . . 152

4.18 $\chi^2$ from a least squares fit of the last 5 data points of the SE correlation function from SL run 1267 ($\lambda = 420 \pm 10$ nm) to Monte Carlo simulations of the effect. The strength of the correlation, or equivalently, the percentage of correlated pairs, is the fitting parameter. The 95% confidence level upper limit of the strength of correlated photon pairs is shown with a thick dot-dased line. . . . . . . . . . . . . . . . . . . 153

4.19 SNOMAN SL Monte Carlo simulation of a 10% "dynamic" dipole. Shown are the same event (SE) and different events (DE) correlation functions and a fit. . . . . . . . . . . . . . . . . . . . . . . . . . . . . 155

4.20 The best fit point and $1\sigma$ and $3\sigma$ error ellipses for the fit in the above plot are shown. The generated values are denoted by where the horizontal and vertical dashed lines cross. . . . . . . . . . . . . . . . . . . 155

4.21 SNOMAN SL Monte Carlo simulation of a 10% "dynamic"quadrupole. Shown are the same event (SE) and different events correlation functions and a fit. . . . . . . . . . . . . . . . . . . . . . . . . . . . . . . . 157

4.22 Best fit, $1\sigma$ and $3\sigma$ error ellipses for the fit in the above plot are shown. The generated values are denoted by where the horizontal and vertical dashed lines cross. . . . . . . . . . . . . . . . . . . . . . . . . . . . . . 157

4.23 SNOMAN SL Monte Carlo simulation of a "dynamic", coherently summed, 5% dipole and 5% quadrupole angular distribution. The same event (SE) and different events (DE) correlation functions and a fit are shown. . . . . . . . . . . . . . . . . . . . . . . . . . . . . . . . 158

4.24 Best fit, $1\sigma$ and $3\sigma$ error ellipses for the fit in the above plot are shown. The generated values are denoted by where the horizontal and vertical dashed lines cross. . . . . . . . . . . . . . . . . . . . . . . . . . . . . . 158

4.25 SL Run 179: Same event and different events dynamic correlation functions. . . . . . . . . . . . . . . . . . . . . . . . . . . . . . . . . . . . . 160

4.26 SL Run 179: Corrected same event and adjacent events dynamic correlation functions. Note that the AE correlation function is uniform while the SE function is not. . . . . . . . . . . . . . . . . . . . . . . . 161
4.27 SL Run 1279: Same event dynamic correlation function for the "stable" portion of the run ($t_{event} < 3min.$, see Figure 3.5 in Chapter 3). . . . 163
4.28 Analysis of two SL Bose-Einstein MCs - with and without Bose-Einstein correlations. . . . . . . . . . . . . . . . . . . . . . . . . . . . . . . . . 166
4.29 Analysis of a SL Bose-Einstein MC - SL spot size dependence. . . . . 167
4.30 Analysis of a SL Bose-Einstein MC - wavelength dependence. . . . . . 167
4.31 Run 1267: 3D Histogram of Nhit vs. $\theta_{detector}$ vs. $\phi_{detector}$ showing the regions of unfiltered light and regions of filtered light as well as some noise. . . . . . . . . . . . . . . . . . . . . . . . . . . . . . . . . . . . . 169
4.32 Top view of Figure 4.31 for clarity. . . . . . . . . . . . . . . . . . . . . 169
4.33 SE and DE vs. $\alpha$ for the 334±10 nm BP filter data set. . . . . . . . . 173
4.34 SE and DE vs. $\alpha$ for the 420±10 nm BP filter data set. . . . . . . . . 174
4.35 SE and DE vs. $\alpha$ for the 487±1 nm BP filter data set. . . . . . . . . 175
4.36 Corrected SE function vs. $\alpha$ for the 334±10 nm BP filter data set. . . 176
4.37 Corrected SE function vs. $\alpha$ for the 420±10 nm BP filter data set. . . 177
4.38 Corrected SE function vs. $\alpha$ for the 487±1 nm BP filter data set. . . 178

4.39 A comparison of the $420 \pm 10$ nm data sets fromm SL filter runs 1267 and 1270. The SE correlation functions of the data sets from the two runs are consistent with each other. . . . . . . . . . . . . . . . . . . . 180

4.40 SL Filter Run 1267 - 420$\pm$10 nm filter comparison . . . . . . . . . . . 182

4.41 SL Filter Run 1267 - filter comparison . . . . . . . . . . . . . . . . . 183

4.42 A fit to a theoretical model . . . . . . . . . . . . . . . . . . . . . . . . 184

A.1 Energy response of the SNO detector to 5 MeV neutrinos with the CC interaction. The figure was obtained using the SNOMAN Monte Carlo generator. . . . . . . . . . . . . . . . . . . . . . . . . . . . . . . . . . . 196

A.2 Energy response of the SNO detector to 5 MeV neutrinos with the ES interaction in the heavy water. The figure was obtained using the SNOMAN Monte Carlo generator. . . . . . . . . . . . . . . . . . . . . . 203

A.3 SNO expected $\nu_e$spectrum distortion for various solar neutrino problem solutions . . . . . . . . . . . . . . . . . . . . . . . . . . . . . . . . . 212

A.4 SuperK expected $\nu_e$spectrum distortion for various solar neutrino problem solutions . . . . . . . . . . . . . . . . . . . . . . . . . . . . . . . 212

**List of Tables**

7

3.1 Comparison of the timing calibration reconstruction performed with the laserball (LB) and SL sources. Reconstructed coordinates are measured in cm and the time in ns. The uncertainties are shown.(The author thanks Bill Frati for the use of this information.) . . . . . . . 92

4.1 SL Filter Run 1267: event cuts and statistics. . . . . . . . . . . . . . 171

A.1 SNO neutrino interactions and physics. The cross sections at 10 MeV neutrino energy are given. . . . . . . . . . . . . . . . . . . . . . . . . . 196

# Chapter 1

# Introduction

The Sudbury Neutrino Observatory (SNO) is the first heavy water Cerenkov neutrino detector. Using heavy water as a neutrino target allows SNO to measure both the electron neutrino flux as well as the total flux of all active solar neutrino flavors. If the electron neutrinos, which are born in the nuclear fusion cycle in the sun, transform to another type of active neutrino on their way to the earth, the electron neutrino flux will be less than the total neutrino flux in some energy interval. A deficit of solar neutrinos compared to predictions from solar models has been seen by five previous experiments [3, 4, 5, 6, 7]. Such a result would be conclusive evidence for neutrino "flavor" transformation, also called neutrino oscillations. A positive neutrino oscillation result implies that at least one flavor of participating neutrino has non-zero mass.

The construction for SNO started in 1990 at Inco Ltd.'s Creighton Mine near Sudbury, Ontario, Canada. The construction phase ended in November 1998 and the first solar neutrino data was taken in May, 1999. Due to construction delays, it was not possible for the author to study solar neutrinos. Instead, a sonoluminescent light source has been used to study both the SNO detector as well as the phenomenon of sonoluminescence itself.

"Sonoluminescence" (SL) is the creation of light from sound energy. The physical process by which this comes about is not yet fully understood. SL was discovered in 1934 by Frenzel and Schultz [8] who found that light was emitted erratically by cavitation air bubbles in water. Unfortunately, the phenomenon was not stable and further study was impeded. This situation did not change until 1990 when Philip Gaitan and Lawrence Crum [9, 10] were able to find a way to get predictable, stable sonoluminescence with a single air bubble. This will be referred to as "Single Bubble Sonoluminescence" (SBSL). Since SBSL was discovered, many experimenters have studied the phenomenon trying to shed light on the physical mechanism. Those efforts have been quite successful, but are incomplete.

This chapter will motivate both the construction of the Sudbury Neutrino Observatory and the study of sonoluminescence. Section 1.1 will discuss the solar neutrino problem including the standard solar models and the experiments built to test them. Shortcomings of these experiments will be pointed out. Possible explanations of the solar neutrino problem will be discussed in Section 1.2. In Section 1.3 the Sudbury Neutrino Observatory experiment, which was designed to address the shortcomings of the first generation of neutrino detectors, will be discussed.

In the course of development of the construction of SNO, we observed that sonoluminescence could be used to calibrate the SNO detector. Later it appeared that the SNO detector could be used to study sonoluminescence itself. Section 1.4 will discuss the relationship between the Sudbury Neutrino Observatory and sonoluminescence. Section 1.5 describes the discovery, history and some of the experiments done to understand sonoluminescence. Section 1.6 will briefly discuss some theories of the mechanism of SL light emission. Experiments were undertaken as part of this thesis in order to test certain predictions of some of these theories. The final section, Section 1.7, will present the outline of this thesis.

## 1.1 The Solar Neutrino Problem

The solar neutrino problem was identified through the pioneering experiments carried out by Ray Davis at the Homestake Gold Mine in South Dakota, USA [11]. The problem is roughly 30 years old and is still unsolved. At that site, Davis built the first solar neutrino detector, using $^{37}Cl$ in perchlorethylene as a neutrino target, and made the first measurements of the solar neutrino flux. At the same time, theoretical studies of solar neutrinos were undertaken by John Bahcall. Bahcall calculated predictions for the solar neutrino flux from a computer model simulating the stellar evolution of the sun [12]. Davis' "Homestake" or "Chlorine" ($Cl$) neutrino detector was used to make many measurements of the solar neutrino flux, all of which disagreed with predictions. There was a deficit of neutrinos: only about one third of the predicted neutrinos reached the *Cl* detector. Many systematic checks have been performed in the 30 years the experiment has operated. The deficit seems robust. Much effort has been spent developing and refining the solar models. The result is that the solar models cannot be adjusted to account for the experimental results. This discrepancy has come to be known as the "solar neutrino problem". Four other major solar neutrino experiments, some of which have totally different means of detecting neutrinos and cover different energy regimes, all show a deficit compared to the solar models. These experiments and their results will be discussed later in this chapter.

### 1.1.1 Stellar Evolution and Standard Solar Models

The sun can be modeled in a fairly simple way as it is early in the main sequence [13, 12, 14, 15]. As a result, most of its mass is made up of hydrogen which has yet to be fused to helium or heavier elements. In addition, the fusion process is happening very slowly. This section will briefly describe the manner in which stars, specifically the sun, are modeled. For more in depth information see the references [13, 12, 14, 15].

The primary assumptions of standard solar models (SSMs) are that the sun is spherically symmetric, and is in quasi-static equilibrium with no convection. Rotation, mass loss and magnetic fields are not considered. Hydrostatic equilibrium is maintained by the balance between nuclear energy generation and gravitational energy. The energy transport and pressure are calculated as functions of the density, temperature and opacity, all of which depend on the radial position in the sun. Both the radiative and the dominant thermal components of the pressure are included. Finally, the nuclear energy generation mechanism is modeled.

The observed luminosity is the integral of the local energy generation over the entire star. In order to model the nuclear energy generation, all of the possible nuclear reactions that take place in the sun have to be understood. This is discussed below.

Many different nuclei contribute to nuclear fusion reactions in the sun. The overall effect of fusion in the sun is to fuse four protons into an alpha particle, two positrons, two electron neutrinos plus photons:

$$4p \longrightarrow \alpha + 2e^{+} + 2\nu_e. \tag{1.1}$$

There are two main branches of reactions. The most important branch for neutrino physics is the pp chain. It is responsible for the vast majority of the sun's energy as well as for solar neutrinos, including the highest energy $^{8}$B neutrinos which some of the experiments are sensitive to exclusively. The other branch is the CNO branch which was the original fusion chain discussed by Bethe in the first paper delineating the fusion physics of the sun [16].

The rate of each of the nuclear reactions must be calculated and the results integrated over the entire sun in order to predict the neutrino fluxes. In order to calculate the rates, the fusion cross sections of each reaction must be known. Fusion cross sections are difficult to measure at the low (keV) average energies of the particles in the solar interior. The rates are so small at these energies that laboratory experiments cannot measure the cross sections. The cross sections are measured at energies above a few hundred keV and extrapolated to low energies according to theoretical considerations.

All of the tools that are needed to calculate a solar model have now been specified. The model assumes initial elemental abundances and evolves the equations over time. The end result must agree with well measured solar parameters (*e.g.* solar mass, radius, luminosity and surface temperature). An iterative procedure is used to achieve this agreement. Computer codes have been written to perform these complex solar model calculations. Some of these codes are available publicly over the Internet [1].

**Predictions of Solar Neutrino Fluxes**

Standard solar models (SSMs) make predictions about the density, temperature, neutrino and photon production profiles and elemental abundances as functions of the radius of the sun, and calculate the luminosity and neutrino fluxes as functions of energy. For the purposes of this thesis, only neutrino fluxes will be discussed.

Table 1.1 shows the predictions of the solar neutrino fluxes from the Bahcall-

[1] see John Bahcall's web page: http://www.sns.ias.edu/~jnb/ .

| Solar Neutrino Type | Flux $10^{10} cm^{-2} sec^{-1}$ |
|---|---|
| pp | $5.94(\pm 1\%)$ |
| $^{7}Be$ | $4.80 \times 10^{-1}(\pm 9\%)$ |
| $^{8}B$ | $5.15 \times 10^{-4}(^{+19\%}_{-14\%})$ |
| hep | $2.10 \times 10^{-7}$ |

Table 1.1: Bahcall-Pinsonneault SSM (1998) predictions of some important neutrino fluxes in the pp chain [17]. (From John Bahcall's web page: http://www.sns.ias.edu/∼jnb/ .)

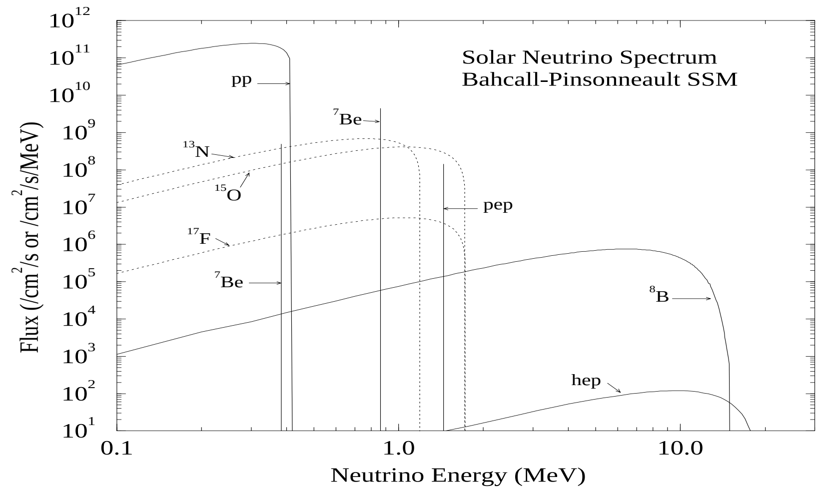


Figure 1.1: Bahcall-Pinsonneault SSM (1998) predictions of the neutrino energy spectra [17]. (From John Bahcall's web page: http://www.sns.ias.edu/∼jnb/ .)

Pinsonneault SSM (1998) [17] for some of the neutrino types in the pp chain and figure 1.1 shows a plot of the neutrino energy spectra. These are the fundamental results obtained from the SSMs as pertains to neutrino astrophysics. It is seen from these figures that the dominant neutrinos are the pp neutrinos but that they cut off at a relatively low energy. Due to the low endpoint energy of pp neutrinos, most (but not all) experiments cannot detect them. The neutrinos from the CNO chain are also shown and it is seen that they contribute at fairly low energies (below 2MeV). Finally, the highest energy neutrinos of consequence are the $^{8}$B neutrinos which extend up to 15MeV. All solar neutrino detectors can detect them. "hep" neutrinos are predicted to have a very small flux.

### 1.1.2 Solar Neutrino Experiments

There are five major solar neutrino experiments that have measured solar neutrino fluxes above their energy thresholds. All of these experiments are located deep underground. This is to decrease the cosmic ray induced background to neutrino events. Solar neutrino experiments can be classified into two categories: radiochemical and direct counting experiments. These will be described individually below.

**Radiochemical Experiments**

Radiochemical experiments detect neutrinos through inverse beta decay of a nucleus caused by a neutrino interaction. A general equation describing the reaction is:

$$\nu_e + (Z, A) \longrightarrow (Z+1, A)^* + e^-. \tag{1.2}$$

The product nucleus is radioactive and decays via electron capture emitting an Auger electron in the process. These product radioisotopes are removed periodically from the target medium with high efficiency using well known and tested chemical techniques. The Auger electron has low energy and can be detected in a small proportional counter. The number of Auger electrons measured determines the number of neutrino interactions that took place when detection efficiencies are accounted for. Given the cross section of the neutrino interaction, this is a measure of the neutrino flux.

The major radiochemical experiments are the Chlorine experiment [11] in the Homestake Mine, South Dakota, USA, SAGE (Soviet American Gallium Experiment) [18] in the Caucasus mountains of Russia and GALLEX [19] in the Gran Sasso Laboratory, Italy. The latter two experiments used Gallium ($^{71}$Ga) as a neutrino target medium - SAGE in liquid form and GALLEX in solid form. The "Gallium" experiments had very low energy thresholds, about 200keV, and so were sensitive to the copious pp neutrinos. The Chlorine experiment, as its name implies, uses Chlorine ($^{37}$Cl) as a target and has a threshold of 800keV, making it sensitive primarily to $^8$B and $^7$Be neutrinos.

### Direct Counting Experiments

Direct counting experiments have the ability to measure the time, energy and sometimes angle of incidence of a neutrino interaction. Water Cerenkov experiments and other detectors that use scintillators are examples. The former will be discussed below. Water Cerenkov experiments that use light water as a target and detection medium rely on neutrino-electron scattering to detect neutrinos. The interaction is:

$$\nu + e^- \longrightarrow \nu + e^-. \tag{1.3}$$

When a neutrino scatters from an electron in the water, the electron can move through the water faster than light does. During this time the electron emits Cerenkov radiation in a characteristic cone shaped pattern and the light is detected by photomultiplier tubes (PMTs).

The Kamiokande [20] and Super-Kamiokande [7] experiments are the most important water Cerenkov detectors to date. The latter is a larger version of the former. The energy thresholds of these experiments are roughly 5-7 MeV and as a result they are only sensitive to the high energy $^8$B and hep neutrinos.

### Solar Neutrino Experimental Results

All five neutrino experiments mentioned above detect a deficit of solar neutrinos relative to predictions of the standard solar models. The experimental results are compared to theoretical predictions for the most recent model of Bahcall and Pinson-

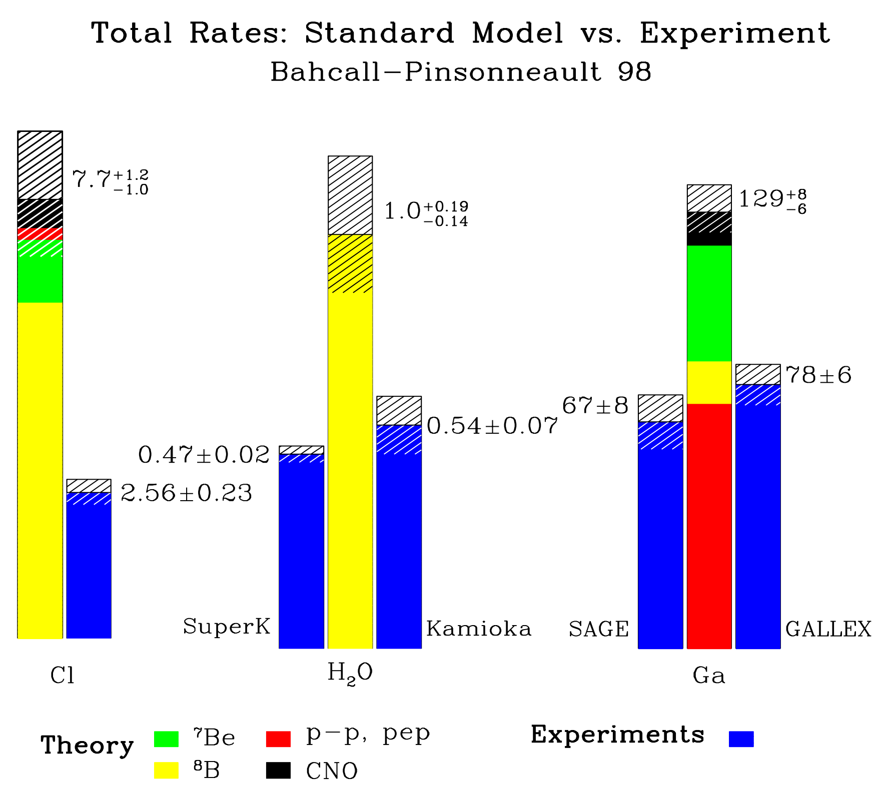


Figure 1.2: Bahcall-Pinsonneault SSM (1998) comparison of expected event rates with measured rates for five neutrino experiments. Theoretical and experimental uncertainties are shown and cannot explain the discrepancy [17]. (From John Bahcall's web page: http://www.sns.ias.edu/∼jnb/ )

neault in figure 1.2 [17]. It can be seen that all experiments detect fewer neutrinos than predicted and that the deficit is far larger than both the theoretical and experimental uncertainties. This is only part of the solar neutrino problem. After the results of these experiments became available, it was realized that there was another aspect to the problem. The deficit of solar neutrinos seems to be a function of energy.

Global fits to the rates of all five major experiments have been done with the $^8$B and $^7$Be fluxes left as free parameters but with the shapes and the other parameters of the solar model left intact [21]. The result is shown in figure 1.3 which uses the Bahcall-Pinsonneault SSM from 1995 with helium and metal diffusion effects included. The model itself is a point at the upper right hand corner of the plot and the ellipse encircling that point is the theoretical uncertainty of the model calculated from 1000 Monte Carlo solar models done by Bahcall and Haxton [22]. The 90% confidence level limits in the $^8$B - $^7$Be parameter space are labeled for each experiment. The Kamiokande and Super-Kamiodande experiments can only detect $^8$B neutrinos and are consistent with a band shown which is independent of the $^7$Be flux. The other two ($Cl$ and $Ga$) experiments have different relative sensitivities to $^7$Be amd $^8$B neutrinos and so have upper limits with different slopes on the plot.

It is seen that the $^8$B and $^7$Be fluxes deduced from experiments are inconsistent with the SSM values at the 90% confidence level. Furthermore, the only overlap of the allowed regions is at $\phi(^8B)/\phi(^8B)_{SSM} \sim 0.34$ and $\phi(^7Be)/\phi(^7Be)_{SSM} \sim 0.0$. That

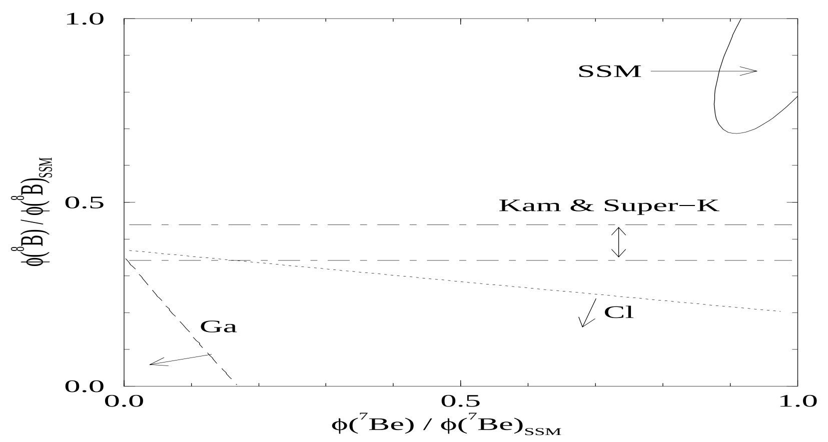


Figure 1.3: Results of a model independent analysis where global fits of the event rates of four major neutrino experiments were fit to the predictions from the Bahcall-Pinsonneault SSM (1995) with the fluxes left as free parameters. Shown are the 90% confidence level inclusion regions of the $^8$B vs $^7$Be fitted flux plotted for each experiment. It is seen that there is a very small region of agreement at 0.34 on the y-axis and 0 on the x-axis [21]. (The author thanks N. Hata for the use of this figure.)

is: a much lower $^8$B flux and *no* $^7$Be flux.

A complication arises due to the fact that the nuclear species involved in the creation of $^8$B neutrinos are produced only by the $^7$Be reaction. If $^8$B neutrinos were suppressed relative to $^7$Be neutrinos it could be explained by, for instance, a overestimation of the cross section leading to the $^8$B neutrinos. The case at hand, however, cannot be explained by such an argument. This fact is the crux of the argument for neutrino oscillations which will be discussed in the next section.

## 1.2 Possible Explanations of the Solar Neutrino Deficit

Logically, there are a number of possible explanations for the solar neutrino deficit and the incompatibility of the flux measurements with the predicted $^8$B and $^7$Be fluxes. First, the theory could be wrong. Second, one or more of the experiments could be wrong. Third, the physics of neutrinos may not be properly understood (independent of the theoretical SSM), *i.e.* there might be some new neutrino physics to be discovered.

### 1.2.1 Are The Solar Models Or Experiments Wrong?

The SSMs are not thought to be incorrect at the level required to explain the solar neutrino problem. The theoretical uncertainties have been thoroughly examined. There is excellent agreement between the predictions of the SSMs and helioseismoligical measurements of the solar sound speed [23]. Furthermore, the pp neutrino flux provides a constraint on the solar luminosity as the number of pp reactions is directly linked to how much light is produced. The Gallex and SAGE experiments have measured the flux of all solar neutrinos combined and the results are consistent with the SSM pp flux and a small contribution from all other sources.

To address the approximations made in SSMs or to add other features, many nonstandard solar models (NSSMs) have been put forth. Most of these models can be parameterized by the value they predict for the core temperature of the sun and most of them predict a cooler sun relative to the SSM. The neutrino fluxes are very sensitive to changes in the core temperature, but $^8$B neutrinos are more sensitive ($\phi_{^8B} \sim T^{18}$) than $^7$Be neutrinos ($\phi_{^7Be} \sim T^8$) [13]. Cooler temperatures therefore decrease the ratio of $^8$B to $^7$Be fluxes, the opposite effect to what is seen experimentally. Thus, NSSMs do not fit the data well and it is not possible to find a parametrization that can explain the data without adding exotic effects [13, 24, 25].

The fact that all solar neutrino experiments see a deficit of neutrinos lends credence to the argument that the experiments are correct. More important is the fact that the Gallium experiments are not only consistent with each other but, in addition, both have performed calibrations of their detectors with neutrino sources with known fluxes. The results of both calibrations were that the expected and measured neutrino flux (or equivalently neutrino interaction cross section) agreed to a very high accuracy. The results are:

$$R = \frac{\sigma_{measured}}{\sigma_{calculated}}, \tag{1.4}$$

$$R_{GALLEX}[26] = 0.93 \pm 0.07, \tag{1.5}$$

for Gallex and:

$$R_{SAGE}[27] = 0.97 \pm 0.12, \tag{1.6}$$

for SAGE. These experiments verified that there is no significant systematic bias towards low rates in these experiments and the energy regime probed showed that no bias exists with respect to $^{7}$Be neutrinos.

In summary, neither the solar models, nor the solar neutrino experiments appear to be incorrect at the level required to explain the solar neutrino problem. The final possibility is that new solar neutrino physics awaits discovery. The only current model which can correctly account for the experimental data is that of neutrino oscillations. Neutrino oscillations will be discussed below.

### 1.2.2 Neutrino Oscillations

If the solar models and the experiments are both correct, the only other possibility is that something is happening to the neutrinos between their point of emission in the sun and the earth. This leads to the hypothesis that neutrino oscillations are responsible for the observed neutrino deficit. In this model, electron neutrinos, the only type of neutrino emitted by the sun, "oscillate", or turn into either a mu, a tau or a sterile neutrino ($\nu_\mu$ , $\nu_\tau$ and $\nu_s$ respectively), with some probability during the trip from the sun to the earth. $\nu_\mu$ and $\nu_\tau$ interact with matter but $\nu_s$ does not.

The radiochemical experiments are only sensitive to $\nu_e$ . The deficit of neutrinos may be accounted for by $\nu_\mu$ and $\nu_\tau$ resulting from neutrino oscillations. The light water Cerenkov detectors can detect all active neutrino flavors, but cannot distinguish $\nu_e$ from $\nu_\mu$ and $\nu_\tau$ and are approximately seven times more sensitive to $\nu_e$ than to

$\nu_\mu$ and $\nu_\tau$ . If neutrino oscillation are occuring, the smaller cross section for $\nu_\mu$ and $\nu_\tau$ neutrinos would lead to an apparent deficit of $^8$B neutrinos. Furthermore, the presence of matter can increase the oscillation probability in an energy dependent way. This could explain the discrepency between experiment and theory of the ratio of $^8$B to $^7$Be neutrino fluxes described earlier [28, 29].

The concept of neutrino oscillations leads to further important implications. Neutrino oscillations can only occur if neutrinos have mass. In the Standard Model of particle physics, neutrinos are treated as massless. The recent discovery of neutrino oscillations, and therefore neutrino mass, by the Superkamiokande experiment [30] is the first piece of physics that contradicts the Standard Model. However, the Standard Model can be modified to encompass neutrino mass.

A full discussion of the phenomenon of neutrino oscillations is beyond the scope of this thesis. Below is a description of the basic points. Later, experimental evidence of neutrino oscillations will be discussed.

### Vacuum Oscillations

Vacuum oscillations are the simplest form of the broader category of neutrino oscillations. The idea is that the neutrino's flavor eigenstates are not equivalent to their mass eigenstates. Weak interactions take place in the flavor basis while neutrinos propogate as mass eigenstates. A neutrino's "flavor" is labeled by the particle it interacts with in a charged current interaction. $\nu_e$ interacts with an electron, $\nu_\mu$ with a muon, and $\nu_\tau$ with a tau. A simple time dependent quantum mechanical analysis shows that under certain conditions, neutrinos of one flavor can "oscillate" or turn into another flavor. The relationship between the mass and flavor eigenstates can be expressed by the unitary transformation equation:

$$\begin{pmatrix} \nu_e \\ \nu_\mu \end{pmatrix} = \begin{pmatrix} \cos\theta & \sin\theta \\ -\sin\theta & \cos\theta \end{pmatrix} \begin{pmatrix} \nu_1 \\ \nu_2 \end{pmatrix}, \qquad (1.7)$$

where $\theta$ is called the *vacuum mixing angle* between the flavor and mass eigenstates, $\nu_1$ and $\nu_2$ are the mass eigenstates corresponding to $\nu_e$ and $\nu_\mu$ respectively, and only 2 flavor oscillations are being considered. This treatment may oversimplify reality but it shows the physics in a concise manner. For discussions of the full three flavor problem see the references [31, 32, 33].

From this equation one can obtain the time evolution of the $\nu_e$ and $\nu_\mu$ states, and the survival probability of the electron neutrinos as a function of energy and distance from the sun. The result for the survival probability is [13]:

$$\mid \langle \nu_e(t) \mid \nu_e(0) \rangle \mid^2 = 1 - \sin^2(2\theta)\sin^2(\frac{(\Delta m^2)t}{4E}) = 1 - \sin^2(2\theta)\sin^2(\frac{\pi D}{L_V}), \qquad (1.8)$$

where E is the average energy (E $= 0.5$(E$_1$ + E$_2$)), $\Delta m^2 = m_2^2 - m_1^2$ is the difference in the squares of the masses of the mass eigenstates, D is the distance travelled in time t and $L_V$ is known as the vacuum oscillation length. The vacuum oscillation length can be expressed as:

$$L_V = \frac{4\pi E\hbar}{\Delta m^2 c^3}. \tag{1.9}$$

It can be seen that there are two parameters, $\sin^2(2\theta)$and $\Delta m^2$, both of which can affect the $\nu_e$ survival probability. Radiochemical and Water Cerenkov experiments measure the survival probability averaged over the energy spectra of the neutrino fluxes. The region of parameter space that is of interest is the region such that $\sin^2(2\theta)\sim 1$ and $L_v \sim 1$AU. In this case, one obtains almost full suppression at some energies. When averaging is done and fits to the experiments are calculated, this region of parameter space does fit the data. A plot of the allowed region for vacuum oscillations calculated by doing simultaneous fits to all of the experimental data is shown in figure 1.4 [21].

### Matter Oscillations

The basic idea of matter oscillations is that contributions to the effective mass of neutrinos due to neutrino scattering in matter is flavor dependent. Neutral current (NC) interactions contribute the same amount for all three neutrino types. However, at solar neutrino energies, charged current (CC) interactions only proceed for electron neutrinos in ordinary matter. The CC interaction introduces an extra mass matrix term which changes the probability amplitude of neutrino mixing. The additional term was originally calculated by Wolfenstein [34, 35]:

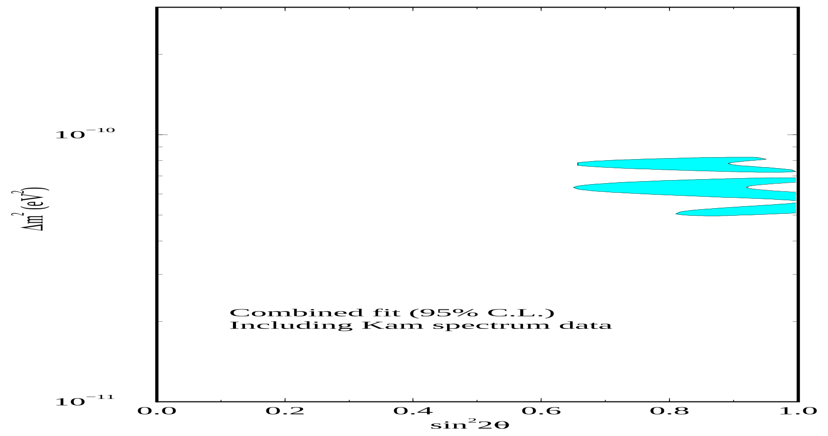


Figure 1.4: Combined fit of data from all experiments to the vacuum oscillation hypothesis where the 95% contours are shown [21]. (The author thanks N. Hata for the use of this figure.)

$$\Delta M_{matter} = \sqrt{2} G_F n_e \mid \nu_e \rangle \langle \nu_e \mid, \tag{1.10}$$

where $G_F$ is the Fermi weak interaction coupling constant and $n_e$ is the local electron number density in the matter through which the neutrino is traversing. For $\overline{\nu}_e$ , the term has the opposite sign but the same amplitude [36, 13].

The subject of matter oscillations is rich and the discussion too complex for the purposes of this thesis. It is enough to say here, that large suppressions are possible given the electron densities, $n_e$, in the sun and the earth. Resonance conditions occur which provide maximal mixing for neutrinos of certain energies. Very good descriptions of the methods and approximations used exist in the literature [34, 35, 37, 13, 38, 39]. The pioneering theoretical work in this area was completed by Wolfenstein

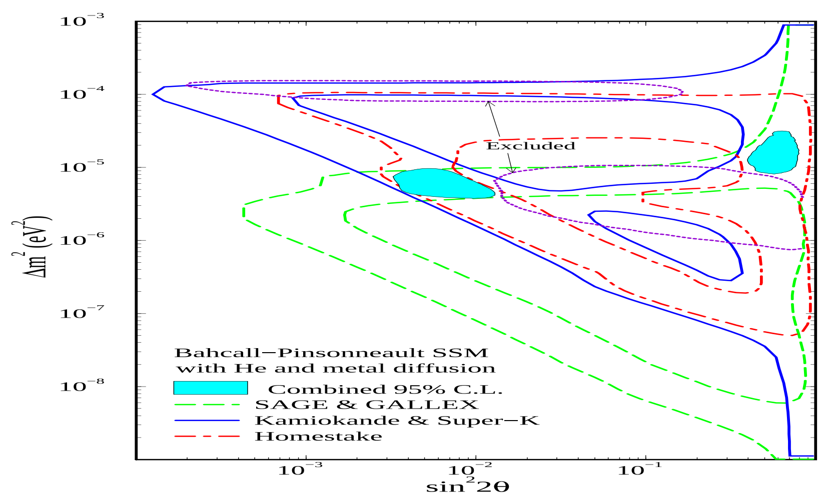


Figure 1.5: Combined fit of data from all experiments to the MSW oscillation hypothesis over the range of parameter space relevant to solar neutrino energies. The inclusion regions for each experiment as well as the combined result 95% confidence level contours are shown [21]. (The author thanks N. Hata for the use of this figure.)

[34, 35] and by Mikheyev and Smirnov [40]. The matter oscillation effect has come to be known as the "MSW effect" after these scientists. The MSW effect can explain the experimental data well as will be seen below.

Detailed analyses have been completed by many researchers on the MSW effect as pertains to solar neutrino oscillations [21, 17, 41, 42]. Numerical calculations are done using the neutrino production and electron density profiles of the sun (assuming some solar model). The survival probabilities of the electron neutrinos as they traverse the sun and earth are calculated. From this information the $\nu_e$ and $\nu_\mu$ fluxes can be computed and followed (including the effects of vacuum oscillations) to the earth. It is possible to use the results of all the solar neutrino experiments to fit for the

MSW parameters, $\Delta m^2$ and $\sin^2 2\theta$, by calculating the expected experiment rates as a function of the parameters. The result of such an analysis is shown in figure 1.5, from Hata *et al.* [21]. The figure shows the 95% confidence level contours allowed by each experiment separately. Also shown is the 95% confidence level contour for a fit to all experiments combined. Two "MSW solutions" are shown in the shaded regions. The solution at $\Delta m^2 \sim 6 \times 10^{-6} eV^2$ and $\sin^2 2\theta \sim 10^{-2}$ is known as the "small angle" solution. The second solution, near $\Delta m^2 \sim 10^{-5} eV^2$ and $\sin^2 2\theta \sim 0.6$ is generally referred to as the "large angle" (LA) solution. The vacuum oscillation solution, shown in figure 1.4 doesn't change as matter does not contribute to neutrino oscillations in that region of parameter space.

### Experimental evidence of neutrino oscillations

As stated above, recent results from the Super-Kamiokande experiment claim evidence for neutrino oscillations using a sample of neutrinos created in the atmosphere of the earth. Many systematic checks have been done and the result is robust. The energy and angle dependence give consistent results. The $\nu_e$ do not show a deficit but there is a deficit of $\nu_\mu$ neutrinos. The $\nu_\mu$ are presumably oscillating into $\nu_\tau$ although oscillations to $\nu_s$ are not ruled out.

## 1.3 The role of SNO

The Sudbury Neutrino Observatory (SNO) is a next generation solar neutrino detector. The novel design uses heavy water as the main neutrino target. The charged current (CC) and neutral current (NC) interactions of neutrinos with the deuteron, not only have relatively large cross sections, but also can be utilized to measure the ratio of electron neutrinos to all active neutrino species thus overcoming the limitations of previous experiments. At solar neutrino energies, the CC interaction occurs only for $\nu_e$ while the NC interaction occurs with the same probability for $\nu_e$ , $\nu_\mu$ and $\nu_\tau$ . SNO can separate CC and NC events on a statistical basis, measuring the $\nu_e$ neutrino flux through the CC interaction and the total neutrino flux through the NC interaction. The ratio, CC/NC, may prove or may disprove that some of the solar $\nu_e$ have changed flavor to $\nu_\mu$ , $\nu_\tau$ or both. A more detailed discussion of neutrino interactions in heavy water, along with the discussions of the SNO experiment is given in Appendix A. A full description of the SNO detector and its subsystems will be presented in Chapter 2. For now, it will suffice to say that SNO is designed to test the hypothesis of neutrino oscillations and therefore neutrino mass for interacting neutrinos.

### 1.4 SL and SNO

As stated above, construction delays have changed the subject of this thesis from solar neutrinos to sonoluminescence. SL was used as a calibration of the time response of the SNO detector. Also, the SNO detector is a useful laboratory for the phenomenological study of SL itself. Experiments were carried out as part of this thesis, to attempt to determine the spot size (size of the light emitting region of a SL bubble) of SL and the precise angular distribution of photons. SL experiments performed in the SNO detector were able to utilize many of its unique features including the fast electronics, the large number ($\sim$10,000) of photo-multiplier tube detectors and its stable spherical geometry. Sonoluminescence, the sources developed for the experimentation, and the results will be presented in the sections and chapters that follow.

### 1.5 Sonoluminescence

Sonoluminescence is a phenomenon that was discovered in 1934 but was not amenable for study until the early part of this decade when techniques were developed to make it stable and reproducible. This section will discuss the discovery, history and what is known and unknown about sonoluminescence.

### 1.5.1 Discovery and History of SL

In 1927 Richards and Loomis [43] found that hydrogen peroxide ($H_2O_2$) was formed in water driven by high intensity ultrasound. This was the first hint of a phenomenon known as Sonoluminescence. Later, Schmitt *et al.* [44] noticed that the production of $H_2O_2$ was correlated with the appearance of transient cavitation bubbles. Mecke [45] noted that the quantum of energy needed to make peroxide from water was of the right order of magnitude to fall in the visible part of the spectrum. Following Mecke's suggestion, Frenzel and Schultes [8] looked for visible light emanating from water driven by a sound field and indeed discovered SL in 1934.

Not much happened in the field for fifty years or so as the phenomenon was inherently unstable. There were some attempts at explaining SL in terms of sparking from static electricity and some researchers obtained SL in the absence of cavitation noise [46].

In 1990, Philip Gaitan and Lawrence Crum [9, 10], then at the National Center for Physical Acoustics at the University of Mississippi, developed a means to stablize a single bubble in a sound field and were able to coax the bubble into producing SL repetitively, predictably and stably. This significant advance, dubbed "single bubble sonoluminescence" (SBSL), led to an explosion of activity and a new field of study. Many researchers have published many experimental and theoretical papers on the subject.

Since 1992 most of the important experiments on SL have been done by Barber, Hiller, Lofstedt, Putterman and Wenninger at UCLA. They have measured (among other things) the energy spectrum [47, 48], the bubble radius as a function of time [49], and the dependence of the light intensity on temperature, pressure, and noble gas concentration [50]. They have also done preliminary angular distribution measurements in which a small dipole component was observed under certain conditions [1]. Another important measurement was made by Gompf *et al.* [51] who measured the SL pulse width ($30ps < PW < 300ps$ over a wide range of parameter space); this measurement has been confirmed by two other groups [52, 53].

### 1.5.2 Characterization of SL

For the remainder of this thesis, unless otherwise specified, the term "sonoluminescence" will be used to mean the stable "single bubble sonoluminescence" (SBSL) discovered by Gaitan and Crum. Without SBSL this thesis would not have been possible. It is extremely stable and reproducible, and can be obtained on demand unlike its chaotic cousin, cavitation SL. Below is a discussion of SBSL (or SL). It is not possible to cover all of the nuances of the phenomenon here. Excellent review articles and other material have been written elsewhere [50, 54].

SL is a phenomenon in which sound energy is converted to light energy. This is acheived by introducing a gas filled bubble (usually air) into the pressure antinode of a flask (usually spherical) filled with a fluid (e.g. water) which is being excited in one of its acoustic resonant modes. In a spherical flask, one of the 0th order spherical Bessel function modes of the flask is used, which has a pressure antinode at the center of the flask - the monopole mode. A bubble at this site will oscillate in the radial direction at the frequency of the driving sound field. If the drive parameters (amplitude, frequency and gas partial pressure in the fluid are the most important) are correctly tuned, visible blue light will be emitted. This happens when the bubble is at the point of minimum radius.

### What Is Known

What is known about SL? The light is characterized by: a blue appearance which can be seen with the naked eye in a darkened room; the spectrum peaks in the UV and can be fit to a black body spectrum with a very high temperature ($\sim 50,000$ K with a water temperature of $10^\circ\ C)[47,\ 48] orabrehmsstrahlung-likespectrum[55]; thepulsewidthhasbeenmeasuredtobebetween 30 and 300 ps[51,\ 52,\ 53]; thepulse-$
$to-pulsesynchronismofthelightpulseisextremelysharp,$ ¡ 50ps$[56,\ 50]; andtheangulardistributionofphotonsisisotropicinsomecaseswhileinothersasmalldipolemomentisobserved[1]. Thedipolemomenthasbeenattributedtoadipolemomentinthebubblewall[1]. Measurementsofthebubbleradiusoverthesoundfieldperiodshowthemaximumandminimumradiiare 40$
$\mu$m and 0.5$\mu$m respectively [49, 50].

The number of photons emitted per flash has been measured by the author to be between $10^4$ and $10^7$ photons/flash into $4\pi$ steradians in the optical portion of the spectrum ($200nm < \lambda < 700nm$) to which PMTs, used to perform the measurement, are sensitive. The power of the emitted light is between 1 and a few hundred mWatts, while roughly 100 Watts of power is required to drive the sound field in the appropriate regime of parameter space. This result agrees with previous measurements [50].

The intensity of the light has been an interesting area of study. The intensity increases with increasing drive pressure from the sound field. However, there are lower and upper thresholds forming a window of drive pressure inside of which SL can be obtained and outside of which it cannot. This is typically a very narrow window of the order of a few tens of millivolts for a few hundred millivolt drive voltage (the oscillator driving the sound field). Even more sensitive is the dependence on frequency. The resonant frequency must be adjusted to within 1 part in $10^4$ (or even $10^5$) or the light intensity will go to zero. There is evidence that the intensity increases with decreasing drive frequency (on a larger scale than mentioned above) although this has to be acheived with different sized sources and the calibration is difficult. More interestingly, reducing the water temperature from 40 $^{\circ}C$ to 10 $^{\circ}C$ *increases* the intensity by a factor of 100 [56].

The intensity of SL light is stable from pulse to pulse if the water is degassed properly and one is operating in a stable regime of parameter space. More will be mentioned about these two points in section 3.3 which shows some of the raw data from SL in the SNO detector.

The spectrum of SL has been measured [47, 48] and it is found that the spectrum rises with photon energy. The peak of the spectrum is unmeasured as it is in the regime where water absorbs most of the photons ($\lambda < 200nm$ in the UV). The spectrum can be fit to the tail of a black body spectrum with a very high "temperature" (T=25K at 20 $^{\circ}C$ water temperature and T=50K at 10 $^{\circ}C$ water temperature) although it is still unclear whether or not this is the true temperature inside the bubble at light emission. No lines have been observed in the spectrum and lines don't exist to within 10nm FWHM resolution [47].

The most interesting thing about SL is the degree of energy focusing. This can be calculated simply by estimating the energy per atom in the sound field and in emitted light. The former can be estimated as [56, 50]:

$$\langle \rho v^2 \rangle \cdot (volume/atom) \sim 4 \times 10^{-12} eV/atom, \tag{1.11}$$

where $\rho$ is the density of the water and $v$ is the velocity of the molecules due to the sound field. This number can be compared to a photon energy of $\sim 5eV/atom$. The energy is focused by 12 orders of magnitude.

The intensity, stability and spectrum of SL is highly correlated with the type of fluid and the type of gas used to make the bubble. Many different fluids and gasses have been tried and to date the best seems to be water with Oxygen with 1% Xenon added at a partial pressure of 150 Torr [50]. Both more and less Xenon gives poorer results. Interestingly, this is roughly the percentage of Argon in air which is why the first SBSL experiment worked so well.

Noble gasses seem to be the most important component, Xenon and Argon being the best. SL without them works either poorly or not at all depending on the gas used. Another interesting twist is that when heavy water ($D_2O$) is used as the fluid, there is a large red shift in the spectrum compared to when water ($H_2O$) is used [47, 48].

#### What Is Unknown

There are two fundamental measurements regarding light production that remain to be done or improved from those mentioned above. Those are:

(1) a measurement of the size of the photon emission region, and

(2) a more accurate measurement of the angular distribution of SL photons.

Experiments were performed as part of this thesis with the intent of doing these two measurements. The results will be discussed in Chapter 4. Below, some SL theory will be discussed.

### 1.6 SL Theory

There are two general categories of theories that attempt an explanation of the emission mechanism of SL light:

(1) those which rely on classical physics and

(2) those which rely on quantum electrodynamics (QED).

Various theories from both of these categories are discussed briefly below. Experiments carried out as part of this thesis were designed to address some of the predictions of some of these theories.

### 1.6.1 Classical physics SL theories

Within this category, two separate theories will be discussed. They will be referred to as:

(1) the "adiabatic heating" model,

(2) the "shock wave" model.

Brief discussions of each of these occur below including the merits of each and a comparison of the three at the end. Further information can be obtained from references cited therein.

#### Adiabatic Heating Model

The simplest theory attempts to model the light emission mechanism with a classical model of adiabatic heating of the bubble gas. In this theory, the contraction of the bubble in the compression phase of the acoustic cycle causes the gas in the bubble to heat adiabatically. It is necessary to use the Van der Waals equation of state as that limit is reached when the bubble nears its minimum radius [50, 49].

The bubble ambient, maximum and minimum radii have been measured. They can be used to calibrate the above model. The fits are very good and can explain all features of the bubble's radius vs. time curve [49]. With these and other inputs one can calculate the expected temperature of the bubble gas at minimum radius. Temperatures of 5000K to 10,000K are acheivable, but no higher [50]. This corresponds to maximum photon energies of about 1eV and many photons of average energy 5eV are radiated from the bubble while it is sonoluminescing. Thus the adiabatic heating model does not appear to explain the experimental results. The approximations of low Mach number used in the adiabatic model have been shown to be invalid during the end of the compression phase - the bubble wall is travelling at Mach 4 (relative to the speed of sound in the bubble at ambient pressure) at that time. Including this effect into the model is non-trivial but will be described in the next section. Such models are no longer adiabatic.

Other experimental evidence that disfavors the Adiabatic Heating model is the aforementioned measurements of the SL pulse width (PW) which is essentially the same for blue and red light. If adiabatic heating were the only heating mechanism, the red light should turn on earlier and turn off later than the blue light; as the bubble heats up during contraction the spectrum should move from the red towards the blue and vice versa as the bubble starts to expand from its minimum radius.

### Shock Wave Model

The Shock Wave model [57, 50] is an extension of the adiabatic heating model in which the non-linear portion of the bubble collapse, when the Mach number becomes important, are considered. It provides extra energy focusing via an assumed shock wave (due to the supersonic collapse) being launched towards the bubble interior. Such a model is meant to explain the short (and uniform as a function of $\lambda$) PW and UV energy spectrum observed in experiments. The following discussion is largely taken from Barber *et al.* [50].

This model's predictions agree well with experiment, however, the shock wave has yet to be detected experimentally. Both the pulse width and bubble temperature are consistent with experimental measurements: $30ps < PW < 300ps$ and $\sim 10^4 - 10^5 K$) respectively. Assuming this model is correct, the light from the bubble comes from a much smaller volume, dictated by the shock radius, than the actual bubble volume at the time of light emission. This prediction of the Shock Wave model was addressed in experiments carried out as part of this thesis and will be discussed further in Chapter 4.

Deficiencies of the Shock Wave model are that it requires too many input parameters, for example, the acoustic drive level and ambient radius ($P_a$ and $R_0$). It is also not known how to predict the minimum shock radius [57, 50]. Futhermore, the model does not explain some of the mysteries of SL such as why pure diatomic gases give bad SL while noble gases yield good SL. Further modeling can be done which includes effects of the Van der Waals equation of state, and equations of state that are corrected for plasma effects such as the degree of ionization.

### 1.6.2 QED SL theories

The other major group of SL theories is the group which attributes SL radiation to quantum vacuum radiation. All of these theories postulate that the photons are formed due to changes in the vacuum state during the collapse of the bubble. The index of refraction at some radius smaller than the bubble at time, t, is a function of time as the bubble shrinks and water replaces the more rarified gas at that radius. This sudden jump in the index of refraction causes zero point fluctuations that result in pairs of real photons being emitted.

Julian Schwinger, is the initiator of this general "Casimir route" to explaining SL. He called the model a "dynamical Casimir effect" and in a series of papers [58, 59, 60] he was able to calculate that the dominant contribution to the Casimir energy of a bubble is proportional to the phase space volume, $\sim Vk^3 = 4\pi/3R^3k^3$ which automatically makes it power law agreeing with experimental measurements. To arrive at this result, Schwinger used a quasi-static model in which he calculated and compared the Casimir energies for a bubble in the rarified state (large bubble) and separately for the contracted state (small bubble).

This type of model (including the ones mentioned below) explain three main aspects of SL, the pulse width, the "temperature" inside the bubble at the point of emission, and the UV cutoff of the spectrum.

As for the "temperature" of the black body fit to the energy spectrum of SL, it has already been pointed out that this may not be the true temperature inside the bubble. The spectrum of SL predicted from this model cuts off at the wavenumber, K, in the UV which naturally avoids the necessity of explaining the lack of any evidence for higher energy photons. The true temperature of the bubble can be much less than the result from the fit to a black body spectrum. The spectrum tail looks hotter than it is because of the "squeezed" or correlated nature of the two photon states [61].

Liberati *et al.*, and references therein, describe some criticisms of Schwinger's model in detail [61]. This situation has been criticized and clarified by others as well [62, 63]. One group [64] discarded the volume term shown above and eventually the surface term as well leading to a Casimir energy which is far too small to explain SL. Liberati *et al.* and others [62, 63] point out that the discarded terms were ignored for reasons related to renormalization. They discarded any terms which had a cutoff dependence. However, at least in the volume term case, the cutoff dependence comes from the asymptotic behavior of the index of refraction - a real physics effect which can't be ignored. Another group [65] failed to retain the volume term but this time it was due to ignoring the continuous part of spectrum. Finally, Liberati *et al.* mention a comment made by Barber *et al.* [50] that the effect should be strongest in the portion of the cycle where the rate of change of the volume is largest (near the maximum radius) while the light output occurs near the minimum radius where the surface area is changing at the maximum rate. This incompatability is explained by Liberati *et al.* and will be discussed with their model below.

### Eberlein's "Unruh Radiation" Model

Eberlein [66, 67] has invented a model based on Unruh radiation which is truly a dynamical Casimir effect model. In this model the photons are produced via an adiabatic change in the refractive index in the area between the minimum and maximum bubble radii. The boundary between the air and water moves as a function of time. This boundary accelerates with respect to the rest frame of the quantum vacuum state [61].

This Unruh radiation model is a combination of an adiabatic approximation of the change of index of refraction with time and perturbation theory. The theory predicts most of the light is emitted near the minimum bubble radius where the acceleration and velocity of the bubble are changing the most rapidly. This is in agreement with experiment and is the exact opposite to the prediction of Schwinger's model.

The problem with Eberlein's model is that it doesn't produce enough photons to explain SL [66, 67, 61]. It is a much weaker effect than that of Schwinger mentioned above. The reason for this is Eberlein's use of the adiabatic approximation which leads to exponentially suppressed photon production [61]. The suppression is a factor of $EXP(-\omega\tau)$, where $\omega$ is the frequency of the light and $\tau$ is the rate at which the index of refraction changes. In Eberlein's model, the change in index of refraction happens on the time scale of the acoustic period as it is the moving bubble wall which changes it. This time scale is far larger than that of the light so the supression is large.

**Liberati** *et al.* **Modifications**

Liberati *et al.* have expanded on Schwinger's work and the results they acheive are consistent with Schwinger's original model [61]. In their series of papers, they discuss the previous two models (as well as others) and clear up some confusion that has appeared in the literature related to the relative merits of the models. Some of this has already been discussed above.

The novel contribution of Liberati *et al.* is to calculate the Bogolubov coefficents which relate the vacuum states of a rarified bubble to that of a contracted bubble. They then claim that in the sudden approximation, that is, the index of refraction changes suddenly at a given radius from the center of the bubble, Schwinger's result is correct and an intensity proportional to phase space volume, which automatically makes the spectrum power law, is obtained. They use the same cutoff due to the asymptotic behavior of the index of refraction in the UV that Schwinger used.

The model is not dynamical except for the use of the sudden approximation. The authors are quick to point this out and to say that further work should attempt to find a dynamical model along the same lines. They also suggest that better modeling of the index of refraction as a function of frequency might address the differences in light intensity as a function of the noble gas concentration among other things.

The results of this group of papers is not so very different from those of Schwinger although the Casimir energy is calculated analytically and confusion about the volume term renormalization is illuminated. The model, like Schwinger's, would predict that the maximum light output near the maximum bubble radius where the volume is changing the most rapidly - however, Liberati *et al.* have added a new feature which overcomes this problem.

The authors postulate that there is a regime during the bubble motion that the index of refraction can change extremely rapidly, on a femtosecond time scale, which is enough to make the effect valid for SL. This would happen near the minimum bubble radius as it is postulated that the index of refraction of the *gas* inside the bubble suddenly changes, perhaps by sudden ionization, rather than that of the bubble surface. This would argue for some hybrid theory incorporating the shock wave model with their as yet undeveloped dynamical Casimir model.

### 1.6.3 Comparison of the QED or Casimir models

To briefly review the QED models: Schwinger's model has the correct energy spectrum and intensity of light but it isn't dynamic and predicts the light emission at the wrong part of the acoustic cycle. Eberlein's model is dynamic and predicts emission at the correct part of the cycle but doesn't yield enough intensity to explain SL. The work of Liberati *et al.* attempts to resurrect a Schwinger-like model but reinterpret it in light of a regime where the bubble gas index of refraction suddenly changes, which removes the problem with Schwinger's model. Their model is not complete but suggestions are made as to how to improve it to incorporate predictions of the SL pulse width and sensitivity to noble gas concentration.

None of the models are perfect or even complete. However, they all predict that photons will be emitted in pairs which will be correlated and emitted back to back [66, 67, 61] (ideally, although finite volume effects tend to spread this out in some unspecified way). The models of Schwinger and Eberlein predict that the photons will be emitted from the bubble surface - just the opposite of the classical models which predict emission from the volume inside the bubble. The model of Liberati *et al.* predicts emission from inside the bubble as well although from an undefined portion which has a rapidly changing index of refraction.

The prediction that photons are emitted back-to-back can be tested to a high degree of accuracy by using the SNO detector. Such an experiment has been carried out as part of this thesis and the results will be presented in Chapter 4.

### 1.7 Outline of this thesis

This thesis is divided into five chapters. The solar neutrino problem and the first generation solar neutrino experiments have been described. It was stated that the radiochemical experiments are not able to detect $\nu_e$ and the water Cerenkov experiments are not able to separate $\nu_e$ from $\nu_\mu$ and $\nu_\tau$ . This led to the motivation for the SNO experiment which is designed to measure both the solar $\nu_e$ flux and the flux of all active solar neutrino species independently and concurrently. A more detailed discussion of the physics of the Sudbury Neutrino Observatory is presented in Appendix A.

It has been stated that due to construction delays this thesis does not present analysis of solar neutrino data. Instead, the SNO detector response to a sonoluminescent source has been studied. The SL source has been used for SNO by performing some detector calibrations and studying detector systematic effects in detail. The SL source has been shown to outperform the standard optical calibration source by approximately 30% in performing PMT timing calibrations. Some detector pathologies have been detected which might have gone unnoticed if SL experiments were not carried out and analyzed. The SNO detector, with its spherical geometry and large number of photodetectors, has been utilized in return to study some fundamental aspects of sonoluminescence. SNO provided a unique opportunity to perform these experiments.

Because the SNO detector has been studied with the SL source and has been used for SL experiments, a detailed description of the detector is provided in Chapter 2. The work carried out for this thesis is presented in chapters 3 and 4. Chapter 3 describes the sources which were designed and built for the experiments undertaken for this thesis, and describes some experiemental and theoretical issues involved in the experiments and data analyses presented in the following chapter, Chapter 4. Chapter 4 the data and analyses carried out for this thesis. Chapter 5, summarizes the results of this thesis and describes areas of possible further study.

# Chapter 2

# The SNO Detector

In the previous chapter, the solar neutrino problem and the experiments that brought it to light were discussed. The SNO detector is described in detail in this chapter. Due to construction delays, this thesis uses the SNO detector to study the detector response to a sonoluminescent source rather than neutrinos. SL has been described in Chapter 1 and experimental issues relating SL and the SNO detector are presented in Chapter 3.

Sections 2.1-2.9, describes the SNO detector and subsystems. There is a summary in Section 2.10. If further detail is desired, a publication which describes the detector is available [68].

## 2.1 A Brief Description of the SNO Detector

A schematic diagram of the SNO detector is shown in Figure 2.1. The SNO detector is situated at the 6800 foot level of Inco Ltd.'s Creighton Mine near Sudbury, Ontario, Canada. The rock above the detector is mostly Norite. The depth and rock density

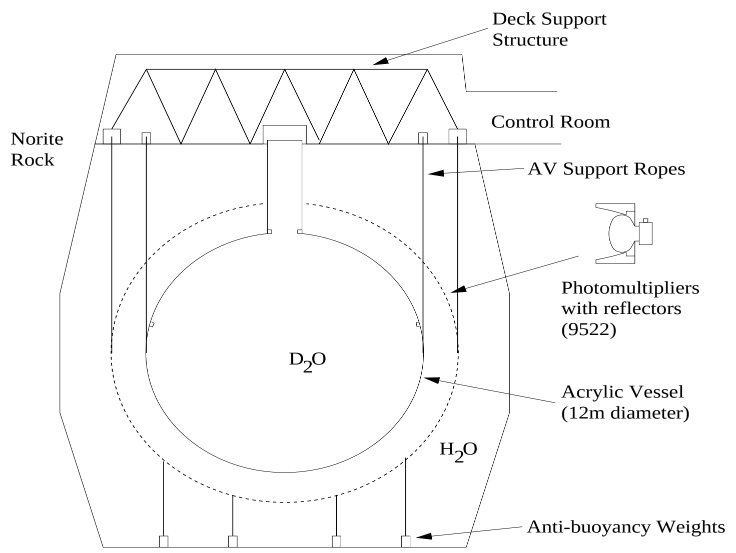


Figure 2.1: Schematic diagram of the SNO detector [69]. (The author thanks R. Ford for the use of this diagram.)

correspond to approximately 6000 meters of water equivalent (mwe). The detector is located in a barrel shaped cavity which is 22 m wide at the widest point. The walls of the cavity are lined with eight layers of Urylon coating to provide ground control of the rock wall, to provide a water proof seal and also to act as a barrier for radon emanating from the rock. A photomultiplier support structure (PSUP), with a geodesic geometry and radius of approximately 8.4 meters, supports 9522 inward looking and 91 outward looking photomultiplier tubes (PMTs) and is centered in the barrel shaped cavity. Concentric with the PSUP and inside it is a spherical acrylic vessel (AV) with a radius of 6 meters and a wall thickness of 5 cm which is designed to hold 1 kT of heavy water. Both the AV and the PSUP are supported by guide ropes which are anchored to a platform (hereafter referred to as "the deck") above the detector cavity. The rest of the cavity is filled with 7 kT of light water, 1.3 kT of which is between the AV and PSUP.

All of the materials making up the detector and subsystems, were carefully assayed and screened to minimize radioactive contamination. Furthermore, the lab is effectively sealed off from the mine at its entrance and clean room conditions averaging approximately class 2500 have been maintained for more than 4 years - even during much of the construction phase.

The light water surrounding the PSUP acts as a neutron and gamma shield. The size of the detector and cavity were designed specifically with this in mind. The PMTs at the equator of the detector are closest to the walls at approximately 2 meters. The distance is greater near the top and bottom of the detector.

### 2.2 Acrylic Vessel

The acrylic vessel (AV) is designed with the following criteria. The first is to isolate the $D_2O$ from the $H_2O$ and maintain the former's purity. The physics reason for the latter, is that hydrogen impurities have a large neutron capture cross section with no resulting high energy gamma and will therefore systematically reduce the NC detection efficiency. Another reason is that the $D_2O$ was loaned to SNO under the condition that it be maintained at a purity of at least 99.85%. The second design criterion is that the AV must maintain structural integrity over 10 years of operation while immersed in ultrapure $D_2O$ and $H_2O$ . Third, radioactive contamination in the AV materials were kept to a minimum and the total mass is minimized for that reason. Finally, the optical transparency of the AV was maximized. The amount of Cerenkov light originating from inside the AV that is attenuated or scattered is as small as possible given the other constraints.

As stated above, the AV has a radius of 6 meters and a nominal thickness of 5 cm. It is made from 72 panels of varying sizes and shapes which were bonded together. The AV has a long (8 meter) neck of 1.5 meter diameter which penetrates the deck above the cavity and is used to install calibration sources as well as to provide piping for $D_2O$ introduction.

The material used for the sphere is ultraviolet transmitting (UVT) cast acrylic chosen for its relative radioactive purity and the good match in spectral response to the PMTs. The neck is translucent UV absorbing (UVA) acrylic so that a minimum amount of the Cerenkov light originating in this region is "piped" to the main detector volume. The AV is supported by ten loops of Vectran HS fiber ropes which have low radioactivity and retain high strength in ultrapure water. Each rope is roughly 30 meters long and supports 5 tonnes (when the detector is filled with $H_2O$ and $D_2O$ ) which is 10% of its rated tensile strength. The ropes pass through ten special "rope groove" acrylic panels at the equator of the vessel.

### 2.3 PMT Support Structure

The PMT support structure (PSUP) is a geodesic framework to which panels holding the PMTs are anchored. As with the AV and all materials used in the detector, radioactive impurities in the PSUP had to be kept to a minimum. The structure is designed to be maintenance free for 10 years of operation while immersed in ultrapure $H_2O$ . Furthermore, the collection of Cerenkov light from the $D_2O$ by the PMTs had to be maximized. These design criteria led to a structure which is described below.

There are 751 panels made from ABS plastic that hold between 7 and 21 PMTs each. These panels and PMTs were assembled above ground in a clean environment, wrapped in protective containers and then shipped underground for installation. The panels were aligned to be centered on the $D_2O$ volume using a laser. Calibration source guide tubes penetrate the upper PSUP at six locations and the AV ropes penetrate at 20 locations. The PSUP is also designed to act as a light and water barrier between the inner detector and the outer part of the cavity.

### 2.4 Photomultiplier Tubes

All PMTs are 8 inch Hammamatsu type R1408 12 stage PMTs with special low radioactivity glass to reduce gamma radiation backgrounds from daughter products of the uranium and thorium chains. All materials used to fabricate the PMTs were assayed for radioactivity before they were deemed acceptable. There are 9522 inward looking and 91 outward looking PMTs. The inward looking tubes are mounted in the PSUP panels and have reflective light collectors around them. The entire array and reflectors cover 85% of the surface area and result in a light collection efficiency of 55%. Of the inward looking PMTs, 49 have dynode taps which connect to separate electronics channels. These are used to extend the dynamic range of the PMT charge by a factor of 100. If the standard electronics channels are saturated, these channels may give an estimate of the energy deposition in the detector. These are referred to as "low gain" PMT channels. The outward looking PMTs (OWLs) are situated near all of the nodes of the geodesic structure except the north pole as the neck of the AV protrudes through that point.

All components making up the 12 stage PMT bases were chosen for their low radioisotope content. The high voltage (HV) on the PMTs is in the range: $1700V - 2400V$. The HV value for each PMT is set such that the gain is $10^7$. The PMT noise rates are measured to be $< 1kHz$ in cooled water (∼10° C), lower than the room temperature value of ∼2KHZ. The transit time spread of an electron traveling from the photocathode to the first dynode is quoted by the manufacturer to be less than 1.6ns. Measurements yield a mean spread of 1.5 ns for all of the PMTs in the experiment.

A single waterproof RG59 75Ω coaxial cable connects the signal and high voltage (HV) of each PMT to the signal processing electronics discussed below in Section 2.6.

### 2.5 Heavy and Light Water Systems

Both the heavy and light water systems, which are completely independent, are capable of recirculating water continually. Assays to measure the degree of radioactive contamination from $Rn$, $U$, $Th$ and other elements are made regularly. The water is cooled and is kept at about 10° C in order to prevent bacteria from growing. A UV radiation unit in the recirculation system also reduces the bacteria count. Other systems include: degassification, regassification with nitrogen, purification and ultrafiltration. Additional assays are performed to measure pH, conductivity, bacteria count and suspended particles.

The light water comes from a surface purification plant which produces potable water for the entire mine. It can be obtained on demand at the detector site. The $D_2O$ was trucked in from the Bruce, Ontario, site of Ontario Hydro and transferred to a tank above ground. Isotopic purity checks are done before it is accepted and brought below ground in smaller tanks on rail cars. A pair of 60 tonne tanks underground store the $D_2O$ until it is ready to be put into the AV. About 5.7kT of light water exists outside the PSUP and 1.3kT between the PSUP and the AV. 1kT of heavy water fills the AV.

### 2.5.1 Filtering and Monitoring

The design goal of the background neutron rate in the heavy water is less than one tenth the NC rate predicted from solar models $\sim 5000y^{-1}$. This translates to a limit of $3 \times 10^{-15}g/g$ of Th and $4.5 \times 10^{-14}g/g$ of U in the $D_2O$ . SNO's assay systems are expected to have an uncertainty of less than 10% in these measurements.

Several reverse osmosis (RO) units are used in purification. The RO units for $H_2O$ are used only when accepting the water from the mine water supply and before it enters the main water system. The $D_2O$ is circulated and purified through two RO units.

A seeded ultrafiltration unit is used to remove $Th$, $Ra$ and $Pb$ from the $D_2O$ .

One hundred tonnes of heavy water is passed through the filter at a rate of 150 $l/min$. The filters are then removed and the $Th$, $Ra$ and $Pb$ are stripped off to count how many atoms of each type were extracted. Another method uses acrylic beads coated with $MnO_x$ which is an excellent adsorber for $Ra$ with a 90% extraction efficiency. Water is passed over the beads at 20 $l/min$ and the beads are later removed and installed in an electrostatic counter to count the $Ra$ daughters. The number of $^{222}Rn$ atoms is measured in units of six tonnes of liquid taken from one of six regions in the $H_2O$ or six regions of the $D_2O$ . The six tonnes are put through a vacuum degasser at 20 $l/min$ where $N_2$, $O_2$, $Ar$ and $CO_2$ as well as a few hundred atoms of $^{222}Rn$ are extracted. The $Rn$ is frozen out in a U-shaped trap cooled with liquid nitrogen (-192 C) and transferred to a $ZnS$ coated scintillation cell. From the number of scintillations counted in a day, the number of $Rn$ atoms in the cell and therefore the number removed from the six tonnes of liquid can be calculated.

### 2.5.2 Salt Addition/Removal

The heavy water system is capable of adding and removing $MgCl_2$ salt to enhance the neutral current detection. The concentration used is 0.2%. The system uses two polypropylene tanks. One contains a purified $D_2O$ brine solution and is emptied when the time comes to add the salt. As this is done, a second tank will accept an equal amount of salt free $D_2O$ from the AV. To remove the salt, three RO units will be used to desalinate the $D_2O$ to 100 parts per million (ppm). A second desalination pass is done using four RO units which will result in a salt concentration of one ppm.

### 2.5.3 Cover Gas System

A cover gas is used as a buffer between the water and the mine air which contains $Rn$ at a concentration of 3 $pC/l$. Boil off from liquid nitrogen fills the entire volume under the deck and above the water. To maintain a $Ra$ barrier and to keep the inside of the AV clean, a glove box is inserted over the opening at the top of the neck of the AV. The glove box allows deployment and maintainance of calibration sources stored inside it without breaking the cover gas seal.

## 2.6 Electronics

Solar neutrino interaction rates in SNO are expected to be approximately 30 intereactions per day based on the results of the Super-Kamiokande experiment [70] (assuming no neutrino mixing). Maximum detection efficiency is obtained by operating the water Cerenkov detector at as low an energy threshold as possible. The threshold is limited by the rate of background from radioactivity at low energies and the data acquisition rate. With these considerations, the acceptable data rate is expected to be on the order of a few tens of Hz, or approximately 2-3 kBytes/sec. Furthermore, interaction rates from potential nearby supernovae may be on the order of a few MHz

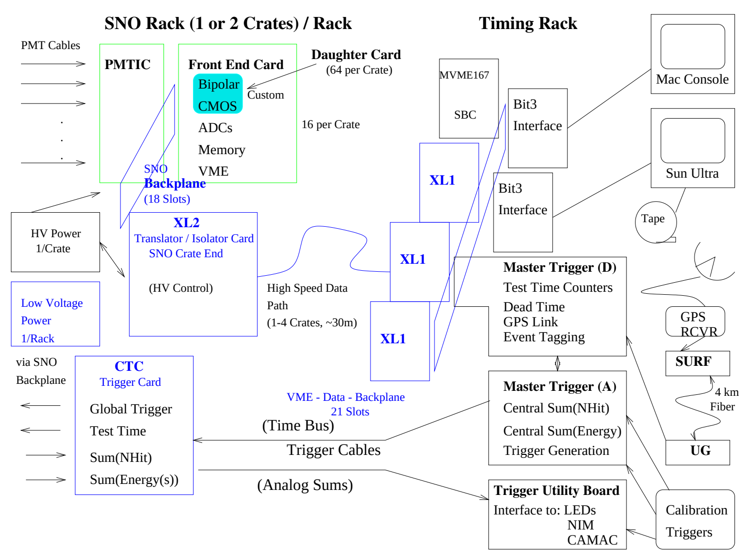

Figure 2.2: Schematic diagram of the SNO electronics and data acquisition system.

in a burst of a few tens of ms, followed by a lower rate in the tens of kHz for tens of seconds afterward. The SNO electronics have been designed to handle such rates. The system can also provide the sub-nanosecond time and wide-dynamic-range charge measurement of the PMT pulses necessary to analyze the wide variety of signals and backgrounds expected.

Figure 2.2 shows a schematic diagram of the SNO electronics system. The data flow moves from left to right. The charge pulses coming from each PMT is coupled to the front end circuitry on the PMT interface card (PMTIC) shown on the upper left. The raw signal is fed to the front end card (FEC) where custom integrated circuits process the signal and store it in the form of three charges, the relative PMT hit time, and an event identification. This information can be retrieved at the convenience of the data acquisition system (DAQ) described in Section 2.7 below.

The main trigger for SNO is called the "NHIT" trigger. When a given PMT detects a photon and the associated signal is above that channel's discriminator threshold, an integrated circuit on the FEC sends out a current pulse of fixed amplitude and 100 ns width to a summing network. After three stages of summing, a final sum of these pulses from all 9522 channels is performed on the analog master trigger card (MTC/A). Only the channels with PMTs that detected light contribute to the sum. If this sum is greater than a given programmable value, typically 30 PMT hits, a global trigger (GT) signal is sent out by the *digital* master trigger card (MTC/D) to all of the channels on each FEC. A GT signal causes the FEC to save the PMT information of any channel for which a discriminator fired up to 390$ns$ before the arrival of a GT. A common event identifier is assigned to the information from these channels. Otherwise, the data is not processed by the electronics. The MTC/D has its own event identifier and also assigns the event an absolute time. This information is stored on the MTC/D for subsequent retrieval by the DAQ.

A single board computer with an embedded central processing unit (eCPU) is in the timing rack VME crate shown in figure 2.2 at the top right. This polls the crates to see if there is data available for retrieval. If so, it reads the data from the FECs and MTC/D and writes it to a dual port memory. An "event builder" (EB) process, running continuously on a SUN Microsystems ULTRASPARC workstation (shown at the upper right hand corner of figure 2.2), reads the data from the eCPU memory. It then combines all of the PMT charge and time information for each event with the MTC/D event information and stores the entire event in its own dual port memory. A "recorder" process, also continuously running on the Sun workstation, transfers the data from the DPM to tape.

There are 19 crates of electronics each holding 16 FECs and PMTICs, a crate trigger card, translator card and two backplanes. Each FEC and PMTIC has 32 channels, thus each crate can handle up to 512 channels. 11 Racks holding either one or, more often, two crates are situated around the deck above the detector cavity.

Below is a more detailed description of the three main electronics subsystems: the high voltage, signal processing, and trigger systems.

### 2.6.1 High Voltage System

Each crate has its own PMT high voltage (HV) supply and there is a separate supply for the 91 outward looking (OWL) PMTs. The HV supply connects to the high voltage backplane (HVBP) of each crate where the HV is filtered. A second filter stage occurs on the PMTIC which plugs into the HVBP. Four selectable HV relays on each PMTIC connect HV to one paddlecard which provides a means of connecting 8 PMT cables to the PMTIC. The limitation of switching HV for groups of eight

PMTs is cost. Further control on a channel-by-channel basis is possible by inserting or removing socketed series resistors on each channel. The values of these resistors are customized for each channel to set the HV to the preferred ($10^7$) gain of that channel's PMT. The HV is delivered to the PMT on the same cable that receives the PMT signal. A Macintosh computer with the main DAQ control software controls the HV switching. Digital switching information is transferred from the timing rack VME crate through the XL1 and XL2 translator cards and to the HVBP. Buses on the HVBP move the switching signals serially through registers on each PMTIC in the crate until the correct one is reached. A separate load bit then loads the local HV control register switching the relays for that PMTIC. The system can operate as few as one or as many as all 64 relays in the crate with a single operation. The DAQ system also acts as a control system for the HV supplies. The information for turning on the supply, ramping up the voltage as well as monitoring the HV value is passed to the HV supply via a cable from the XL2 card. The SNO HV system was designed, built and tested, largely, by this researcher and is described in more detail in Appendix B.

### 2.6.2 Signal Processing

The PMTIC interfaces the electronics with the PMTs. The PMT coaxial cables (RG59 75$\Omega$) are attached in groups of 8 to small paddlecards. Four paddlecards plug into each PMTIC making up 32 channels. The PMTIC provides input termination and HV protection. A one-to-one isolation transformer on the PMTIC provides coupling to the front end circuitry on the FEC.

The FEC receives the raw PMT signal from the PMTIC and routes it to two application specific integrated circuits (ASIC) chips - the “SNOD” and “SNOINT” which perform discrimination and integration respectively. Three separate integrations are done on the PMT pulse: high gain, long and short integration times and a low gain integration that can be switched from long to short time by setting an external bit. The long integration time is on the order of 100 ns and the short is a few tens of ns. The high and low gain charge measurements provide an economical means to obtain a large dynamic range. The extended time integral may prove useful for including more reflected light, thereby improving the energy measurement. The other quantity that is measured is the time difference between the time the discriminator fired and the arrival of the common stop global trigger signal. This time difference is converted to a voltage via a time-to-amplitude converter (TAC). The TAC and analog memory for storage of the charges and TAC value are located on a CMOS chip. Each SNOD and SNOINT chip has four channels and the CMOS chip has one. All of the chips required for eight channels reside on a single daughter card. The daughter cards plug into sockets on the FECs.

An FPGA sequencer and a FIFO controller oversee data storage to 4MByte of digital memory on each FEC as well as data retrieval by the DAQ. The sequencer and FIFO controller programs can be changed by burning a new PROM and installing it on the FEC.

PMT charge simulation is available via Charge Injection (CI) circuitry on the PMTICs. A differential pair amplifier which can be selected externally on a channel-by-channel basis and can be programmed in both pulse height and width, injects a square pulse of charge into the FEC with a range of 0-120 pC (equivalent to 0-100 photoelectrons). This system is used to calibrate the pedestals and slopes of the time and charge measurements. Electronics calibrations are discussed in Section 2.8.

### 2.6.3 Trigger System

SNO uses an analog trigger sum of hit PMTs as its main trigger; it is referred to as the NHIT trigger. Each time a FEC discriminator fires a trigger (current) pulse of 100ns width and a fixed amplitude is generated by the CMOS chip and fed to an analog summing network on the daughter card. Summing stages occur on the FEC (32 channels), crate trigger card (512 channels from 16 FECs) and finally on the MTC/A (all 9522 channels). The final signal is a real time *analog* sum of 9522 channel's 100ns wide trigger pulses. A threshold can be set such that the whole detector will trigger if the instantaneous pulse height of this sum crosses the given value. A separate system with a programmable width near 20ns exists and is used to study events occurring in small volumes of the detector. That region can be offset from the center by programming delays to each channel.

Another trigger signal is an analog sum of the PMT charge pulses themselves - known as the “energy sum” or ESUM trigger. This trigger can be used to cut on very high charge events, either in a few PMTs or in the whole detector. Uses include cutting to find muon events, and perhaps events due to radioactivity in the PMT glass. Outward looking tube NHIT and ESUM triggers for monitoring the light outside the detector are available. Synchronous and asynchronous external trigger inputs are provided which triggered sources can use to cause global triggers every time the source fires. The NHIT trigger can be prescaled by external programming from the data acquisition system.

A global trigger mask word is set which has a bit reserved for each type of trigger that fired during a given event. The DAQ provides an interface so that one can choose which of the bits (or group of them) will cause a global trigger, the other bits are then just spectators to be used in analysis.

### GPS Timing System

Precise timing is important for SNO especially in the event of a supernova. Consequently SNO timing is synchronized to a global positioning satellite (GPS) system. A 10MHz clock keeps time with a pulse from the GPS system (detected via antenna on the surface and converted to a light pulse and sent underground via fiber optic cable) while a 50MHz clock keeps the inter event time to an accuracy of 20nsec. The two clocks are synchronized every so often via fiber optic communication with the surface, corrected for the round trip delay of light pulses.

### 2.7 Data Acquisition System

The Data Acquisition System (DAQ) operates from a Macintosh computer on the deck. The computer can be controlled from either the underground or surface control rooms. The custom built software package, SHARC, has an extensive graphical user interface (GUI) for ease of operation. An embedded central processing unit (eCPU) is located in a VME crate in the timing rack. It receives data via a VME interface which communicate through seven XL1 (translator) cards to all of the FECs and to the trigger system. Crates, and FECs within a crate, are read out sequentially. The FEC information and the trigger information from the MTC/D are stored in separate buffers in the dual port memory (DPM) of the eCPU. An event builder process, running on a SUN workstation on the deck, processes the data into events and sends the information to a recorder process which writes the data to a disk file and to tape. The eCPU pauses readout of the front end if the SUN workstation has not emptied the DPM in time. Data is written to tape in two places: underground and above, before it is erased from the disk of the SUN computer that runs the event builder and recorder software. Copies are made from one of the two originals for each institution.

## 2.8 Calibrations

Many calibration sources are planned for SNO. They can roughly be divided into the categories of PMT, optical and energy calibration sources. Each is dealt with individually. First, however, the calibration source manipulator is described.

### 2.8.1 Calibration Source Manipulator System

Deploying calibration sources at various locations in the detector is accomplished using a calibration source manipulator system. It is a computer-driven series of ropes, pulleys, springs and other mechanical and electrical equipment which can move a given calibration source to most points in the x-z and y-z plane of the detector inside the AV. Sources attach to the manipulator easily inside a glove box centered over the AV. A set of ropes are anchored at various points inside the AV and weights are used to control the location of the source. Each source has an "umbilical" which delivers any electronic signals (or gas capillaries) to and from the source. The manipulator system is designed to take up or let out the slack in the umbilical as the source is moved from place to place.

### 2.8.2 Electronics Calibrations

The conversion from the raw digital information of the three charges and time to the units of nanoseconds and photoelectrons is a two step process. First, the charge injection circuitry on the PMTIC is used to inject charge into each channel. These electronics calibration events are used to convert the raw times to nanoseconds. Second, the conversion of the raw charges to photo-electrons and the establishment of a zero of time is done with an optical source (laserball and sonoluminescence sources) at the single photoelectron level (see below).

In the first stage, varying amounts of charge are injected to obtain a charge slope. To obtain a time slope, the firing time of the injected pulse is delayed by varying amounts relative to the enforced trigger time. Pedestals, or the values of the raw charges and times with no charge input, are measured by gating each channel and forcing a trigger when no source is present in the detector. Spurious background sources are still present but the pedestals can be determined when no high voltage is on the PMTs preventing light from such sources from interfering. Pedestals with and without HV are in very good agreement, however.

In run mode, the pedestals and other electronics calibrations are done periodically while taking neutrino data.

Further calibrations are necessary for dependencies due to discriminator walk and high charge time shifts caused by photons arriving at the early edge of the PMT transit time jitter curve. Such effects are calibrated using a laser optical source at high occupancy.

### 2.8.3 Optical Calibrations

The laserball is the optical calibration source. It is a triggered source with nearly monochromatic light output which can be changed to many different wavelengths with the use of dye cells. It can be located at many positions inside the AV using the manipulator, or outside the AV along a vertical line nearly tangent to the AV at its equator.

The SL source was originally developed to check optical calibrations. However, it has the unfortunate limitation that it is not monochromatic. Furthermore, the spectrum and intensity of the source is not known pulse-to-pulse and day-to-day. Because of these factors the absorption and scattering length variations with wavelength are not obtainable. It might be possible to obtain an estimate of the wavelength averaged extinction coefficients, but it would not be very accurate because of the errors in the intensity and spectrum of the SL light. Unfortunately, the effort was abandoned on these grounds and all optical calibrations described below could be done with the LB.

#### Extinction Coefficients of the Acrylic, $D_2O$ and $H_2O$

The precise intensity of the laserball source is not known pulse-to-pulse. The absorption coefficients are obtained by taking data at many different positions. The possible path lengths in each medium ($D_2O$, $H_2O$ and Acrylic) traversed by a photon originating at the source and detected by a given PMT are estimated with Monte Carlo. Moving the source to specific locations will change the path lengths in each material by the estimated amount. Given this information, the expected relative change in intensity at each PMT for each source location can be calculated. A fit to the data gives the absorption and scattering lengths in each medium.

### 2.8.4 Energy Calibrations

There are two energy calibration sources designed for the SNO experiment: the $^{16}N$ source and the p-t source. These sources produce monoenergetic gamma rays of low and high energy respectively.

The $^{16}N$ source is the most important energy calibration source. It uses a DT generator neutron source to deliver neutrons to a target of $CO_2$ gas resulting in the reaction:

$$^{16}O + n \longrightarrow ^{16} N + p, \tag{2.1}$$

where the $^{16}N$ subsequently decays via the following reaction:

$$\longrightarrow ^{16} O + \gamma + e^{-} + \overline{\nu_e}. \tag{2.2}$$

The gamma is either 6.13 MeV (68%) or 7.12 MeV (4.9%). The beta (electron) acts as a trigger (the source has a scintillator and PMT to detect the light from the beta).

The steel casing of the decay chamber is thick enough to stop the electron while allowing the $\gamma$ to escape. The half life of $^{16}$N is about seven seconds and the source is designed to operate at roughly 50 Hz.

Monoenergetic gamma rays of higher energy are obtained via a miniature accelerator source. The "pT" source uses the $^{3}H(p,\gamma)^{4}He$ reaction producing 19.8 MeV gammas. The *pt* source which has been tested and awaits commissioning. It operates at roughly 20 kV and will produce approximately 1 gamma per second.

The $^{16}N$ source is deployed using the manipulator, and can be located anywhere in the (x,z) or (y,z) planes inside the AV, or it can be located along a vertical line in the light water outside the AV. The p-t source can be located anywhere on the vertical axis of the AV.

### 2.8.5 Electron and Neutron Response Calibrations

#### Electron Sources

The $^{8}Li$ source is another gas transport source. $^{8}Li$ is created via $^{11}B$ in the following reactions:

$$^{11}B + n \longrightarrow ^{8}Li + \alpha, \tag{2.3}$$

and

$$^{8}Li \longrightarrow ^{8}Be(2+) + e^{-} + \overline{\nu_e} \tag{2.4}$$

and

$$^{8}Be(2+) \longrightarrow \alpha. \tag{2.5}$$

The walls of the source are thin enough that the beta escapes with little energy loss (250 KeV at normal incidence). There is a counter wire with a signal wire at both ends on the axis of the cylindrical source. This detects the alphas and "reconstructs" the event by charge division between the signals at each end. The expected event rate is 1 Hz.

The advantage of using this source is that the beta spectrum for the $^{8}Be$ is similar to that of $^{8}B$, the solar nuclear reaction that produces most of the neutrinos detectable at SNO. This source will provide a reasonable simulation of the CC response of the detector.

### Neutron Sources

The $^{17}N$ source operates similarly to the $^{16}N$ source but uses enriched $^{17}O$ gas as the target resulting in the reactions:

$$^{17}O + n \longrightarrow ^{17}N + p, \tag{2.6}$$

and

$$^{17}N \longrightarrow ^{16}O + e^{-} + \overline{\nu_e} + n. \tag{2.7}$$

The $^{17}N$ has a 4 second half life and, again, there is a delayed coincidence with a beta which acts as a trigger from the source scintillator. The source should operate at about 10 Hz.

### 2.8.6 Angular Resolution

Angular resolution calibrations are done with the $^{16}N$ gamma source. The gamma event positions are estimated via reconstruction algorithms. For events that reconstruct further than $1.5m$ from the source, a histogram of the angle between the line connecting the reconstructed and source positions, and the line connecting the reconstructed position and each PMT that was hit, is constructed. This histogram peaks near $0°$ and the width (FWHM) is a good estimate of the angular resolution. Angular resolution is a function of the position in the detector and the energy of the gamma ray. Only the former dependence can be studied with the $^{16}N$ source by moving the source to various locations.

## 2.9 Detector and Physics Monte Carlo Simulations: SNOMAN

An extensive Monte Carlo and analysis software package has been developed by Oxford University and others in the collaboration. The package has been named SNOMAN for SNO Monte Carlo and analysis. It is currently capable of generating Monte Carlo simulations of any of the data sets and interactions needed for SNO analysis except hadronic interactions. SNOMAN can also be used to read in the data files and perform a full calibration on it. It is a multi-purpose tool which has been verified on all the computer platforms being used in the collaboration.

In addition to SNOMAN there is a CERNLIB HEPDB-based database called SNODB which stores all of the calibration data for each electronics channel, PMT, etc. It can be accessed from SNOMAN to calibrate the raw data as it is read in. A system of master and slave nodes has been set up to assure that all versions are the same at a given time.

### 2.10 Summary

SNO is a unique solar neutrino detector which is capable of providing direct evidence of solar neutrino oscillations. Great care has been taken in minimizing the backgrounds in SNO to increase the sensitivity to the neutrino signals.

The detector has been described including all of the important subsystems. A complex detector such as SNO requires detailed calibrations in order to make sure the data, uncertainties, and systematic effects are well understood. SL sources were developed to perform some of these calibrations. These experiments and their analyses brought to light some detector pathologies that might have otherwise gone unnoticed. Discussions of these issues are included in the following chapters.

# Chapter 3

## Sonoluminescence: Experimental and Theoretical Methods

The history, characterization and theory of sonoluminescence (SL) have been discussed in Chapter 1. This chapter will describe the experimental and theoretical methods used to perform and analyze the experiments undertaken for this thesis. Two sonoluminescent sources which have been developed by the author are described in Section 3.1. A description of the SL experimental setup and means of obtaining SL in the laboratory are presented in Section 3.2. Section 3.3 presents some initial data and describes some of the issues involved in its analysis. Section 3.4 shows the result of measurements of PMT timing accuracy performed with the SL source. The result is compared to measurements performed with the standard SNO optical calibration source, the “laserball” (LB). Section 3.5 describes photon correlation functions which are used for all of the subsequent analyses presented. Finally, Section 3.6 describes how the correlation functions described in Section 3.5 are applied to the analysis of the SL experimental data. The analyses of these experiments is presented in Chapter

4.

### 3.1 SL Sources

Two sonoluminescence (SL) sources have been developed for studies of the SNO detector. Possible utilizations of these sources for SNO include: measurements of PMT timing accuracy, detecting and correcting some detector pathologies, single photoelectron calibrations of the SNO PMTs, simulation of high data rates expected for a nearby supernova and monitoring changes in the detector optical properties as a function of time. This thesis covers only the first two of the topics mentioned above, however, the others may be attempted in the future. The sources have also been used to investigate some fundamental properties of SL. These include back-to-back photon correlations, the angular distribution of the emitted photons, and an attempt to determine the SL spot size (the size of the light emitting region of the SL bubble) using "intensity interferometry", the method of Hanbury Brown and Twiss (HBT) [71, 72].

Both SL sources are spherical quartz flasks filled with water. Two peizo-electric crystals are attached diametrically opposite each other on the equator of the flask. A nichrome ($NiCr$) filament (not shown), immersed in the water, is used to introduce an air bubble. Electrical signals for the crystals and filament are routed to the source via an "umbilical" consisting of a silicon sleeve covering the signal cables. The umbilical

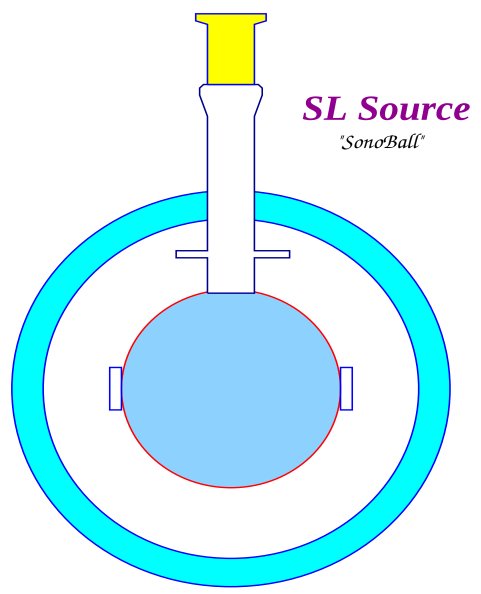


Figure 3.1: The water fill SL source. Note the outer acrylic shell to keep the inner flask away from the heavy water. The peizo-electric crystals are shown on the right and left hand sides of the equator on the inner flask.

extends up through the neck of the acrylic vessel, through the cover gas glove box, and out to the deck where it attaches to a signal generator and DC power supply.

The first source was used before any water had been added to the detector and is therefore known as the "air fill" source. The second source is designed to be immersed in the heavy or light water and is referred to as the "water fill" source [68]. Figure 3.1 shows a schematic drawing of the water fill SL source. It has an inner volume of $250ml$ filled with water. This is surrounded by a spherical shell of $\sim$0.75 cm thick ultra-violet absorbing (UVA) acrylic with a 7 inch outer diameter. The purpose of this shell, obtained from the same company that built SNO's acrylic vessel (AV), is to shield the inner flask from the $D_2O$ as the source must operate in a medium with a density much less than that of the water inside the flask so that standing acoustic waves can be set up inside the flask. The water fill source operates best at a frequency of 32 kHz. The water fill source has a small PMT (Hammamatsu R5600) attached inside the acrylic shell for use as a trigger and to measure of light intensity output near the source.

The air fill source is the only source used to take data for this thesis. Due to time constraints, all the data were taken before water had been added to the detector. The volume of water filling the air fill source is 1 liter. The source operates best at a frequency of 23.4 kHz.

### 3.2 SL Source Operation

Below is a brief guide to obtaining SL in the laboratory. For more careful discussions on the resonances and detailed aspects of operation see the references [56, 50]. A diagram of a simple experimental setup for SL is shown in Figure 3.2. This setup does not reflect some improvements that were made in terms of remote operation. It is meant to highlight the salient features of SL source operation.

Both sources operate in the same fashion: an AC signal is applied to the peizo-electric crystals using a series LC matching circuit, to tune the electrical resonance to the acoustic resonance of the spherical vibrational mode of the flask. The crystal

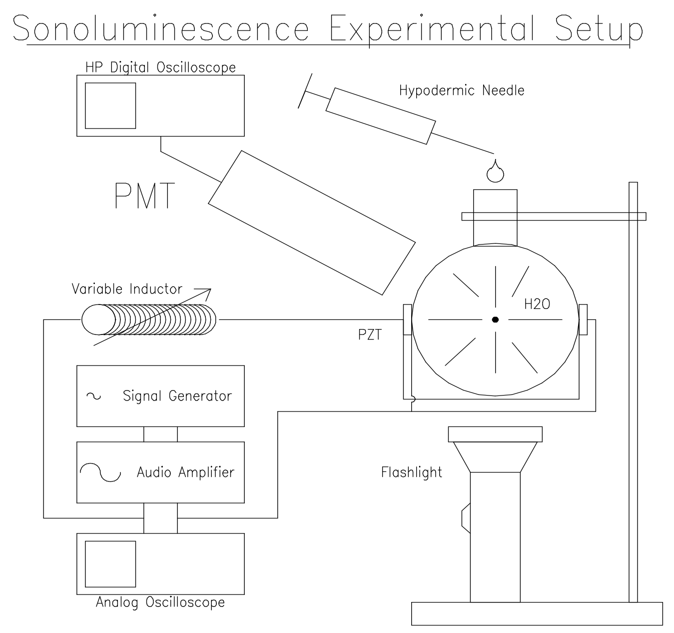


Figure 3.2: SL Experimental Setup

vibrations excite the mode. If an air bubble is introduced into the water it will move to the center (provided one is operating at one of the monopole modes of the flask and the amplitude of the signal is properly tuned) and start vibrating in its own monopole mode. When the frequency and amplitude of the signal are tuned to precisely the right values, the bubble will emit a blue light that is visible to the naked eye (in a darkened room). The light is pulsed, with one pulse per period of the exciting signal.

The diagram in figure 3.2 shows a hypodermic needle introducing a drop of water which, due to surface effects, causes an air bubble to be formed. This system was modified for remote operation. For the work described in this thesis, bubbles are introduced by charging a set of capacitors to $\sim$100V and then discharging the capacitors through the aforementioned $NiCr$ filament, resulting in localized boiling of the water. This allows dissolved air in the water to come out of solution and to form a group of bubbles. The bubbles move to the center of the flask. If the sound field is on resonance in the monopole mode, the bubbles coalesce there to form a single bubble.

Operation of the source is straightforward and systems have been developed that allow remote operation. The only difficulty is that the water must be degassed such that the partial pressure of air is on the order of a few tenths of a percent [73] or the bubbles will behave unstably. The result is unstable light intensity or no light emission at all. Degassing is performed before the source is installed in the detector. It is accomplished simply by connecting a vacuum pump to the sealed source. It typically takes 30 minutes to degas the air fill source (1 $liter$) and approximately 5 minutes for the water fill source ($250ml$). No means of measuring the partial pressure of air after degassing was used. If it is to be used further, this is an improvement that should be made to the system. Remote degassing will also be necessary before the source is deployed into the detector the next time. This will require minimal modifications to the existing hardware. The umbilical already has a tube in it for this purpose.

After degassing, the water must come back to a steady temperature before SL can be achieved as the resonant frequency of the flask is a function of the speed of sound in water, which is in turn a function of temperature. Temperature drifts affect the light intensity and can cause loss of SL light but this happens on the scale of tens of minutes or hours. The frequency can be adjusted as the temperature changes during operation and, in practice, it is not difficult to operate the source over a time period of many hours.

## 3.3 SL Data: A First Look

The SL sources and their operation have been described in the previous section. Below is a first look at some SL data taken with the SNO detector. The presentation will proceed from the raw form of the data towards the more usable form used in analysis.

### 3.3.1 NHIT and NHIT vs. Time

Figure 3.3 shows a plot of the "NHIT" distribution for SL run 179 taken on May 6, 1998 when the SNO detector had no water in it ("air fill", as in all of the data shown in this thesis). "NHIT" is defined as the number of PMTs hit in a given event. This quantity is used as the main trigger for solar neutrino data in SNO (see the discussion in the trigger system section in Chapter 2). The source was placed within 25 cm of the center of the detector, turned on, and left running for approximately 30 minutes. The "NHIT100 Medium" trigger prescaled by a factor of 1000 was used (see discussions of the trigger system in Chapter 2). Prescaling was necessary because the electronics and data acquisition system (DAQ) are not designed to handle sustained

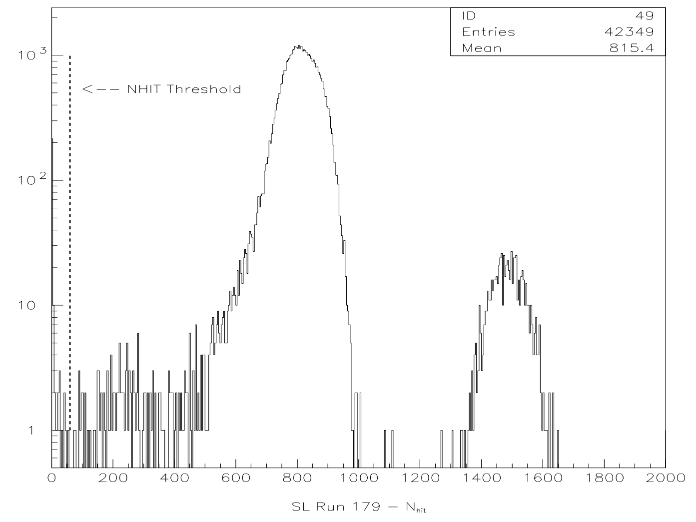


Figure 3.3: SL Run 179: Raw NHIT Distribution. The dotted line represents the NHIT threshold setting.

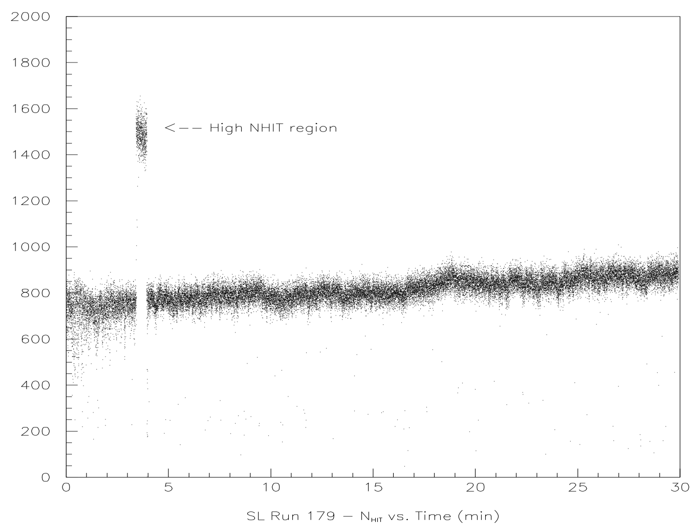


Figure 3.4: SL Run 179: Raw NHIT vs. Time (min.)

event rates of tens of kHz. Thus, only the data for every thousandth SL event was saved. There were 5511 electronics channels connected and working at that time, representing 58% of the total number of electronics channels.

The NHIT distribution is shown on a log scale to highlight all of the features. The salient features are:

(1) the distribution is not clean,

(2) the main peak, near $NHIT = 800$, is a skewed towards low NHIT *i.e.* the shape is not Gaussian and

(3) there is a high NHIT peak near $NHIT = 1500$ separated from the main peak.

The following discussion will explain these and other features of the data.

The entries at low NHIT ($NHIT < 400$ and predominantly $NHIT = 0$) are due to systematic effects in the DAQ at the time these data were taken which have since been corrected. They do not accurately represent the true NHIT for the associated events. It is known that the low NHIT events are not caused by real events with that many hits because the NHIT trigger threshold was set to approximately 60 hits as shown by the dashed line in Figure 3.3; events with fewer than this number of hits were discarded at the electronics level - before the DAQ and event builder.

Insight can be gained by comparing the NHIT distribution in Figure 3.3 to Figure 3.4 which shows NHIT vs. event time, where event time is measured in minutes since the start of the run. One can see the low NHIT events as a sprinkling of dots below the main group. Other things to notice are the instability of the SL at the beginning of the run and that the NHIT is slowly rising during the run. It starts out at 750 and at the end of the run it reaches an average value of 850. This is the reason why the main NHIT peak in Figure 3.3 is skewed towards low NHIT. Another feature is the small wiggles in the NHIT vs. time curve which show that the mean intensity is fluctuating on time scales of tens of seconds to minutes. The most prominent feature in Figure 3.4 is labeled a "high NHIT region". The SL intensity suddenly jumps from one steady value near 750 by almost exactly a factor of two, to 1500 over a very short time. This is due to an intentional manual increase in the drive voltage of the signal generator which was lowered to its original value 30 seconds later.

A SNOMAN 3.01 Monte Carlo simulation of SL (during air fill) was carried out to determine the number of photons detected (in air fill) for a given number emitted. This results in that approximately 3% of the SL photons emitted actually get detected. Breaking this up into its components: 45% are lost due to the limited PMT effective coverage of 55%, roughly 20% reduction comes from the PMT quantum efficiency and the rest are lost due to absorption and reflections. For an average NHIT of $\sim 800$ as shown in Figure 3.3, the number of photons emitted in a single flash of SL can be estimated:

$$N_\gamma = \frac{\overline{NHIT}}{\epsilon} = \frac{800}{0.03} \sim 26,000 \ photons \ per \ flash, \tag{3.1}$$

where $\epsilon$ is the 3% overall efficiency for photon detection. Of course, during the high NHIT portion of the run the intensity was a factor of two higher - $\sim 50k$ photons per flash. These numbers are small compared to the values published in the literature of $10^5$ to $10^6$ photons per flash [56, 50]. However the values quoted elsewhere are generally near the high intensity threshold of SL. This run was performed near the lower threshold as it was desired to be near the single photoelectron level of the PMTs. In fact the source intensity could have been turned much higher and intensities a factor of 8 higher ($\sim 200k$ photons per flash) have been observed.

To operate in the single photoelectron regime, the following condition must be met:

$$NHIT <\sim 5\%\ NPMT = 0.05 \times 9522 \sim 476. \tag{3.2}$$

The probability that a single PMT will be hit in a given event is the ratio of NHIT to NPMT, or 5% if the above condition is met and the light is isotropic. This is known as the average "occupancy" of the detector which is equal to the average occupancy of each PMT assuming the light is isotropic. At such low rates, Poisson statistics apply. The probability of a PMT registering two photoelectrons can be calculated to be:

$$P(n=2) = \frac{\lambda^2}{2!}e^{-\lambda} = \frac{\lambda}{2}P(n=1), \tag{3.3}$$

where $\lambda$ is the average occupancy of the PMT. Thus the probability that a PMT will register two photoelectrons is a factor of $\lambda/2$ times the probability that it will register one. Small values of $\lambda$ assure that PMTs are detecting single photoelectrons the vast majority of the time. The probability of more than one photoelectron being detected by a PMT in a given event is negligible if $\lambda$ is small. Thus operation at low occupancy, assures that one is operating in the “single photoelectron” regime. For $\lambda = 5\%$, the probability that a single photoelectron registers in a PMT is 40 times the probability that two will register in a given event. All of the data taken for this thesis, except where noted, was taken at occupancies of less than 15%.

To provide contrast to the relatively stable light intensity shown for run 179, consider Figure 3.5. The figure shows a plot of NHIT vs. time for run 1279 taken in August, 1998. The SL source could not be degassed (a critical prerequisite for stable SL) before the run. As a result, the light intensity was unstable. One can see from the plot that there are intensity fluctuations of up to a factor of 10 over intervals of a few seconds along with smaller fluctuations. Regions of relative stability, normal and high NHIT are shown. Comparison of the stable run 179 in figure 3.4 and the unstable run 1279 in figure 3.5 shows the extremes of sonoluminescence behavior due to proper and improper degassing respectively. When the source is properly degassed, one can see visually that the bubble is perfectly still, with no observable motion. When too much air is in the water, however, the bubble oscillates about the center of the source and the shape of the bubble becomes unstable. Many bubbles may form for short periods of time before coalescing again. This behavior leads to light intensity fluctuations as seen in figure 3.5.

NHIT cuts can be performed on the data such that unwanted non-SL events are discarded. Such a cut might be to cut everything below 400 and above 1000 in run 179 (see Figure 3.3) to analyze events only in the main peak. Another possibility is to cut events below $NHIT = 1200$ to analyze the high NHIT portion alone. These cuts are carried out on an event by event basis, as are the event time interval cuts discussed below.

### 3.3.2 Time Interval Between Events

Another event level cut is possible due to the synchronism of SL. SL pulses occur at fixed time intervals and if a non-SL event occurs it is likely to occur at a different interval. Figure 3.6 shows the time between events for SL run 179. Note that the vast majority of adjacent event time differences occur at 42msec which is 1000 times the SL period, $\tau_{SL}$. The factor of 1000 is due to the aforementioned prescaling of the detector trigger. If the interval between two events is not $1000\tau_{SL}$, it has to be decided which one (if not both) is non-SL and discard it.

### 3.3.3 PMT Hit Time and Charge

Figure 3.7 shows a PMT hit time histogram, calibrated according to the procedures discussed in Chapter 2, Section 2.8, for the same SL run. This histogram represents PMT hit level data rather than the event level data described above. There is an

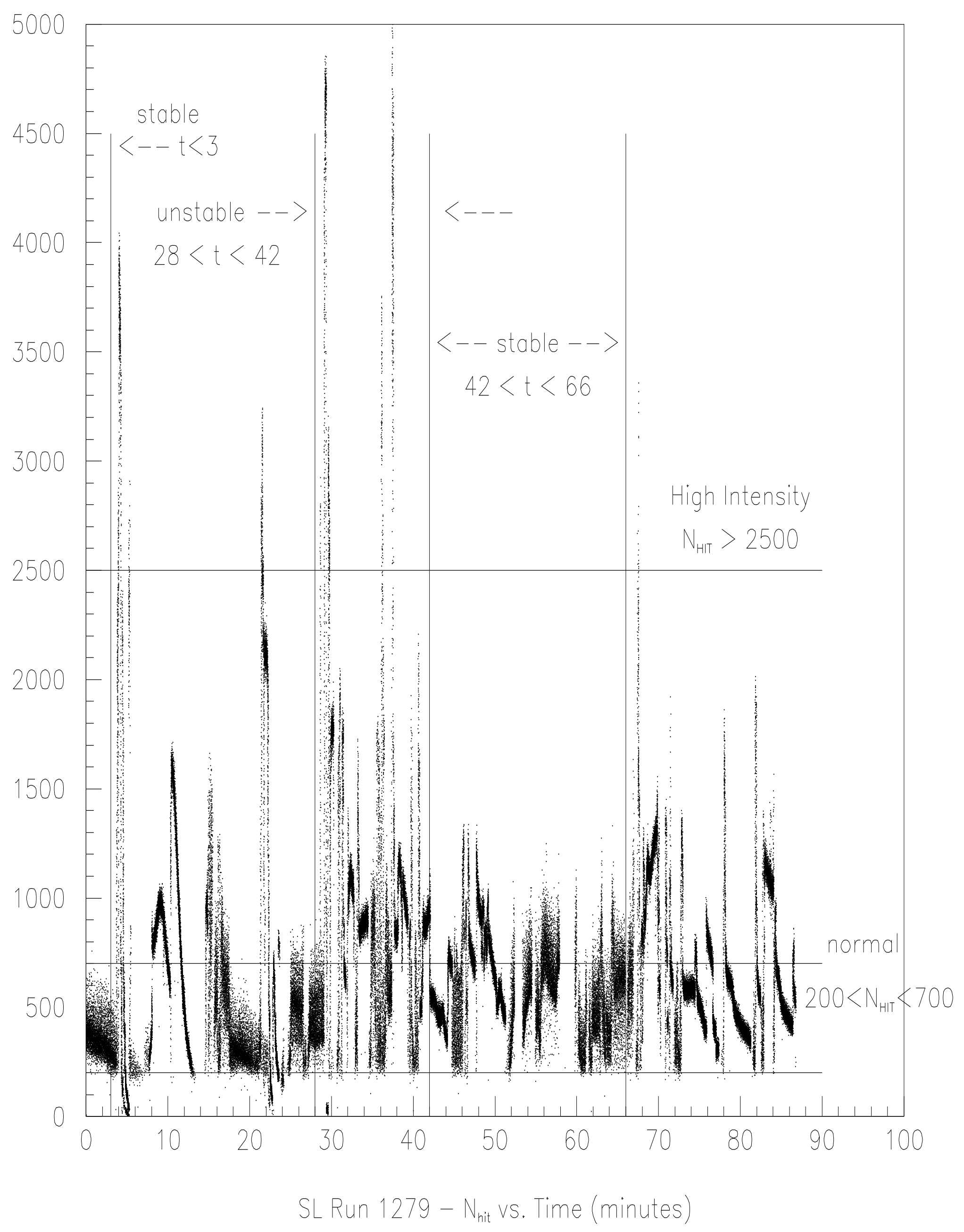


Figure 3.5: SL Run 1279 unfiltered light, full detector - $NHIT$ vs. $t_{event}$. Source could not be properly degassed before the run resulting in bubble-, and therefore intensity-, instability.

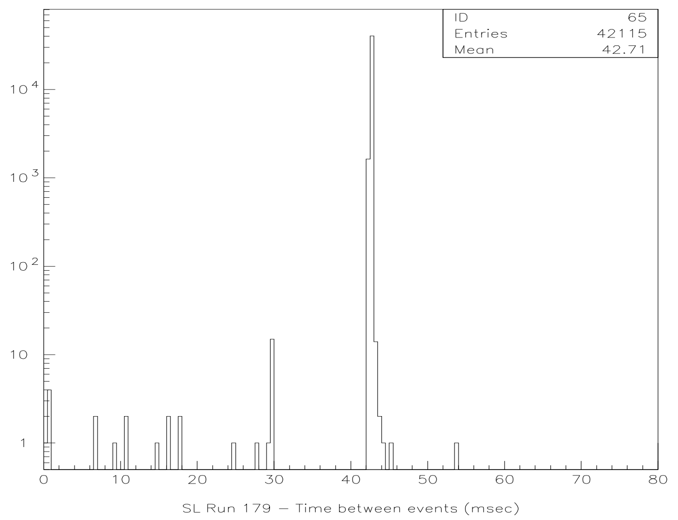


Figure 3.6: SL Run 179: Time between events, $\Delta t_{event}$ in $msec$. If adjacent events occur with $\Delta t \neq 1000\tau_{SL}$ then they can be cut as they are probably not SL events.

entry for each photon that produced a signal in a PMT during the entire run 179. The time is in $ns$ with an arbitrary offset. To understand this histogram and the following discussion, it is important to remember that the SL source was at the center of the detector during the run. The time spectrum in Figure 3.7 has three features worth noting.

First, the bulk of the detected light occurs between approximately 68 and 83 ns (denoted by the dashed lines) on the plot and is labeled “direct light peak”. This is light that took a direct path from the source to the PMTs without reflecting. The small peak at $\sim 60ns$ is due to imperfect calibrations of a small number of electronics channels at the time these data were taken which has since been corrected.

The second thing to notice are the two sets of reflection peaks which are labeled. The first set is due to reflections off the acrylic vessel (AV) and the PMTs themselves; in both cases the photons travel back across the detector and are detected on the opposite side. The AV reflection peak occurs at $\sim 115ns$ and the PMT reflection peak occurs at $\sim 131ns$. The time difference between these peaks and the direct light peak is simply the crossing time of the detector for the PMT reflection case, $\sim 56ns$ in air. For acrylic vessel reflections the time difference is less by approximately 5 $meters/c$ $\sim 16ns$ since the AV is approximately $2.5m$ from the PMT support structure (PSUP). The second order peaks are similar, but these photons are not detected after the first reflection. Instead, they undergo a second reflection (again, either at the AV or PSUP) and move back across the detector in their original direction. The time difference is another $40ns$ or $56ns$ (detector crossing time).

Finally, note that the heights of the peaks are separated by almost exactly an order of magnitude. The first order peaks are down by a factor of 10 and the second order peaks by a factor of 100 compared to the direct light peak. This gives an idea of how much light is reflected during air fill. When the detector is filled with water, the reflection peaks are less prominent because the indices of refraction of the PMT glass and AV are closer to that of water than they are to the index of refraction of air.

The charge spectrum in pedestal subtracted ADC counts for the high gain, long

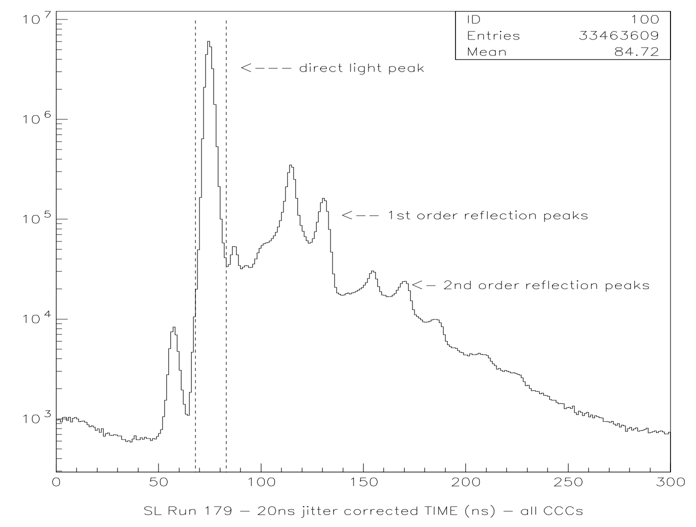


Figure 3.7: SL Run 179: PMT hit time (ns) with arbitrary time offset. Note the direct and reflected light peaks.

integration time, charge signal (QHL) is shown in Figure 3.8. An event time cut was used such that only the low NHIT portion of the data (see Figure 3.4) were used. The charges for every PMT hit and of all PMTs are included in the histogram. There are approximately 40 ADC counts per photoelectron for the high gain charge measurements. The peak occurs at roughly 25 counts which corresponds to approximately 0.6 photoelectrons. The mean is 67 counts which is 1.7 photoelectrons. The source is operating above the single photoelectron regime as the occupancy for most of this run, run 179, is:

$$Occupancy = \frac{NHIT}{NPMT} \sim \frac{800}{5300} \sim 15.2\%. \tag{3.4}$$

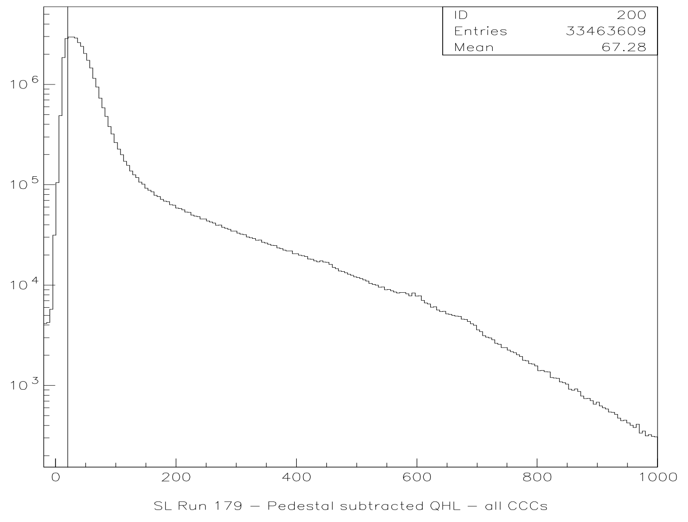


Figure 3.8: SL Run 179: PMT Charge (QHL) in pedestal subtracted ADC counts. There are approximately 40 ADC counts per photoelectron.

Simple PMT hit time cuts can be made where the dashed lines appear in Figure 3.7 ($68ns < t_{PMT} < 83ns$), accepting only the direct light. Such a cut removes reflected light and most scattered light from the data set. This is desirable for the analyses described in this thesis. Typical charge cuts are: $QHL > 0.5PE \sim 20$ ADC counts. This low charge cut decreases sensitivity to threshold effects due to differences in the discriminator thresholds from channel-to-channel as well as reducing the contribution from PMT noise.

### 3.3.4 SL Data With Combined Cuts

To illustrate how the data appears when all of these cuts are applied, a simple NHIT plot for SL run 179 was made with the following cuts:

(1) $400 < NHIT < 1000$ (see Figures 3.3 and 3.4),

(2) $11minutes < t_{event} < 16minutes$ (see Figure 3.4),

(3) $40msec < \Delta t_{event} < 50msec$ (see Figure 3.6),

(4) $68ns < t_{PMT} < 83ns$ (see Figure 3.7), and

(5) $QHL > 0.5PE \sim 10ADCcounts$ (see Figure 3.8).

The resulting plot is shown in Figure 3.9. This plot should be compared to the plot in Figure 3.3. The average NHIT is lower in Figure 3.9 because only the direct light photons are contributing, due to the $t_{PMT}$ time cut. A Gaussian fit to the data and the fit parameters are shown. The fit is excellent, with a $\chi^2$ per degree of freedom of $\chi^2/DOF \sim 0.9$. Notice that the standard deviation of the fit is only slightly larger than the square root of the mean, the ratio of the two is: $\sigma/\sqrt{NHIT} \sim 1.1$, showing that during this 5 minute time interval, the number of emitted photons was nearly constant from pulse-to-pulse. As can be seen from Figure 3.4, the NHIT steadily increased over time during the run. If a similar plot to Figure 3.9 were made over a shorter time interval, a Gaussian fit would result in an even smaller standard

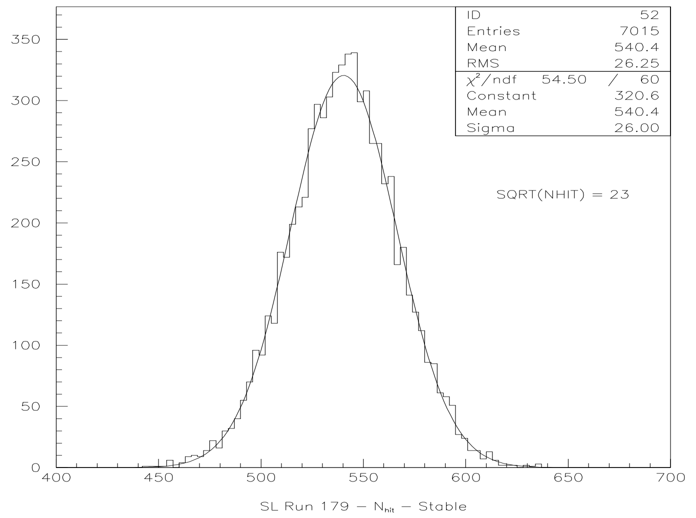


Figure 3.9: SL Run 179: NHIT Distribution for $11min. < Event\ \ Time < 16min.$ after NHIT cuts. Also shown is a Gaussian fit and fit parameters. The $\chi^2$ per degree of freedom is just less than 1. The ratio of the fit deviation to the square root of the mean is: $\sigma/\sqrt{NHIT} \sim 1.1$, showing that the SL over this time period had very stable in intensity.

deviation. The comparison of the Figures 3.3 and 3.9 shows that reasonable cuts can significantly clean up the data, ensuring the integrity of the data while minimizing backgrounds.

### 3.4 PMT Timing Residuals

Some initial SL data has been shown above to give the reader some familiarity with its features. In this section, it will be described how the SL source has been used to measure the timing accuracy of the SNO detector PMTs. The results are then compared to the same calibration carried out with the "laserball" (LB). The LB is the standard SNO optical source and is described in the references [69, 68].

Timing is important in water Cerenkov detectors. The relative arrival time of photons striking the PMTs is used to reconstruct the location of the event that produced the light or to reject background. Good timing resolution gives good reconstructed event position accuracy.

An optical light source is placed as close to the center of the detector as possible. The source should have a pulse width which is short compared to the PMT rise time which is approximately $5ns$ for the SNO PMTs. The SL source has a pulse width in the range: $30ps < PW < 300ps$ [51, 52, 53]. The nitrogen laser which is the source for the laserball has a pulse width of $600ps$ [69]. The dispersion due to scattering in the diffuser ball of the LB system is approximately $1ns$ [69].

Data is taken with the light source, operating until each of the 9522 PMTs takes part in at least 1000 events. The analysis is carried out using a "time fitter", part of the SNOMAN software described in Chapter 2, Section 2.9. The time fitter reconstructs the position and event time of the source using the relative timing of the PMT hits in each event. This is accomplished by minimizing the $\chi^2$:

$$\chi^2 = \frac{[(t_i - t_0) - |\overrightarrow{r_i} - \overrightarrow{r_0}|/c]^2}{\sigma_i^2}, \tag{3.5}$$

where $t_i$ and $\overrightarrow{r_i}$ are the PMT hit time and PMT position in detector coordinates for PMT $i$, $t_0$ and $\overrightarrow{r_0}$ are guesses for the event time and position, and $\sigma_i$ is the estimated error on the value of the numerator in Equation 3.5. The reconstructed position for each event and the corrected PMT arrival time of the photons striking each PMT are histogrammed. The uncertainty in the three position coordinates and the time are calculated from these histograms. Figure 3.10 shows the PMT timing residual histogram (reconstructed time minus actual time) for data taken with the LB (solid histogram) and the SL source (dashed histogram). It is seen that the uncertainty in the timing for the SL calibration is less than that of the laserball. A Gaussian fit to both histograms yields: $\sigma_t = 1.6ns$ for the SL source and $\sigma_t = 2.0ns$ for the LB. Thus the PMT timing accuracy measurement of the SL source is better by approximately 25%. Furthermore, the spread measured by the SL source is approximately equal to the transit time spread of the PMTs, $1.6ns$, quoted by the manufacturer. Thus the SL source is essentially showing the response of the PMTs to delta function light signals. This is explained by the pulse width, which is more than one order of magnitude less than the PMT single photoelectron transit time spread.

Figure 3.11 shows the reconstructed position residuals (reconstructed position minus actual position) for both the LB (solid histogram) and SL (dashed histogram) sources. The SL source gives better accuracy. This is partly due to the better timing and partly due to the fact that the SL is essentially a point source. SL light comes from a bubble which is approximately $500nm$ in radius when the light is emitted. The LB has a diffuser ball with a radius of a few inches.

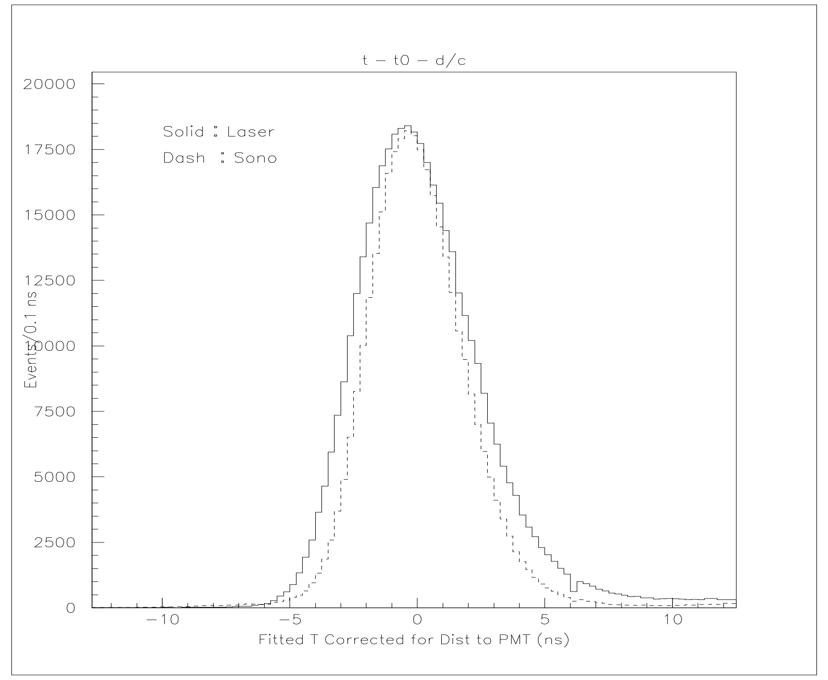


Figure 3.10: PMT time residuals for the LB (solid histogram) and SL source (dashed histogram). (The author thanks Bill Frati for the use of this plot.)

Table 3.1 summarizes the results of the timing and reconstruction residuals and compares the SL and LB sources in this regard.

**Intermediate Summary**

The SL sources and their operation have been described. Some initial data has been shown to explain some of the technical concepts specific to the SNO detector. Additionally, the PMT timing accuracy measurements performed with the air fill SL source were presented. It was shown that the SL source outperforms the laserball source by 25% in this measurement.

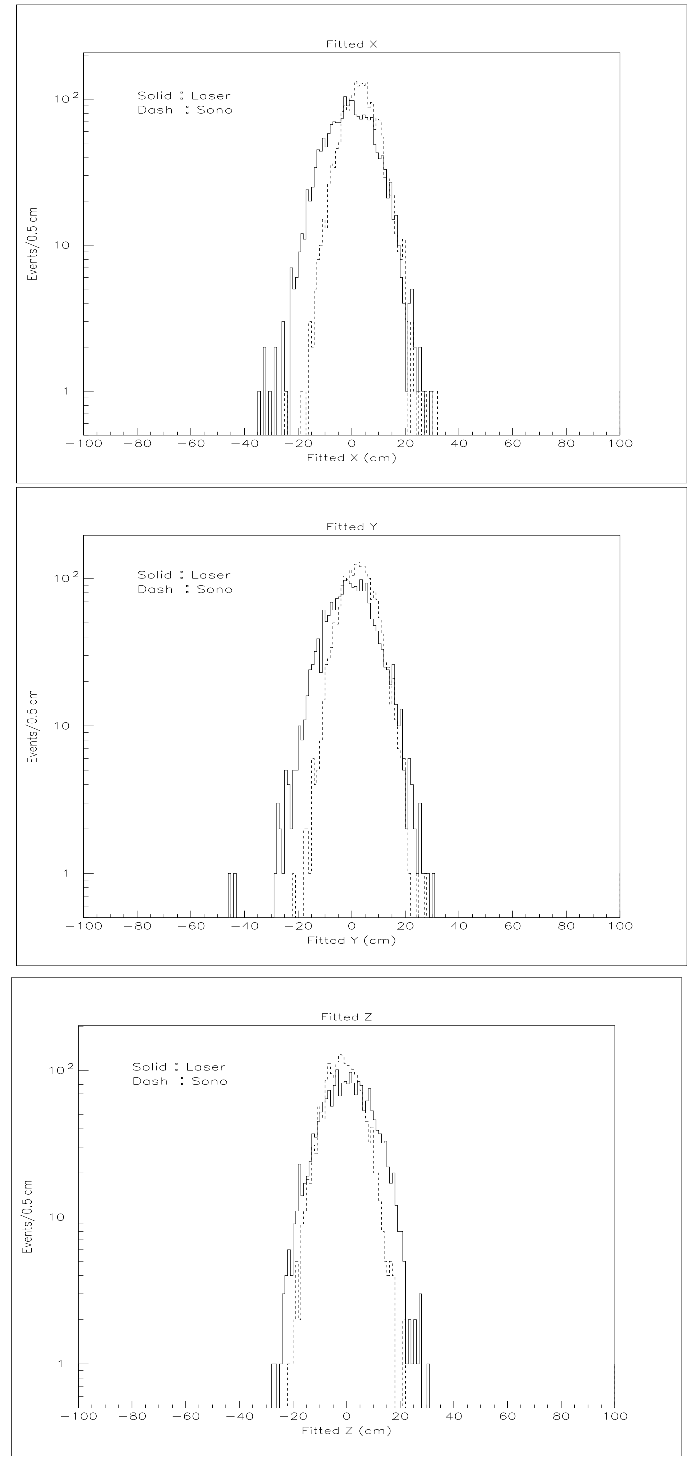


Figure 3.11: Reconstructed x, y and z position residuals for the LB (solid histogram) and SL source (dashed histogram). The results of the Gaussian fits to these histograms are shown in table 3.1. (The author thanks Bill Frati for the use of this information.)

| Run | Source | X(cm) | Y(cm) | Z(cm) | Time(ns) | $\chi^2/DOF$ |
|---|---|---|---|---|---|---|
| 101 | laserball | $-0.3 \pm 9.4$ | $-0.6 \pm 10.3$ | $0.3 \pm 10.0$ | $-0.2 \pm 2.0$ | 1.4 |
| 292 | SL source | $-3.3 \pm 9.9$ | $4.5 \pm 9.5$ | $-5.3 \pm 7.5$ | $0.0 \pm 1.6$ | 0.7 |

Table 3.1: Comparison of the timing calibration reconstruction performed with the laserball (LB) and SL sources. Reconstructed coordinates are measured in cm and the time in ns. The uncertainties are shown.(The author thanks Bill Frati for the use of this information.)

SL has also been used to unearth some systematic effects in the SNO electronics that may have gone unnoticed but for the analysis performed as part of this thesis. These analyses will be presented in Chapter 4. In order to understand that data and the other analyses presented, it is necessary to understand the photon correlation functions used. These will be described below.

### 3.5 Photon Correlation Functions

The possibility that pairs of photons might be correlated as a function of angle between the photon trajectories is intriguing and should give some insight into the physical mechanism of SL. Under certain conditions, previous experiments have seen angular correlations consistent with a small dipole component in addition to a spherically symmetric component [1].

Below is a discussion of the correlation functions used in the analyses described in Chapter 4. They can be categorized into two groups:

(1) "dynamic" correlation functions and

(2) "static" correlation functions.

The terms "dynamic" and "static" are due to the author. Dynamic correlation functions are capable of measuring correlations between photon pairs in which the features of the correlation move about the detector randomly. Static correlation functions are used to examine stationary features. Monte Carlo simulations of dipole radiation make the difference between these two types of correlation functions clear. They are presented after the discussion of the functions themselves.

The dynamic correlation functions remove some of the systematic effects due to the detector or idiosyncrasies of the optical source. In general, the angular distribution of light emanating from a source will have static and dynamic components. The static component may be due to limitations in the design and have nothing to do with the physical process of light emission. The dynamic component, at least in the cases presented in this thesis, are due to the physical processes under scrutiny.

### 3.5.1 Dynamic Correlation Functions

A standard correlation function has the form:

$$\Delta Q_{ij} \equiv \frac{\langle Q_i(t) Q_j(t) \rangle_t}{\langle Q_i \rangle_t \langle Q_j \rangle_t} = \frac{\overline{Q_i Q_j}}{\overline{Q_i}\,\overline{Q_j}}, \tag{3.6}$$

which is the correlation of the charges in PMT$_i$ and PMT$_j$ at time t. Here $\overline{Q_i}$ is the average charge in PMT$_i$ and Q$_i$ is the charge measured in PMT$_i$ in any given SL event. $\langle\rangle_t$ denotes averaging over time. This correlation function is *not* normalized, i.e. when $i = j$ (correlation at "zero lag") the correlation function does not tend to 100%. Instead, the function tends to 1 for *uncorrelated* charge as the average of the charges of two PMTs is equal to the product of the average charges in those PMTs assuming any coincidences between them are random. Correlations between the charges in the two PMTs will have values of $\Delta Q_{ij}$ greater than 1 and anti-correlations will have values of $\Delta Q_{ij}$ less than 1.

Charge is used because it is assumed that the charge in each PMT is proportional to the intensity, I, of the light striking the PMT photocathode. In other words it is assumed that:

$$\Delta Q_{ij} = \frac{\langle \eta I_i(t) \eta I_j(t) \rangle_t}{\eta \overline{I}_i \eta \overline{I}_j} = \frac{\langle I_i(t) I_j(t) \rangle_t}{\overline{I}_i \overline{I}_j} \equiv \Delta I_{ij}, \tag{3.7}$$

where $\eta$ is the PMT quantum efficiency which is assumed to be the same for each PMT (otherwise the average of $\eta$ over all PMTs is substituted).

In the quantum domain, in which light is thought of in terms of photons striking the PMT photocathode, the same equation holds but can be rewritten for clarity as:

$$\Delta Q_{ij} = \Delta I_{ij} = \frac{\langle N_i(t) N_j(t) \rangle_t}{\overline{N}_i \overline{N}_j} \equiv \Delta N_{ij}, \tag{3.8}$$

where N$_i$ is the number of photons striking the photocathode of PMT$_i$ at time t.

SNO's PMTs do not have good charge resolution so it is not possible to count the number of photoelectrons in each PMT pulse with good accuracy.

### "Same Event" (SE) Correlation Function

In practice the correlation function, Equation 3.6, is calculated by looping over the data once to get the average charge in each PMT, and then looping over the data again, this time calculating the product of the charges in the pairs of PMTs which both fired in a given event, divided by the average charge in each PMT, and averaging this over all events. This is carried out for all PMT pairs in the detector region of interest and the results are averaged over all pairs with care taken not to double count. The resulting function is a function of the angle, $\alpha$, between the given PMT pair. The correlation measured in this manner will be referred to in this thesis as the "same event" (SE) correlation function. Thus, the SE signal is calculated via the following formula:

$$SE(\alpha) = \frac{1}{2}\sum_{i=1}^{N_{PMT}}\sum_{j=1}^{N_{PMT}} \frac{\sum_{k=1}^{N_{tr}} Q_{i,k}Q_{j,k}/N_{tr}}{(\sum_{k=1}^{N_{tr}} Q_{i,k}/N_{tr})(\sum_{k=1}^{N_{tr}} Q_{j,k}/N_{tr})} \cdot \frac{1}{N_{PMTpairs}(\alpha)}. \qquad (3.9)$$

The factor of one half prevents double counting of PMT (or photon) pairs. In the particular case where $i = j$, the comparison is between $\mathrm{PMT}_i$ and *itself*. The angle $\alpha$ will be zero in this case which gives the correlation at "zero lag" referred to above.

The angle $\alpha$ is binned. Choosing an index $l$ to represent the angular bins, the calculation of $N_{PMTpairs}(\alpha)$ in Equation 3.9:

$$N_{PMTpairs}(\alpha) = N_{PMTpairs}(l) = \sum_{i=1}^{N_{PMT}} \sum_{j=i}^{N_{PMT}} P(l) \tag{3.10}$$

where:

$$P(l) = \begin{cases} 1, & \text{if the binned angle } \alpha \text{ between PMT}_i \text{ and PMT}_j \text{ lies in bin } l \\ 0, & \text{otherwise} \end{cases}, \tag{3.11}$$

and, again, the two sums are carried out this way to prevent double counting of PMT pairs.

It should be pointed out that the correlation function, Equation 3.9 is set up such that it eliminates many uncertainties due to PMT efficiency variations including quantum efficiency, acceptance as a function of angle, reflections and other PMT geometry effects. This assertion is explained by the normalization factor of the average charge per PMT in the denominator. If a PMT has a low efficiency, it will not have many coincidences with other PMTs but it will also have relatively small average charge and the two effects tend to cancel on average.

From discussions below, it will become clear that a “PMT hit” correlation function is more accurate for the analyses of this thesis than the “charge” correlation of Equation 3.9. The “PMT hit” correlation function can be calculated from Equation 3.9 by assuming all charges are unity. Thus the correlation is between hit PMTs regardless of charge. When operating in the single photoelectron regime, the “PMT hit” and “charge” correlation functions are approximately equivalent.

**"Different Event" (DE) Correlation Function**

One would think that photons from *different events* should be uncorrelated. A DE correlation function can be defined via the following equation:

$$DE_{FULL}(\alpha) = \frac{1}{2}\sum_{i=1}^{N_{PMT}}\sum_{j=1}^{N_{PMT}} \frac{\sum_{k=1}^{N_{tr}}\sum_{k'>k}^{N_{tr}} Q_{i,k}Q_{j,k'}/\binom{N_{tr}}{2}}{(\sum_{k=1}^{N_{tr}} Q_{i,k}/N_{tr})(\sum_{k=1}^{N_{tr}} Q_{j,k}/N_{tr})} \cdot \frac{1}{N_{PMTpairs}(\alpha)}, \quad (3.12)$$

where the sums ($k$ and $k'$) over events are such that double counting is prevented. The combinatorics is such that there are $\binom{N_{tr}}{2}$ possible event comparisons explaining that factor in the denominator. Here, coincidences are obtained between a given event $k$ and *all subsequent* events $k'$, hence the statistical accuracy is much better than the SE function.

In practice, the DE function calculation is computationally intensive due to the large numbers of PMTs ($N_{PMT}$) and events ($N_{tr}$) in the runs analyzed for this thesis. To reduce the computational time, the number of different events compared was reduced to a number on the order of ten leading to a DE function:

$$DE(\alpha) = \frac{1}{2}\sum_{i=1}^{N_{PMT}}\sum_{j=1}^{N_{PMT}} \frac{\sum_{k=1}^{N_{tr}}\sum_{k'>k}^{k+N_{compare}} Q_{i,k}Q_{j,k'}/N_{DE}}{(\sum_{k=1}^{N_{tr}} Q_{i,k}/N_{tr})(\sum_{k=1}^{N_{tr}} Q_{j,k}/N_{tr})} \cdot \frac{1}{N_{PMTpairs}(\alpha)}, \quad (3.13)$$

where the only difference between this equation and Equation 3.12 is the $k'$ sum is only done to $k + N_{compare}$ (as mentioned above, $N_{compare}$ is on the order of ten) and the event normalization has been changed from $\binom{N_{tr}}{2}$ to $N_{DE}$ which can be calculated as:

$$N_{DE} = N_{compare}(N_{tr} - N_{compare}) + \binom{N_{compare}}{2}. \quad (3.14)$$

Equation 3.14 reduces to $\binom{N_{tr}}{2}$ for $N_{compare} = N_{tr}$ consistent with Equation 3.12.

For $N_{tr} = 25,000$, a typical value, the number of different event comparisons for the full DE function (Equation 3.12) is:

$$\binom{N_{tr}}{2} \sim 6.3 \times 10^8, \tag{3.15}$$

which would take a computer months to calculate (it has to be carried out for each PMT pair so there is another large factor involved), whereas the number for the reduced DE (Equation 3.13) with $N_{compare} = 10$ is:

$$N_{DE} \sim 5 \times 10^5, \tag{3.16}$$

three orders of magnitude smaller which takes a few hours for a computer to calculate.

It is possible to define a third correlation function, the "adjacent event" (AE) function. This is a special case of the DE function in which only adjacent events are compared. The AE function has the same statistical level as the SE function because hits from one event are compared to those of a single other event. The formula for calculating the AE function is obtained from Equations 3.13 and 3.14 with $N_{compare} = 1$. These three correlation functions, SE (Equation 3.9) and DE (Equation 3.13) and AE are used in this thesis in the analyses of three very different phenomena.

### 3.5.2 Static Correlation Functions

As stated above, the dynamic SE correlation function will detect only correlations that move about the detector from event to event. It will not, for example, detect a dipole correlation if the dipole axis stays fixed (with respect to the detector coordinates) over time. To see this, consider Equation 3.9. It is normalized by the average charge in each *local* PMT. If a certain area of the detector has more light than the rest, there will be more coincidences in that area making the numerator of Equation 3.9 relatively large. But that effect will be cancelled by the normalization (*i.e.* the denominator of the same equation), as those PMTs will have higher average charge. A static dipole would be totally uncorrelated under this an analysis, *i.e.* the SE function would be flat as a function of angle.

To detect correlations that are static in direction over time, it is possible to define a "static" correlation function. The static correlation SE function is defined as:

$$SE_{static}(\alpha) = \sum_{i=1}^{N_{PMT}} \sum_{j=i}^{N_{PMT}} \frac{\sum_{k=1}^{N_{tr}} Q_{i,k} Q_{j,k}/N_{tr}}{\overline{Q_0}^2} \cdot \frac{1}{N_{PMTpairs}(\alpha)}, \tag{3.17}$$

where:

$$\overline{Q_0} = \sum_{i=1}^{N_{PMT}} \sum_{k=1}^{N_{tr}} Q_{i,k}/(N_{PMT} N_{tr}) = constant, \tag{3.18}$$

is the *global* average charge of all PMTs over all events and is constant.

It can now be seen how this function detects "hot spots" at some part of the detector. If there is such a hot spot, with higher than normal rates, there will be more coincidences in this area. However, the normalization will be the same for all areas of the detector, and the denominator will not cancel the effect. This spot will have a higher correlation than other spots which will yield a correlation at small angles.

The corresponding DE function is:

$$DE_{static}(\alpha) = \sum_{i=1}^{N_{PMT}} \sum_{j=1}^{N_{PMT}} \frac{\sum_{k=1}^{N_{tr}} \sum_{k'>k}^{k+N_{compare}} Q_{i,k} Q_{j,k'} / N_{DE}}{\overline{Q_0}^2} \cdot \frac{1}{N_{PMTpairs}(\alpha)}. \quad (3.19)$$

however, there is no need to use the DE static correlation function as it gives the same result as the SE static correlation function. The whole point of the static functions is to detect correlations that do not change direction over time. In such cases, photons from different events should have the same correlation as photons in the same event.

The SE static correlation function is also used in the analyses discussed in this thesis.

### 3.5.3 Monte Carlo Comparison of Static and Dynamic Correlation Functions

To show the difference between the dynamic and static correlation functions, MC simulations of SL in the SNO detector were carried out with a 23.1% *stationary* dipole angular distribution, where the dipole axis coincided with the detector vertical axis. Figure 3.12 shows a plot of each of the correlation functions described above applied to this MC data set. It is seen that the dynamic correlation function does not

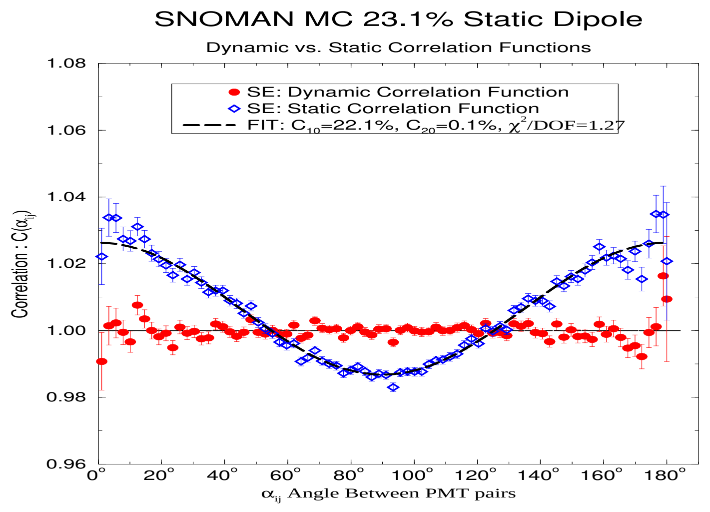


Figure 3.12: SNOMAN SL Monte Carlo simulation of a 23.1% stationary dipole. Shown are the "dynamic" and "stationary" same event (SE) correlation analyses. It is seen that the dynamic analysis shows no correlation.

show any correlation while the static one does. The amplitude of the static correlation is not 23.1% because the nature of the correlation function is such that it averages over all directions (the sum over all PMT pairs), not just with respect to the detector zenith. A fit is shown which shows a fit value of $22.1 \pm 0.5\%$ for the dipole and the $\chi^2/DOF$ is good at 1.27.

Figure 3.13 shows a Monte Carlo simulation of a 10% *dynamic* dipole. The dipole direction moves about the detector randomly from event to event. The SE static and dynamic analyses are shown. It is seen that both detect the dipole and give similar results. The reason the static correlation function detects the dynamic dipole is due to the properties of the correlation functions and the way they are applied to the SNO

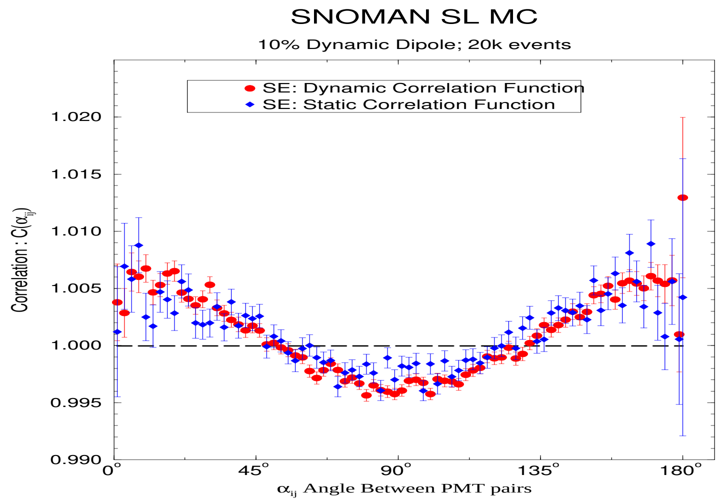


Figure 3.13: SNOMAN SL Monte Carlo simulation of a 10% dynamic dipole. Shown are the "dynamic" and "stationary" same event (SE) correlation analyses. Both correlation functions detect the dipole.

detector. Both the static and dynamic correlation functions are summed over all PMT pairs. This is equivalent to integrating over the full solid angle in detector coordinates. The movement of the dipole direction randomly over all directions is also equivalent to integrating over the solid angle because the correlation functions are averaged over all events in the run. It is this integration which causes the amplitude of the dipole to appear as a few percent rather than at its full strength of 23.1% in Figure 3.12 and 10% in Figure 3.13.

### 3.5.4 Laserball and Sonoluminescence Static Correlation Functions

Figure 3.14 shows the static SE correlation functions for the LB and SL sources. Bright spots in the intensity appear as correlations larger than one at small angles. Both the LB and SL sources show such bright spots. Relatively dim spots appear as anticorrelations with function values less than one. Detector effects could account for some of the correlation or anticorrelation. However, the limit on the detector contribution is set by the SL SE plot since its features are smaller. This shows that most of the features in the LB static correlation function are due to the LB source itself. Photons in the LB diffuser ball scatter between 4 and 16 times before exiting [74]. The LB system uses a fiber optic cable to transmit the laser light from the laser on the deck to the diffuser ball. If the fiber optic cable does not terminate in the exact center of the diffuser ball, the intensity of the light will be higher from the area where the cable is closest to the diffuser ball wall.

### 3.5.5 Time Autocorrelation Functions

The same event (SE) and adjacent events (AE) correlation functions are related to the concept of time autocorrelation functions. A time autocorrelation function is used to find correlations in a data set over time. The calculation of a time autocorrelation function is performed according to the following formula:

$$TC(\Delta t_{k,k'}) = \frac{1}{2}\sum_{i=1}^{N_{PMT}}\sum_{j=1}^{N_{PMT}} \frac{\sum_{k=1}^{N_{tr}}\sum_{k'>k}^{N_{tr}} Q_{i,k}Q_{j,k'}/\binom{N_{tr}}{2}}{(\sum_{k=1}^{N_{tr}} Q_{i,k}/N_{tr})(\sum_{k=1}^{N_{tr}} Q_{j,k}/N_{tr})} \cdot \frac{1}{N_{PMTpairs}}, \qquad (3.20)$$

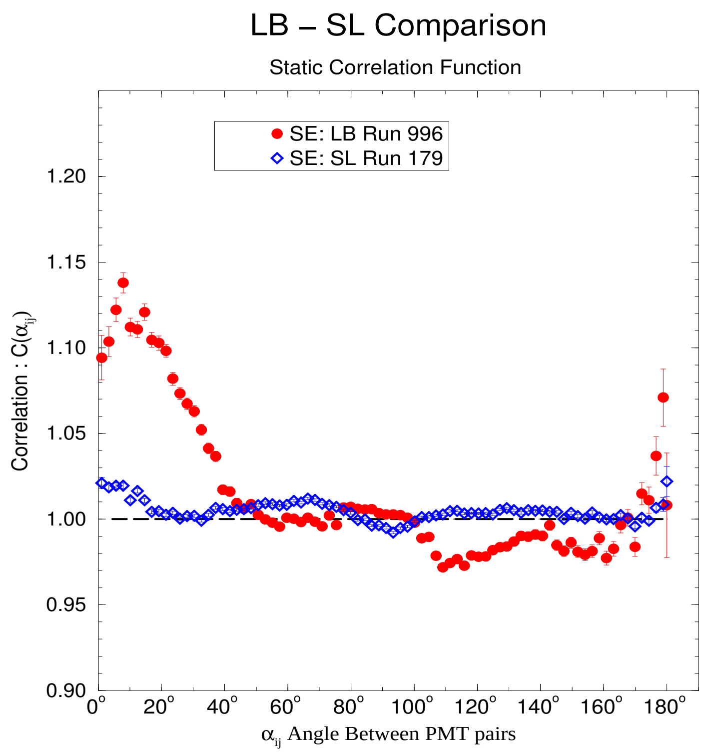


Figure 3.14: LB run 996 and SL run 179 "static" same event correlation functions. The LB static angular distribution is far less isotropic than that of the SL source.

which is similar to the full DE correlation function of Equation 3.12 but in this case it is a function of the time difference between events, $\Delta t_{k,k'}$. For $k = k'$, the time autocorrelation function is equivalent to the average over all angles of the SE function of Equation 3.9. The full DE function is the average of the time autocorrelation function for each angular bin over all event times.

Time autocorrelation functions can be used to study fluctuations in light intensity over time. For the simple case of sine wave intensity fluctuation modeled as:

$$I(t) = I_0(1 + \epsilon \cos \omega t), \tag{3.21}$$

the same event (SE) dynamic correlation function can be shown to yield:

$$SE(periodic\ intensity\ fluctuations) = 1 + \frac{\epsilon^2}{2}, \tag{3.22}$$

as is shown below.

The average charge observed by a PMT under this model is:

$$\overline{Q}_i = \langle Q_0(1 + \epsilon \cos \omega t)\rangle_t = Q_0. \tag{3.23}$$

That is, the average charge is a constant determined by the intensity level. However the same event correlation between the charges in two given PMTs is:

$$\langle Q_{i,k}Q_{j,k}\rangle = \langle Q_0^2(1 + 2\epsilon \cos \omega t + \epsilon^2 \cos^2 \omega t)\rangle_t = Q_0^2(1 + \frac{\epsilon^2}{2}), \tag{3.24}$$

which is constant. The same event correlation function is essentially the ratio of the above expression and the square of the average charge:

$$SE(periodic\ intensity\ fluctuations) = \frac{Q_0^2(1 + \frac{\epsilon^2}{2})}{Q_0^2} = 1 + \frac{\epsilon^2}{2}, \tag{3.25}$$

which is equivalent to the expression in Equation 3.22. Thus periodic intensity fluctuations result in a positive correlation offset of the same event correlation function. This behavior is seen to some degree in all of the correlation analyses performed for this thesis.

The different events correlation function for the periodic fluctuation model above has no positive correlation offset. The different events correlation of PMT charges can be shown to be:

$$\langle Q_{i,k} Q_{j,k'} \rangle = \langle Q_0^2 (1 + \epsilon \cos \omega t_k + \epsilon \cos \omega t_{k'} + \epsilon^2 \cos \omega t_k \cos \omega t_{k'}) \rangle_{t_k t_{k'}} = Q_0^2, \quad (3.26)$$

which cancels with the denominator yielding a DE correlation function of unity over all angles. The last equality is true only if the number of different events comparisons is large enough to average over at least one period of the fluctuation cycle.

### 3.5.6 Electronics Channel Correlation Functions

It is possible to define SE and DE, static and dynamic correlation functions which are functions of difference in electronics channel number. There is a one to one mapping of PMT to channel number. The functions are calculated the same way as the PMT angle correlation functions discussed above, with the exception that PMT hits are mapped to the unique channel number. Then the difference between the channel numbers of two coincident PMT hits is used as the abscissa when plotting the correlation function. The functions can be used to study correlations between

PMT hits on neighboring channels. Neighboring channels are often connected to neighboring PMTs but not always. For isotropic light, PMT hits on neighboring channels should be uncorrelated. Any departure from uncorrelated behavior can be separated from real correlations because nearby channels are not always nearby PMTs. Comparing the angular and electronics channel correlation functions may show whether the effect is real or a systematic effect of the electronics.

These electronics channel correlation functions are used to analyze systematic effects in the LB and SL data. The data will be presented in Chapter 4.

### 3.6 Applying Photon Correlations to Fundamental SL Investigations

As mentioned above, experiments measuring some fundamental properties of SL have been performed using the SNO detector. The SNO detector provides a unique opportunity to perform such measurements due to its:

(1) large number (9522) of PMTs, allowing many data points in a single SL pulse (event),

(2) large and stable spherical geometry, ideal for angular distribution and the other measurements performed,

(3) state of the art electronics and

(4) data acquisition and archiving facilities.

The topics investigated were: back-to-back photon correlations, the angular distribution of SL photons, and measurement of the size of the light emitting region of a SL bubble. These topics will be introduced individually below. It will be shown how the correlation functions described in the previous section are used in the analyses. The data are presented in Chapter 4.

### 3.6.1 Back-to-Back Photon Correlations

The QED theories of SL light emission have been discussed in Chapter 1. In these theories, each photon has a correlated partner and the photons are emitted virtually back-to-back with nearly the same energy. The geometry of the SNO detector is excellent for this as approximately 3700 of its PMTs have a "partner" PMT at nearly 180° from it across the detector. Thus for each SL event many sets of back-to-back photon pairs can be counted if the effect is present. The sensitivity will be quantified when the analysis is presented in Chapter 4, Section 4.3.

The dynamic correlation functions described above are ideal for analysis of back-to-back photons. Calculation of the SE dynamic correlation function should show a positive correlation at an opening angle of 180° . There should be no correlations at other angles. For this analysis, however, a slightly modified version of the dynamic SE function is used. Unity is subtracted from the SE function and it is normalized by the correlation at zero lag. This does not change the behavior of the SE function.

The function, in this form, becomes a true correlation function which is limited to the interval [-1,1] with uncorrelated light giving a value of zero and anticorrelations giving negative values. This is carried out to show the strength of the correlation clearly. If 100% of the photons have correlated, back-to-back partners, then the SE function should be flat for all other angles and should approach the value of unity at 180° assuming perfect detection efficiency. This will become clear when Monte Carlo simulations of the effect are shown in Chapter 4, Section 4.3.

### 3.6.2 Angular Distribution of Photons

The angular distribution of photons for SL has been measured by Hiller *et. al.* to be nearly spherically symmetric [1]. These researchers have measured a small dipole moment and have attributed it to a dipole moment in the shape of the bubble. If there is some further deviation from spherical symmetry, SNO is ideally suited to measure it as the detector has a large number of PMTs on an approximately spherically symmetric array. This measurement has been carried out as part of this thesis.

Correlation functions can be used to measure the multipole moments of an arbitrary angular distribution function although the method gets tedious when a large number of multipoles are included. Such an analysis has been carried out using data taken with a SL source in the SNO detector. This section will discuss how the correlation function is used in the analysis. The theoretical discussion below is based largely on the work of Hiller *et. al.* [1].

If the angular distribution is mostly monopole with a small dipole component, the number of photons striking PMT$_i$ at angles $\theta_{det,i}$ and $\phi_{det,i}$ will be:

$$N_i(t) = N_I + 3N_D \cos \alpha_{i,k}(t), \tag{3.27}$$

where $\alpha_{i,k}$(t) is the angle between the dipole axis and PMT$_i$ at time t, and N$_I$ and N$_D$ are the isotropic and dipole strengths respectively. If one assumes the dipole has no preferred direction over time, the dynamic same event (SE) correlation function can be expressed as:

$$SE(\alpha_{ij}) = \frac{f_D^2}{(1+f_D)^2}(\frac{1}{5} + \frac{3}{5}\cos 2\alpha_{ij}), \tag{3.28}$$

where $f_D = N_D/N_I$ is the fractional dipole strength.

The same analysis can be carried out assuming any order of multipole moments although the calculations can be cumbersome. The calculation for the more general case of a dipole of strength $f_D$ and a quadrupole of strength $f_Q$, summed coherently, is given in Equation 3.29. This calculation assumes that the dipole and quadrupole have the same axis (as in the dipole calculation, the direction of this axis is randomly distributed over time):

$$\Delta Q_{ij} = \frac{112 f_D^2 + 160 f_D f_Q + 115 f_Q^2}{560(1+f_D+f_Q)^2}$$

$$+\frac{(2440 f_D f_Q)\cos(\alpha)}{560(1+f_D+f_Q)^2}$$

$$+\frac{(336 f_D^2+480 f_D f_Q+300 f_Q^2)\cos(2\alpha)}{560(1+f_D+f_Q)^2}$$

$$+\frac{(1080 f_D f_Q)\cos(3\alpha)}{560(1+f_D+f_Q)^2}$$

$$+\frac{225 f_Q^2\cos(4\alpha)}{560(1+f_D+f_Q)^2}. \tag{3.29}$$

### 3.6.3 Intensity Interferometry: Measuring the Spot Size of SL

Hanbury-Brown and Twiss (HBT) developed the technique of "intensity interferometry" in the 1950's in attempts to better measure the diameters of distant stars [71, 72]. Previously, astronomers used a technique developed by Michelson and based on his famous interferometer, to perform such measurements [75]. It was only possible to measure the diameters of large, red giant, stars with Michelson's technique due to limitations in mechanical design. With intensity interferometry, however, it was possible to measure the diameters of smaller, main sequence, stars which are more plentiful and the method extended the catalog of stars whose diameters had been measured from 6 to 32 over a period of a few years [72]. Furthermore, HBT were able to measure the diameters of main sequence stars for the first time.

A brief comparison of Michelson and intensity interferometry follows and is based on discussions in Hanbury-Brown's book [72]. For more complete information see it and other references [71, 76].

### Michelson Interferometry

Michelson interferometry is the standard method of interferometry. Two primary mirrors, separated by a distance $d$, detect light from the same source (star). The mirrors are equidistant from the star and the separation is much smaller than the diameter of the star. The diameter of the star is, in turn, much smaller than the detector-star distance. Thus the following conditions are essential:

$$d << R_{star} << D, \tag{3.30}$$

where $D$ is the detector-source distance. The signals from the primary mirrors are combined on a secondary mirror and focused on a screen or photodetector. The intensity at the detection point is essentially a correlation of the electromagnetic field vectors of the light from the two primary mirrors. The distance between the primary mirrors can be varied by the experimenter while maintaining precise control of the relative path difference of signals from the two primary mirrors to the detection point. The intensity of the light at the detection point depends on this separation, $d$, according to the equation [72]:

$$\Delta I = \frac{I_{max} - I_{min}}{I_{max} + I_{min}} \propto \frac{\sin(\pi d\theta/\lambda)}{\pi d\theta/\lambda}, \tag{3.31}$$

where, $\lambda$ is the wavelength of the light, and:

$$\theta = \tan\left(\frac{2R_{star}}{D}\right) \sim \frac{2R_{star}}{D}, \tag{3.32}$$

is the angular size of the star. In the last equation, $D$ is the distance from the observer to the star, $R_{star}$ is the radius of the star and the last expression is an approximation that holds for all stars as they are so far away (*i.e.* $D >> R_{star}$). The function $\Delta I$, in Equation 3.31, peaks at $d = 0$ and goes to zero at the critical detector separation:

$$d_{critical} = 1.22\frac{\lambda}{\theta}, \tag{3.33}$$

although it has other zeroes as well. A measurement of this critical separation for a given star is a measure of its angular diameter, and therefore the actual diameter provided the distance to the star is known. Monochromatic light is required in this method and if the source is not monochromatic, filters are used at the detector.

The limitations of this technique are due to the fact that it relies on phase cancelations between the two primary mirror signals. The path length difference from each primary mirror to the secondary (which are, in practice on the order of tens of meters) have to be controlled to be of the order of the wavelength of the light. Secondly, the path difference has to be less than the coherence length of the light. These mechanical design requirements are very difficult to obtain with such large apparatuses. Finally, path length differences between the star and each primary mirror occur due to atmospheric effects. Such a problem can only be overcome by a putting an interferometer in space.

**Intensity Interferometry**

The HBT method relies on correlations in the *intensity* of light between two detectors far distant from a source. While Michelson interferometry is essentially the correlation of the electromagnetic fields of two different signals from the same source, "intensity interferometry" (II) correlates the intensity, or square, of the electromagnetic field. For that reason, the correlation function used is often referred to as a "second order" correlation function in the literature [72, 76].

There are two methods of doing intensity interferometry: correlations in the fluctuations of the currents from two photodetectors, and correlations in the number of photons counted by two photodetectors. The first method is based on classical physics and the second on the quantum nature of the photon fluctuations. Although HBT used the first method in their apparatus for measurement of the angular diameter of stars, they proved that the (more controversial) quantum method worked by doing experiments with a Mercury vapor lamp [77]. Since the quantum method was used for this thesis, only that will be described. For a good explanation of both methods see Hanbury-Brown's book [72].

The quantum treatment of intensity interferometry is based on the fact that photons are bosons and obey Bose-Einstein statistics. The variance of a Bose-Einstein distribution is larger than that of a Poisson or Gaussian distribution. With perfect resolving power, a PMT detecting steady beam of light will have fluctuations which are much larger than the square root of the mean. Non-zero timing resolution can prevent detection of this phenomenon depending on how poor the resolution is.

Consider two PMTs detecting light from the same source. Naively one expects the coincidences between them to be random. With good enough timing resolution, however, one would notice that the intensity fluctuations of the light measured by the two PMTs is slightly correlated. Thus:

$$\frac{\langle N_i N_j \rangle}{\langle N_i \rangle \langle N_j \rangle} \sim \frac{\langle Q_i Q_j \rangle}{\langle Q_i \rangle \langle Q_j \rangle} > 1, \tag{3.34}$$

whereas for random correlations, the ratio would be unity. Here, $N_i$ is the number of photons counted by $PMT_i$ and $Q_i$ is the charge detected by the same PMT. The angular brackets denote averaging over some number of events. As stated above, this effect is due to the Bose-Einstein nature of the photons. It is this property which is being tested in the intensity interferometry experiments carried out in this thesis.

Note that Equation 3.34 looks similar to the correlation functions described in Section 3.5 without all of the summations and indices. Thus the correlation functions are well suited for measurements of intensity interferometry.

As stated above, the correlation vs. angle between detectors for Michelson interferometry varies as:

$$\frac{\sin(\pi d\theta/\lambda)}{\pi d\theta/\lambda}. \tag{3.35}$$

For intensity interferometry, it can be shown that the dynamic SE correlation function will have an angular dependence which varies as unity plus the square of this function:

$$SE(\alpha) \sim 1 + \left(\frac{\sin(\pi d\theta/\lambda)}{\pi d\theta/\lambda}\right)^2, \tag{3.36}$$

which peaks at $\alpha = 0$ and goes to unity at the same critical value presented in the Michelson interferometry case:

$$d_{critical} = 1.22\frac{\lambda}{\theta}. \tag{3.37}$$

Slotta and Heinz [2] use a different but equivalent parametrization in their model of SL intensity interferometry. They also discuss the effect of non-zero bandwidth of the filters used to limit the wavelength of the light and the effect of the finite SL pulse width. Slotta and Heinz show that the width of the correlation is related to the spot size of the SL bubble as:

$$SE(\alpha) = 1 + \frac{C(\alpha = 0, \delta\omega, \delta\tau)}{2} exp(-4R_{SL}^2 k^2 \tan^2(\alpha/2)), \tag{3.38}$$

where $R_{SL}$ is the SL spot size, $k = 2\pi/\lambda$ is the wavenumber of the light coming through a filter of bandwidth $\delta\omega$, and:

$$C(\alpha = 0, \delta\omega, \delta\tau) = \frac{1}{\sqrt{1 + 4\delta\omega^2\delta\tau^2}}, \tag{3.39}$$

where $\delta\omega$ is the optical filter bandwidth in units of radial frequency, and $\delta\tau$ is the SL pulse width. $C(\alpha = 0, \delta\omega, \delta\tau)$ represents the correlation at zero opening angle and is dependent as shown on the bandwidth of the optical filter used and the SL pulse width. For extremely small pulse widths ($\tau_{SL} << 1ps$), or bandwidths ($\delta\lambda << 1nm$), the value of the constant $C(\alpha = 0, \delta\omega, \delta\tau)$ tends to 1/2. The pulse width of SL has been measured to be between 30 and 300 ps. For the intensity interferometry experiments performed in this thesis, the optical band pass filters used had bandwidths of $1nm$ and $10nm$. For the $10nm$ bandwidth filter and $\tau_{SL} = 300ps$, the worst case value of the correlation at zero opening angle is:

$$C(\alpha = 0, \delta\lambda = 10nm, \tau_{SL} = 300ps) = 7.8 \times 10^{-6}. \quad (3.40)$$

which shows the difficulty of the measurement undertaken. For the $1nm$ bandpass filter and a SL pulse width of $30ps$ gives a best case scenerio that is approximately two orders of magnitude larger or:

$$C(\alpha = 0, \delta\lambda = 10nm, \tau_{SL} = 300ps) = 7.8 \times 10^{-4}. \quad (3.41)$$

This model is used to fit the data for the intensity interferometry experiment performed for this thesis and will be discussed when that analysis is presented in Chapter 4.

For SL, it is desired to find the spot size - the size of the light emitting region of the bubble. The quantum vacuum radiation theories predict light is emitted from the bubble surface. The adiabatic heating theory assumes emission throughout the entire bubble volume while the shock wave theory predicts the light comes from a volume much smaller than the bubble size. Consideration of the geometry of SNO and the wavelengths of interest gives the sensitivity of SNO to measure the effect.

The minimum angle SNO can probe is approximately 2° , the angular separation of adjacent PMTs. With $\lambda = 400$ nm, SNO is sensitive to spot sizes between 40 and 1000 nm. There is evidence that the *bubble* size is approximately the wavelength of red light ($\lambda \sim 500$ nm) when SL light is emitted [49, 50]. Therefore SNO is sensitive in just the right range to measure this important parameter of SL.

### 3.7 Summary

It has been shown that the SL source is a useful calibration device for PMT timing and single photoelectron calibrations, supernova simulation, and detecting detector pathologies. In the future it may be possible to do some quick, stability checks of the optical properties of the detector using the SL source as well, although this has not been done yet.

Some SL data was introduced to enable the reader to understand some of the issues related to the SNO detector. Measurements of PMT timing accuracy were presented for the SL source and the laserball (LB) and it was shown that the SL source outperformed the LB by 25% for that calibration.

Correlation functions used in all analyses presented in Chapter 4 were discussed in detail. Finally, it was shown how these correlation functions will be used to do each experimental analysis. The results of these experiments will be presented in the following chapter.

# Chapter 4

# Angular Distribution and Angular Correlations

## 4.1 Introduction

The previous chapter discussed some experimental issues concerning sonoluminescence (SL) and its use in the SNO detector. Some SL data taken with the SNO detector were shown and most of the cuts that are made on the data were explained. It was shown how SL was used to measure the PMT timing and event position reconstruction residuals and that it outperformed the laserball (LB) by 25% in the timing residual measurement. Various correlation functions were discussed. Finally, the application of these correlation functions to the experimental analyses of this thesis was explained.

This chapter presents the three main analyses performed for this thesis:

(1) back-to-back photon correlations in SL light,

(2) the angular distribution of SL photons, and

(3) a measurement of the SL spot size using intensity interferometry.

Section 4.2 describes two systematic effects that were uncovered during the process of analyzing the data for this thesis. The time autocorrelation of the LB data is also shown and the degree of intensity fluctuations is measured. The three main analyses of this thesis are presented individually. Section 4.3 describes the back-to-back photon correlation analysis performed. Section 4.4 discusses the measurement of the photon angular distribution of SL light. Section 4.5 describes the attempt to measure the SL spot size using intensity interferometry. Finally, Section 4.6 provides a summary and discussion of the results.

### 4.2 Systematic Studies Using the Laserball

The laserball (LB) data is used as a control sample for the SL data presented in this thesis. The LB is known not to exhibit back-to-back photon correlations. The angular distribution of the LB is approximately isotropic (in a dynamic sense) and is measured here. Lasers, except under special circumstances, do not exhibit correlated intensity fluctuations as the light is coherent [72, 76]. However, the diffuser ball of the LB system scatters the photons entering it between 4 and 16 times before they escape [74]. This randomizes the photons enough that intensity interferometry is possible. However, the spot size of the emission region of the light from the LB diffuser ball is too large ($R_{LB} \sim 5$ cm) to be measured with the SNO detector using intensity interferometry. Spot sizes larger than approxmately 3$\mu$m are undetectable. Thus the LB is a good control light source that can be used to study systematic effects.

During the course of studying angular correlations in the laser (LB) and sonoluminescence (SL) data, two systematic effects became evident. Study of these systematics led to proof that they are due to subtle effects in the SNO electronics. These effects may not have been detected or understood if not for the analyses undertaken as part of this thesis. Both the LB and SL data (as well as all other SNO data when analyzed with correlation functions) show the effects although they will be presented in the context of the LB data. The first effect is crosstalk between adjacent electronics channels. The second effect is a slight charge anticorrelation happening only when PMT pulses occur on the same SNOD discriminator chip or, to a lesser degree, on adjacent SNOD chips on the same daughter card.

Figure 4.1 shows the "PMT hit" and "charge" same event (SE) correlation functions for LB run 996. The primary feature of the distribution is that it has a positive correlation offset of approximately 0.4%. This effect is due to slight intensity fluctuations over time. A time correlation analysis, discussed in Section 4.2.4 below, provides a measurement of the average strength of the fluctuations. Other features of the correlation plots shown in Figure 4.1 are that neither SE function is flat at the smallest angles. The PMT hit SE function has a positive correlation and the charge SE function has an anticorrelation at these angles. This information reveals both systematic

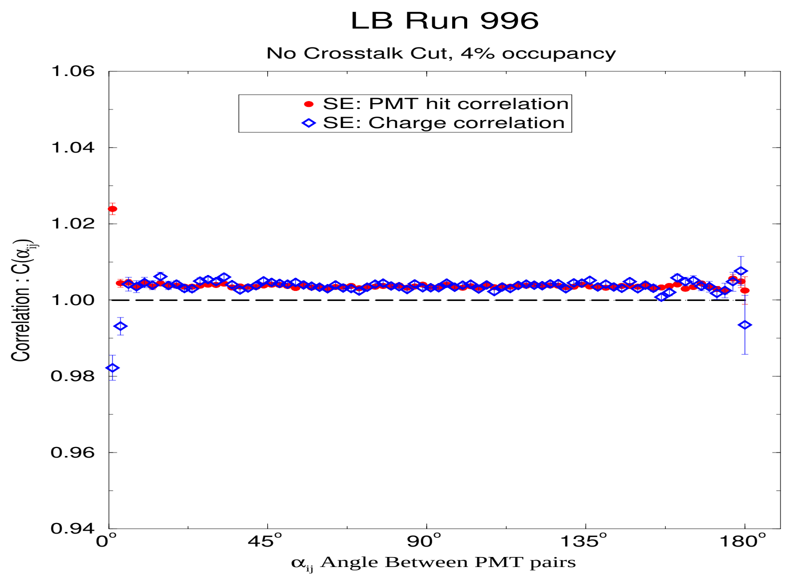


Figure 4.1: Laserball Run 996: "PMT hit" and "charge" same event correlation functions. Note the slight positive correlation for the PMT hit SE function and the anticorrelation of the charge SE function at small angles. Also note the 0.4% positive correlation offset at all angles.

effects mentioned above although it is not obvious at this stage. First, the discussion will concentrate on the positive correlation of the PMT hit SE function which is due to electronic crosstalk. The charge anticorrelation effect will be presented later.

### 4.2.1 Electronic Cross Talk

A large charge in one electronics channel will be picked up by the neighboring channel via the small capacitance between the channels. The measured integrated charge on the adjacent channel will be far smaller than that on the channel with the real charge because the signal from capacitive pickup is essentially the derivative of the pulse being picked up. The pickup, therefore, has a positive and negative swing with amplitudes that are approximately equal within the integration time. Crosstalk, thus, has a unique signature. The channel (PMT) with the real charge will have large integrated charge or it will not cause appreciable crosstalk. The adjacent electronics channel(s) will have very little integrated charge. Such a signature provides a means of cutting out much of the crosstalk background as will be described below.

The positive correlation at small angles of the PMT hit SE function in Figure 4.1 is due to electronic crosstalk between adjacent electronics channels. To show this, the charge behavior of all pairs of PMT hits in adjacent electronics channels has been compared to that of PMT hits in adjacent PMTs which are not in adjacent electronics channels. Figure 4.2 shows this comparison. Both scatter plots in the figure plot the larger (smaller) of the pair of charges for a given coincidence on the x axis (y-axis). The top plot is for all adjacent electronics channels and the bottom plot is for adjacent PMTs which are not in adjacent electronics channels. It is seen that the plots are similar except for the region of small charge in the y-direction. This area has entries only for adjacent channels. It is the region with large charge in one channel and very small charge in the adjacent channel. Since adjacent PMTs which are not adjacent channels do not show the effect, it cannot be due to real light.

A simple cut has been developed to minimize the effect of this crosstalk. The region which shows the crosstalk is fairly well separated from the signal region. There is a "valley" region in between the two which is not visible in the coarse plot in Figure 4.2. A closeup of the adjacent channels plot is shown in Figure 4.3 with a line drawn through the valley. If an entry falls below this line and to the right of it, the smaller of the charges is eliminated from further analysis as it is due to crosstalk. The larger charge is not eliminated as it is due to real light.

The crosstalk "background" region has a slight overlap with the signal region. It is important to show how much signal is lost by this cut. An estimate of the cut signal can be obtained by comparing how much data is cut when applying the crosstalk cut to next-to-adjacent channels (*i.e.* channels whose channel numbers differ by two). Figure 4.4 shows the same plot for adjacent channels before (top) and after (bottom) the crosstalk cut has been applied. The same is shown in Figure 4.5 for next-to-

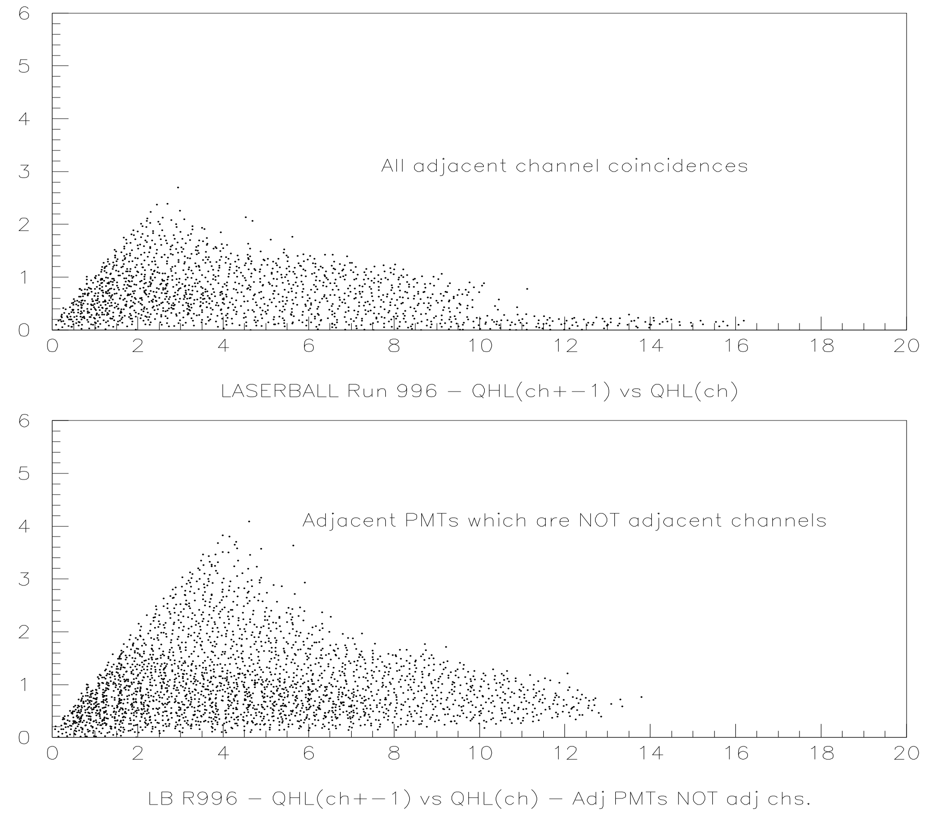


Figure 4.2: Laserball run 996: $QHL_{min}$ vs. $QHL_{max}$ for all photon coincidences in: adjacent electronics channels (top plot), and adjacent PMTs which are not in adjacent electronics channels (bottom plot). The cross talk region at low charge is populated in the top plot, but not in the bottom plot.

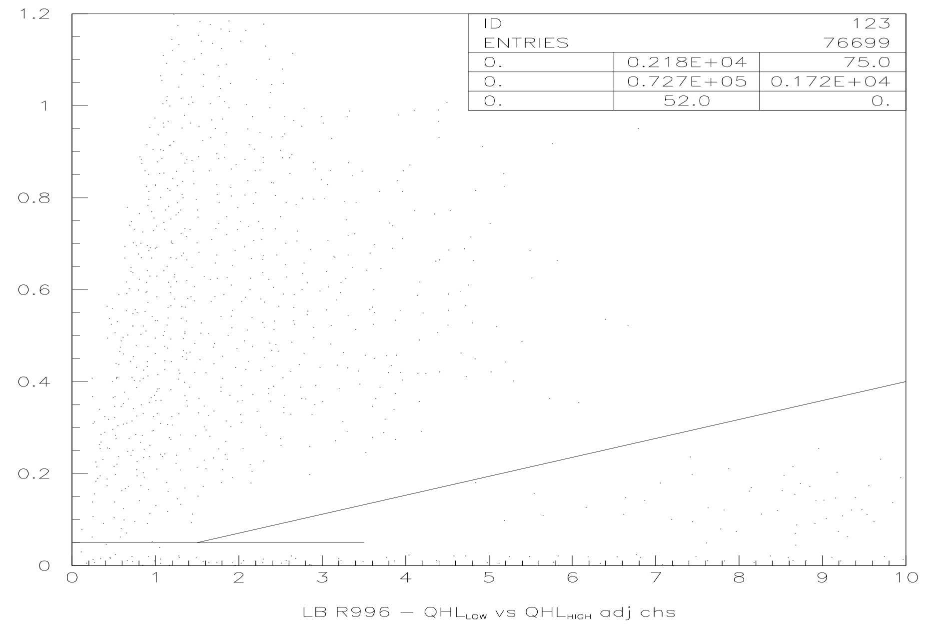


Figure 4.3: Laserball run 996: A closeup of the top plot in Figure 4.2 showing the separation of the crosstalk background from the signal. The crosstalk cut line is shown. The smaller of the two charges from entries below and to the right of the cut line are discarded.

adjacent channels. The number of entries in all of the scatter plots are shown and can be used to calculate the fraction of cut PMT hits in each case. For adjacent channels, 2.8% of the hits will be cut. For next-to-adjacent channels, 0.4% will be cut. The estimated upper limit on signal loss is then 0.4%.

This crosstalk effect will have to be considered in SNO neutrino analyses as it may bias the fits to Cerenkov events. The effect on Cerenkov events is small, however, because it only happens when large charges ($Q > 5PE$) occur in a PMT. This does not happen often for low energy Cerenkov events.

A plot of the SE correlation function after the crosstalk cut is made is discussed after the second electronics systematic is discussed.

### 4.2.2 Daughter Card Charge Anticorrelation

The "charge" SE correlation function in Figure 4.1 shows an anticorrelation at small angles, with a 2% effect for the first data point. This anticorrelation is due to an electronics effect that happens very rarely. Figure 4.6 shows a plot of the SE electronics channel correlation function discussed in Chapter 3, Section 3.5. This function is used to show correlations as a function of the difference in electronics channel number rather than angle between PMTs. It is used to separate systematic effects from physics. Figure 4.6 shows the *charge* SE correlation functions for:

(1) coincidences on the same SNOD chip (diamonds),

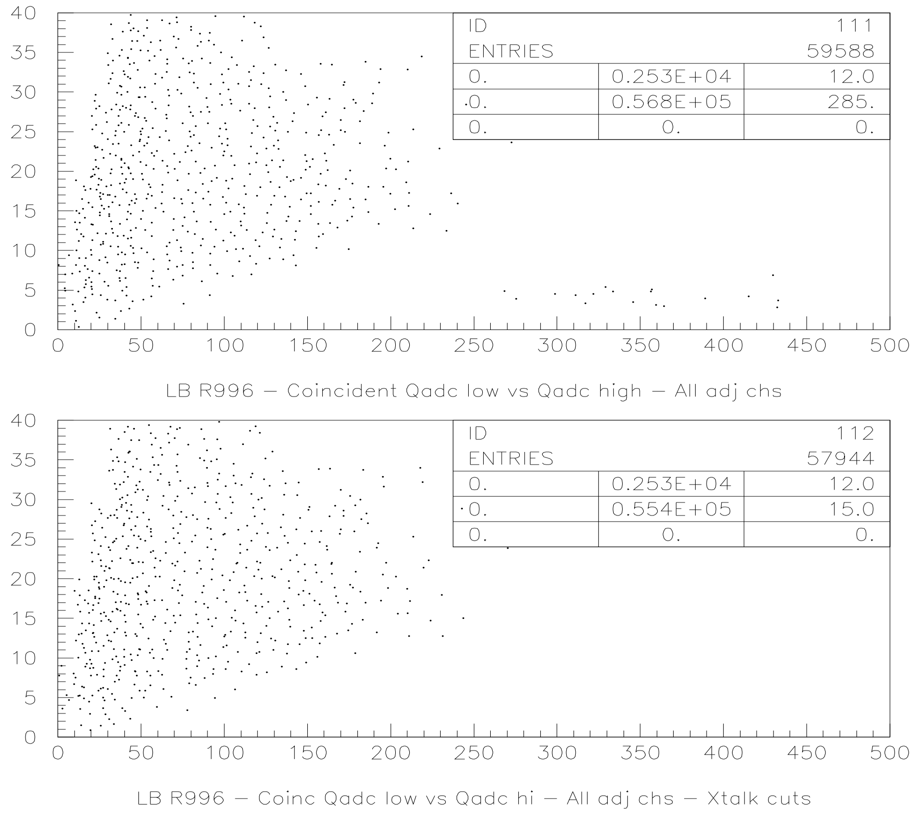


Figure 4.4: Laserball run 996: Similar to Figures 4.2 and 4.3 but using QHL pedestal subtracted ADC counts for the charge rather than calibrated charge. The top plot shows the uncut signal plus crosstalk background and the bottom plot has the crosstalk cut applied. The number of entries on each plot can be used to calculate that 2.8% of the PMT hits that were cut.

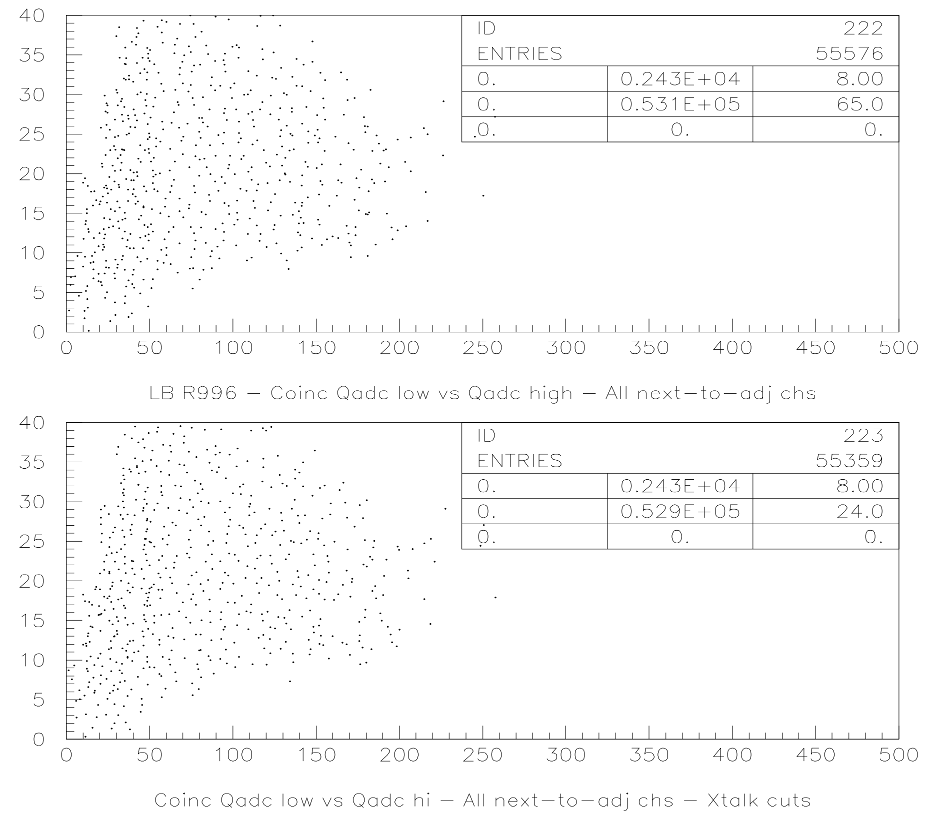


Figure 4.5: Laserball run 996: Similar to Figure 4.4 but with next-to-adjacent channels rather than adjacent channels. The units of charge on both axes are pedestal subtracted ADC counts. The number of entries in each plot can be used to calculate that 0.4% of the PMT hits were cut.

(2) coincidences on adjacent SNOD chips from the same daughter card (large X's),

(3) coincidences on the same daughter card (filled circles), and

(4) coincidences on adjacent daughter cards (triangles).

It is seen that there are anticorrelations for all functions shown except for the case of adjacent daughter cards. The positive correlation for this case is larger than that of the LB data shown in Figure 4.1 above. For now, it is assumed that the level of correlation for the adjacent daughter card SE function defines the level for uncorrelated signals. The anticorrelation for "same SNOD" coincidences (10%) is twice that of the "adjacent SNOD" coincidences (5%). The "same daughter card" SE correlation function is redundant information as it includes the latter two cases. It can be seen that it represents the average of the "same SNOD" and "adjacent SNOD" functions. It is equal to the latter function for $\Delta channel > 3$ since there are only 4 channels on a chip.

Figure 4.7 shows that Monte Carlo (MC) simulations of this effect can reproduce the anticorrelation at small angles with quantitative accuracy. A SNOMAN MC simulation has been carried out in which the charges in PMTs from coincidences on the same SNOD chip were lowered by 10%, and charges from coincidences on adjacent chips from the same daughter card were lowered by 5%. The MC does not show the positive 0.4% correlation offset of the LB data but does show the anticorrelation at small angles with the same magnitude as the LB data. The LB data has the crosstalk

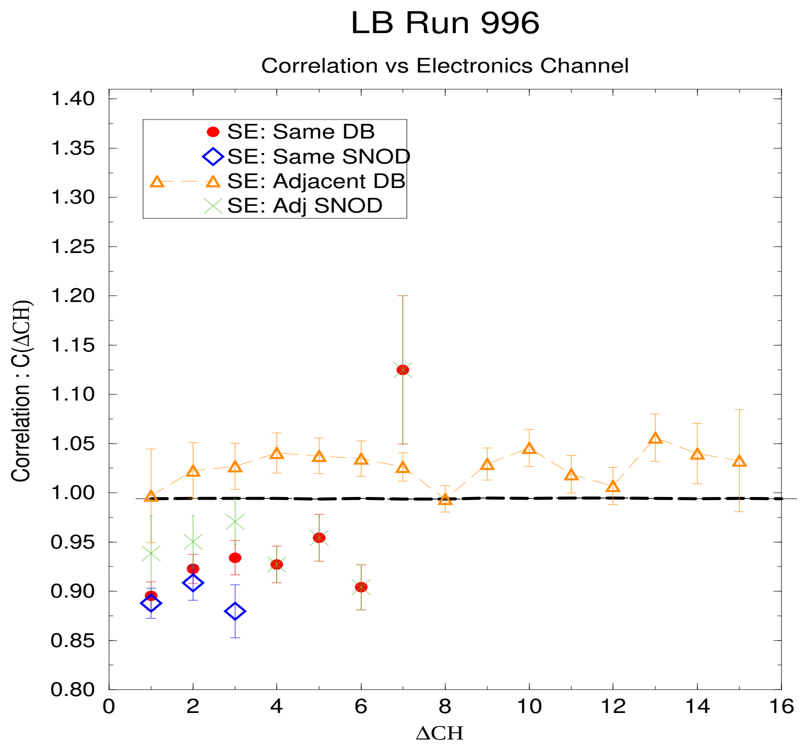


Figure 4.6: Laserball run 996: SE Correlation functions vs. $\Delta channel$, the difference between the channel numbers of two given electronics channels. This is done for "same daughter card" (or "same DB") coincidences (filled circles), "same SNOD discriminator chip" coincidences (open diamonds), "adjacent SNOD chip, same daughter card" coincidences (large X's) and "adjacent daughter card" (or "adjacent DB") coincidences (open triangles). All SE functions show an anticorrelation except the adjacent daughter card case which is consistent with the 0.4% positive correlation offset mentioned above.

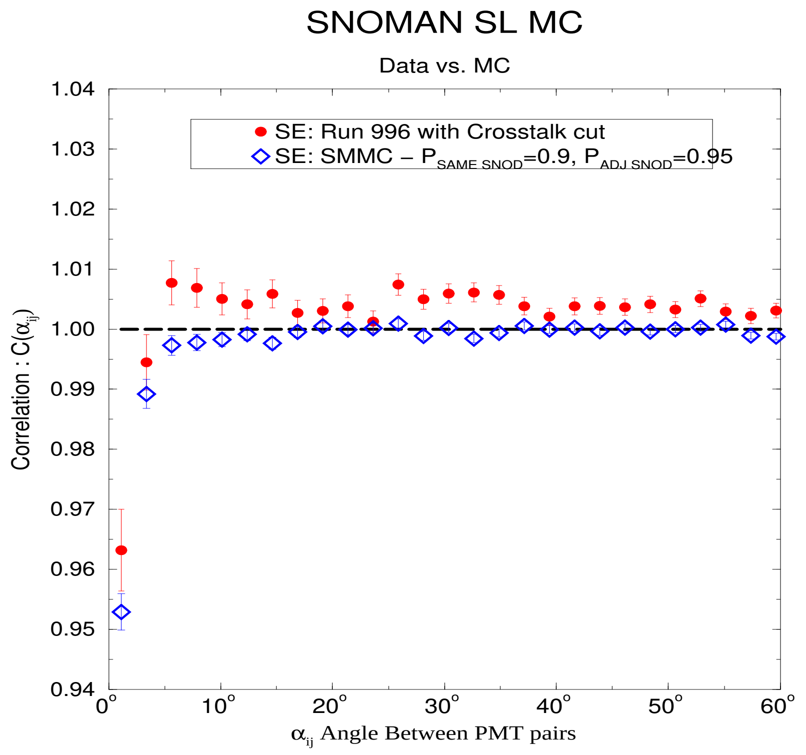


Figure 4.7: LB run 996 and a SNOMAN SL Monte Carlo simulation of the daughter card systematic. The results show good agreement between the simulation and the data but for the 0.4% positive correlation offset which will be discussed further below.

cut made while no cut is needed for the MC simulation which has no crosstalk. The quantitative agreement shows both that the model is consistent with the data and that the crosstalk cut is correct.

### 4.2.3 Comparison of LB Data With PMT Hit and Charge Correlation Functions

It has been shown that electronic crosstalk leads to a positive correlation at small angles for the PMT hit SE correlation function. A rare systematic effect due to coincidences between channels on the same daughter card yield anticorrelations at small angles for the charge SE correlation function. Both effects should contribute to both types of correlation functions. Why is the PMT hit SE correlation function positively correlated while the charge SE correlation function is anticorrelated in Figure 4.1?

Figure 4.8 shows plots of the PMT hit and charge SE correlation functions for data sets before and after the crosstalk cut was applied. Consider the charge correlation functions first. The 2% anticorrelation in the first data point before the cut becomes a 4.5% anticorrelation after the cut. This is expected since most of the adjacent channels are adjacent PMTs as well and some adjacent channel hits have been removed by the cut.

Consideration of the PMT hit SE functions shows that the 2% positive correlation in the first data point before the crosstalk cut becomes consistent with the data at other angles when the crosstalk cut is made, *i.e.* the correlation function becomes flat for all angles. There are two possible explanations for this:

(1) the PMT hit correlation is not affected by the daughter card anticorrelation, or

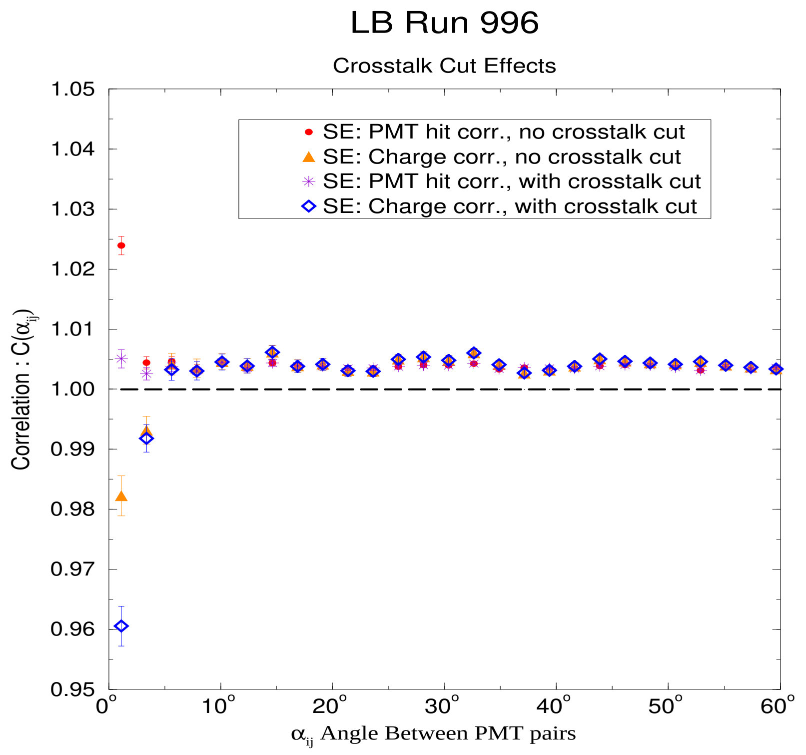


Figure 4.8: LB Run 996: PMT hit and charge SE correlation functions before and after the crosstalk cut is applied. Note that after the crosstalk cut is applied, the PMT hit SE function is consistent with a uniform distribution at all angles.

(2) there is an effect which exactly cancels the anticorrelation for the PMT hit correlation and does not affect the charge correlation.

The first explanation is the more plausible one. In this case, the daughter card "anticorrelation" affects the charge distribution in some way but not the *number* of photons being detected. Thus the PMT hit SE correlation function, which is blind to charge, would not show an anticorrelation while the charge SE correlation function would. It is possible that, although precautions were taken to prevent such an effect [78, 79], a charge pulse on a given SNOD chip or daughter card could cause the pedestals of the other channels on the daughter card to be increased for a short time. This would result in a lower charge measurement for subsequent charge pulses while not eliminating them. This would have to happen on time scales of a few $ns$ because all of the PMT hit coincidences occur with a time window of $15ns$. It is difficult to model how such a fast response time could come about.

It is deemed from Figure 4.8 that the proper SE correlation function to use for subsequent analysis is the PMT hit SE function as it is uncorrelated for all angles after the crosstalk cut is made for the LB data. For convenience, it is shown with the DE function in Figure 4.9. The only remaining feature is the aforementioned 0.4% positive correlation offset which is discussed below.

### 4.2.4 Laserball Time Correlations

In this section, it is shown that the LB exhibits small but measurable intensity fluctuations. The degree of these fluctuations has been measured using the time correlation function described in Chapter 3, Section 3.5.5. Figure 4.10 shows a plot of the time correlation function for LB run 996. The same event correlation function is averaged to a point shown at a time between events of zero. The next point is the average of the adjacent events correlation function, *etc.* The different events function is an

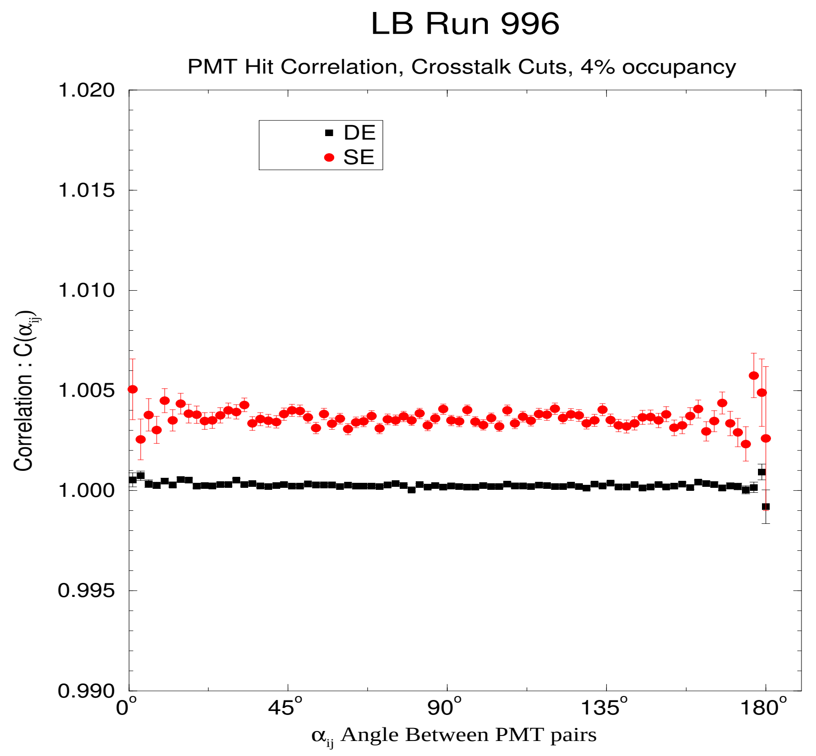


Figure 4.9: Laserball run 996: Same event and different events dynamic PMT hit correlation functions after the crosstalk cut has been made. Note that both functions are flat over the entire angular range but that the SE function has a positive correlation offset while the DE function does not.

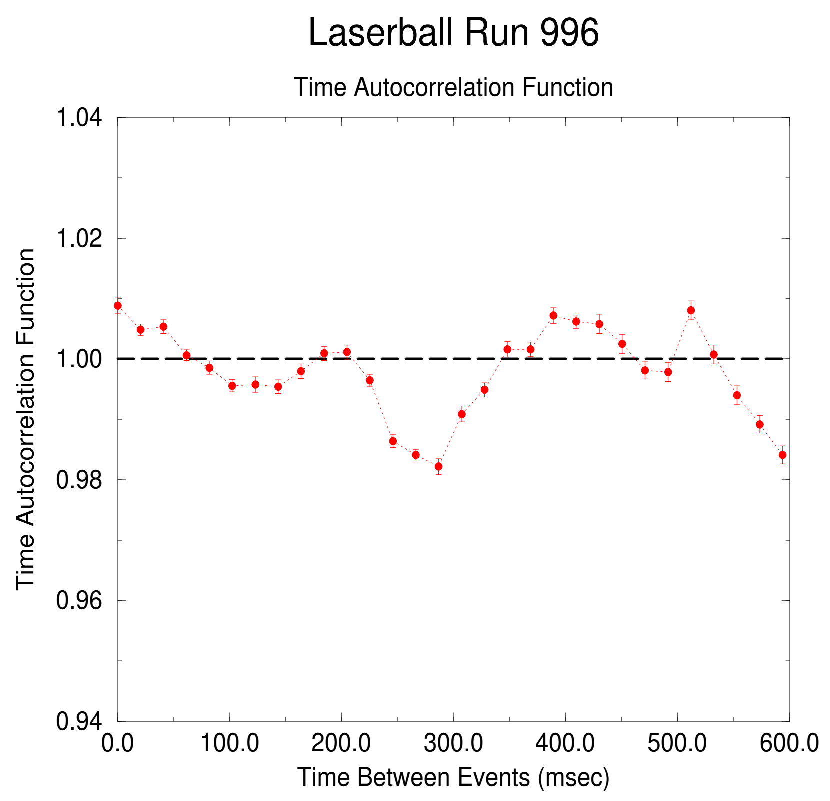


Figure 4.10: LB Run 996: Time autocorrelation function for the LB. It is seen that intensity fluctuations occur with a period of approximately $150 - 200$ *msec* and a *correlation* amplitude of $\sim 3.5\%$. The actual amplitude of the intensity fluctuations is measured to be $9.5\%$.

average of the first ten data points shown in Figure 4.10. It is seen that there are periodic fluctuations in the correlation over time with a period of approximately 150 $msec$ and an amplitude of approximately 0.9%. In the model of a perfect sine wave oscillation, the average positive offset would then be $0.9\%/2 = 0.45\%$ which is the value observed in Figure 4.9. The analysis of a simple sine wave periodic model of time correlations in Section 3.5.5 showed that the measured positive correlation offset of the SE correlation function is related to the amplitude of the fluctuations $\epsilon$ by:

$$SE_{positive\ correlation\ offset} = \frac{\epsilon^2}{2}. \tag{4.1}$$

Substitution of $SE_{positive\ correlation\ offset} = 0.45\%$ gives an average intensity fluctuation of 9.5%. This is in agreement with an analysis of the NHIT vs. event time plot for LB run 996 (not shown).

### 4.2.5 Discussion of the Systematic Effects

The crosstalk and daughter card systematic anticorrelations are understood to some degree and both can be corrected for in the analyses presented below. The crosstalk background can be cut efficiently and the daughter card systematic can be eliminated by using the PMT hit SE correlation function which is not sensitive to the effect. The daughter card systematic will not effect solar neutrino analyses as they rely solely on the number of Cerenkov photons and not on the PMT charges. The crosstalk systematic falsely increases the number of hits observed but the effect is very small, especially for solar neutrino events which have small charges and detector occupancies. The crosstalk cut developed can be used to reduce this already small background even further.

The positive correlation offset is observed to some degree in all the SNO data analyzed by the author. The positive correlation offset will not affect the solar neutrino analyses of SNO. In the analyses that follow, it will be assumed that this positive offset defines the level of uncorrelated signals for same event correlation functions. The three main analyses of this thesis will now be presented individually.

## 4.3 Back-To-Back Photon Correlations

As mentioned in Chapters 1 and 3, the QED, or Casimir effect, theories of SL all predict that photons occur in pairs and are emitted back-to-back and with equal energy to a first approximation. In order to test the hypothesis of back-to-back photon correlations an analysis was carried out using data taken with a sonoluminescence source in the SNO detector. The analysis is described below.

### 4.3.1 Monte Carlo Studies

Monte Carlo (MC) studies have been undertaken to study SNO's sensitivity to back-to-back photon correlations. The SNOMAN software was modified by the author enabling simulation of the effect. In these simulations, both members of a correlated

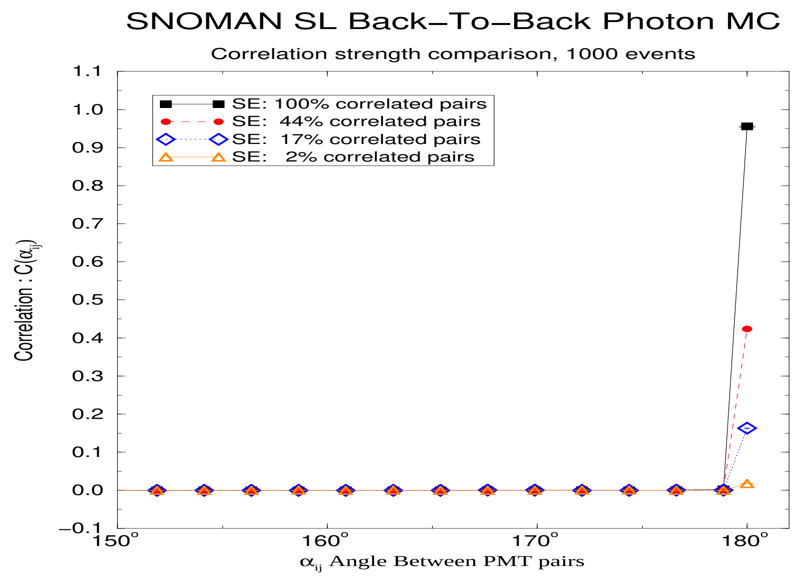


Figure 4.11: SNOMAN SL Monte Carlo simulation of 100%, 44%, 17% and 2% back-to-back pairs of photons.

pair have the same energy, position and time and have opposite direction and polarization. Each correlated pair of photons is random with respect to any other photons in the event. The strength of the correlations is controlled by the fraction of photons that have correlated partners.

These MC data are analyzed with the "same event" (SE) and "different events" (DE) correlation functions discussed in Chapter 3, Section 3.6. They have been normalized by the correlation at zero lag and unity has been subtracted from them. This makes them true correlation functions in which uncorrelated signals have a correlation value of zero, and positive correlations (anticorrelations) have positive (negative) values in the range [-1,1]. Correlation analyses of four such MC data sets are shown in Figure 4.11 where 100%, 44%, 17% and 2% of the photons pairs were correlated. All of the detector inefficiencies have been removed except for the 55% effective photocathode coverage. Only the region near $\alpha = 180^\circ$ is shown for clarity. The data point at $180^\circ$ shows a $(95.5 \pm 0.2)$% correlation for the 100% correlated pair simulation. The correlation for this data point is not 100% because the angle of separation between pairs of PMTs in this data bin is not always exactly $180^\circ$ . This leads to an inefficiency where one member of a pair is detected at the edge of a PMT and the other member just misses the PMT on the opposite side of the detector. The observed correlation of the last data points for the 44%, 17% and 2% strength cases are $42.2 \pm 0.1$%, $16.3 \pm 0.1$% and $1.8 \pm 0.1$% respectively. The values expected when corrected for the inefficiency of the 100% correlated case are 42.0%, 16.2% and 1.9% respectively. The observed values are consistent with the expected result.

Several systematics have a significant effect on the measured correlation strength. Figure 4.12 shows the SE correlation analyses for several MC data sets. All sets were generated with 100% correlated pairs but each added a different photon collection inefficiency effect to the simulation. The case of 100% detector efficiency is also shown for comparison. The effect of Fresnel scattering on the PMTs and acrylic vessel (AV) reduces the observed correlation by 8%. Adding Rayleigh scattering in the AV does not change the value of the correlation significantly as few photons are scattered in

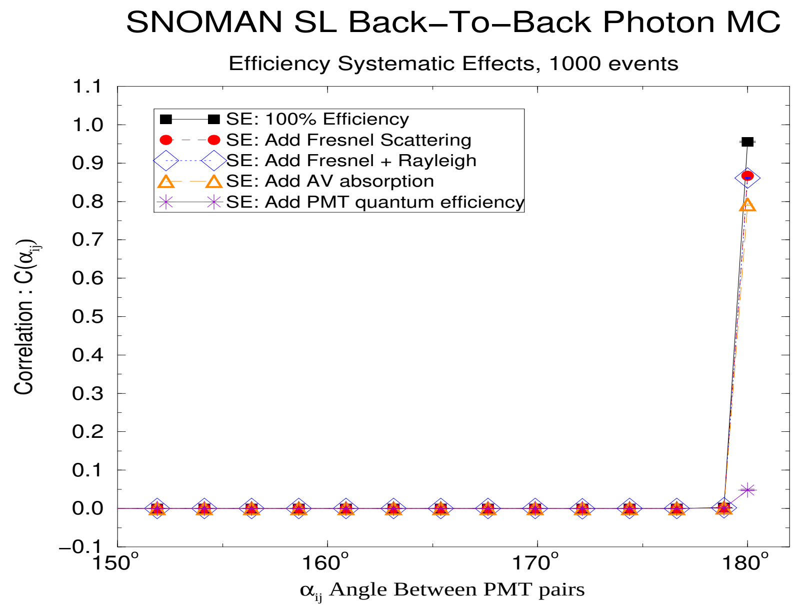


Figure 4.12: SNOMAN SL Monte Carlo simulation of 100% back-to-back pairs of photons. The effect of Fresnel scattering, Fresnel + Rayleigh scattering, acrylic vessel (AV) absorption and PMT quantum efficiency on the correlation are shown.

this manner. Absorption in the AV causes a reduction in the observed correlation of 16%. The PMT quantum efficiency causes the correlation at 180° to drop to 5% for 100% correlated pairs, a factor of 19% smaller than the value for the perfect detector efficiency case. This is explained by the 19% PMT quantum efficiency averaged over the SL photon energy spectrum. All of the effects described systematically reduce the observed correlation except Rayleigh scattering. The Fresnel scattering probabilities at the AV and PMTs, the AV absorption, and the PMT quantum efficiency as functions of wavelength are measured as part of the optical calibration procedure in SNO. This calibration is not yet complete. Therefore, MC values for these parameters, which have been obtained from measurements of the materials before SNO was constructed or estimated from other sources [80, 81], are used in the back-to-back correlations analysis of SL data described below.

Other systematic effects are due to SL source location and mismeasurement of the location. The source location affects the correlation function by determining the angle between PMT pairs. Figure 4.13 shows the results of analyses of MC data sets with source locations at the detector center, and displaced to (x,y,z) = (-10,+25,0) cm. Two analyses of the latter MC data set have been done. In the first, the assumed location of the source is the detector center. In the second, the correct location is used. It is seen that when the wrong location is used in analysis, the measured correlation gets spread out and drastically reduces in magnitude. When the correct location is

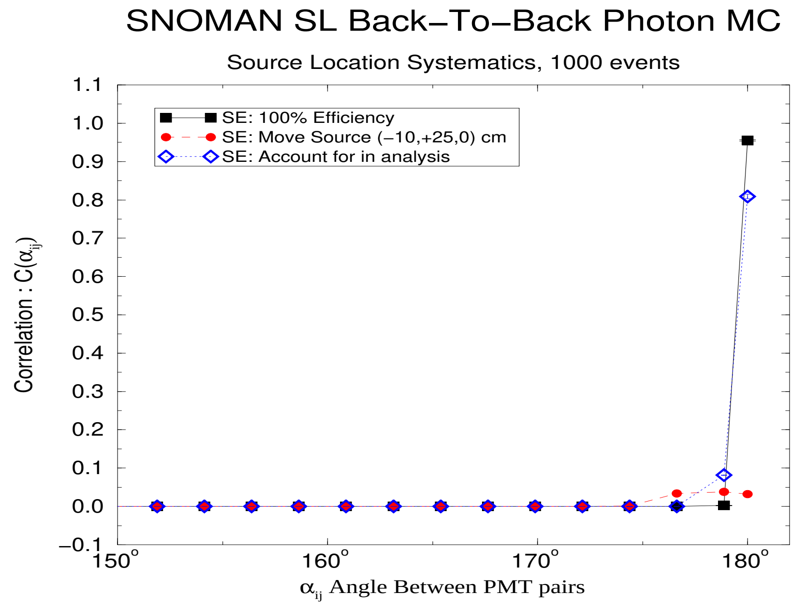


Figure 4.13: SNOMAN SL Monte Carlo simulation of 100% back-to-back pairs of photons. Moving the SL source away from the detector center while assuming it is at the center in analysis causes a spread in the correlation. When the analysis uses the correct source location, most of the spreading disappears.

used in analysis, the spread is less and correlation stronger, but not equivalent to the perfect correlation case. Thus moving the source alone introduces a systematic effect and mismeasurement of the location makes the effect worse. In Chapter 3, Section 3.4 it has been shown that the reconstruction accuracy in each Cartesian component of the source location is $7-10cm$. Thus this systematic error may be significant in the back-to-back correlation analysis of SL data.

In summary, any detector effect that reduces the photon collection efficiency appreciably will be a systematic effect in the back-to-back photon correlation analysis presented below. Such effects include: Fresnel scattering, absorption of photons in the AV, PMT reflections and quantum efficiency, and discriminator threshold effects. These will all have to be accounted for in the analysis below. Measurements and calibrations of these quantities have not yet been made. Therefore, the estimated values for these quantities in the SNOMAN Monte Carlo will be used. Systematic errors on these quantities will be estimated conservatively.

### 4.3.2 Systematic Error Estimation

As shown above, the systematic errors can be grouped into two categories: 1) those due to photon collection inefficiencies, and 2) those due to uncertainties in the source location.

The detector has three main sources of photon collection efficiency as it relates to this experiment: 1) absorption in the acrylic vessel, 2), Fresnel scattering at the acrylic vessel and PMT face, and 3) overall PMT photon collection efficiency. These quantities have not yet been calibrated for SNO. Consequently, a conservative approach is taken in which the Monte Carlo simulation of these effects is used and the systematic error is assumed to be 10% for each of the three effects. Combining these in quadrature yields a systematic error of 17%. This systematic error is assumed to scale with the correlation strength in the fits performed below.

The systematic error due to uncertainty in source location is difficult to include as there is little or no signal in the data and the systematic error can therefore be much larger than the correlation for some data points. The systematic error is on zero. For this reason, it is not included in the fits presented below.

### 4.3.3 Experimental Results

Two experiments were undertaken to test the hypothesis of back-to-back photon correlations. The first used unfiltered SL light. The second used $420 \pm 10nm$ band pass filters attached to the side of the SL source to attempt a measurement of back-to-back correlations over a narrow band of wavelengths.

The first data set used the unfiltered SL source and the full detector (actually 55% of the PMT instrumentation was installed at that time). The SL source was placed as close to the center of the detector as possible, $(x, y, z) = (+10cm, -25cm, +10cm)$

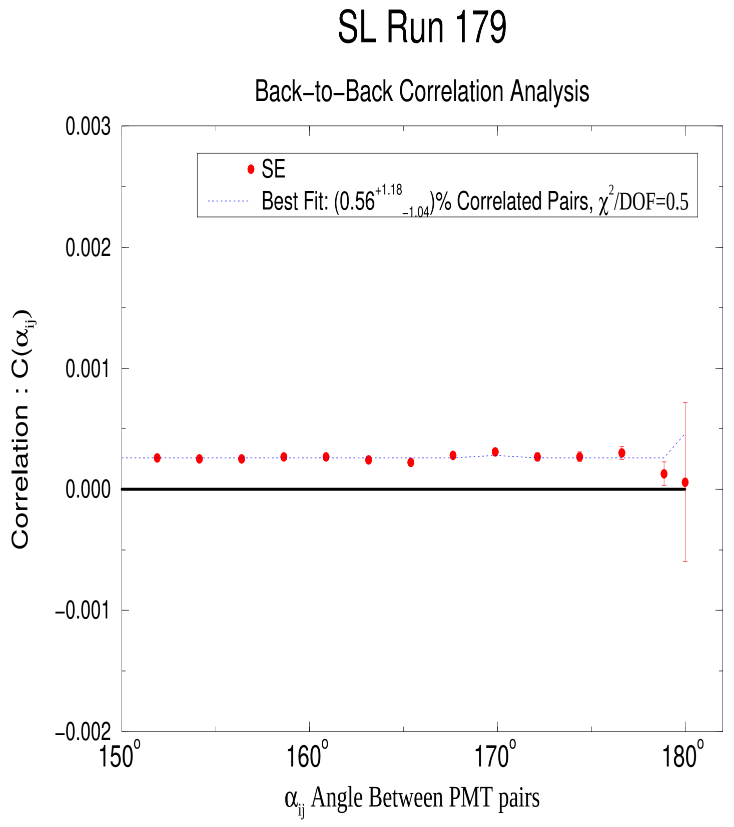


Figure 4.14: SL Run 179: Same event and different events dynamic PMT hit correlation functions with unity subtracted and normalized by the correlation at zero lag. Aside from the positive correlation offset, which is due to intensity fluctuations of the SL light, no significant back-to-back correlations are seen.

in detector coordinates, and 30 minutes of data were taken yielding 42,077 events. This run, SL run 179, has already been discussed in the previous chapter, Chapter 3.

The SE and DE correlation analyses were done on this data set and the results are shown in Figure 4.14. Only the region near 180° has been shown for clarity. The entire dynamic SE correlation function has an offset as discussed in Section 4.2. As stated in that section, this offset is assumed to set the level of uncorrelated signals for same event correlation functions. Aside from this offset, there is no significant correlation at angles near $\alpha = 180^\circ$ . The last data point is for PMT pairs which are exactly $180^\circ$ apart. The uncertainty on that datum is approximately 0.07%.

For the second set of data, a set of three $420 \pm 10nm$ bandpass filters were used to obtain information on both direction and wavelength (energy). The analysis of this data is shown in Figure 4.15. One can see that there are no significant back-to-back correlations in this data set.

Qualitatively, then, both data sets show no photon pair correlations. To be quantitative, one can use Monte Carlo to estimate the upper limit on photon pair correlations which are consistent with the data.

### 4.3.4 Fits To the Data

Figure 4.16 shows the SE correlation functions for Monte Carlo simulations of 10%, 20%, 30% and 40% correlated pairs respectively. The source location in the simulations was (x,y,z) = $(10cm, -25cm, 0cm)$, equivalent to the reconstructed source vertex of the source during the SL data runs described below. All detector photon collection inefficiencies are included in the simulations and the source location is the same as the reconstructed position of the two SL data sets which will be shown below. It is seen that only the last two bins show significant correlation. There is a linear relationship between the strength and the observed correlation in both of these MC

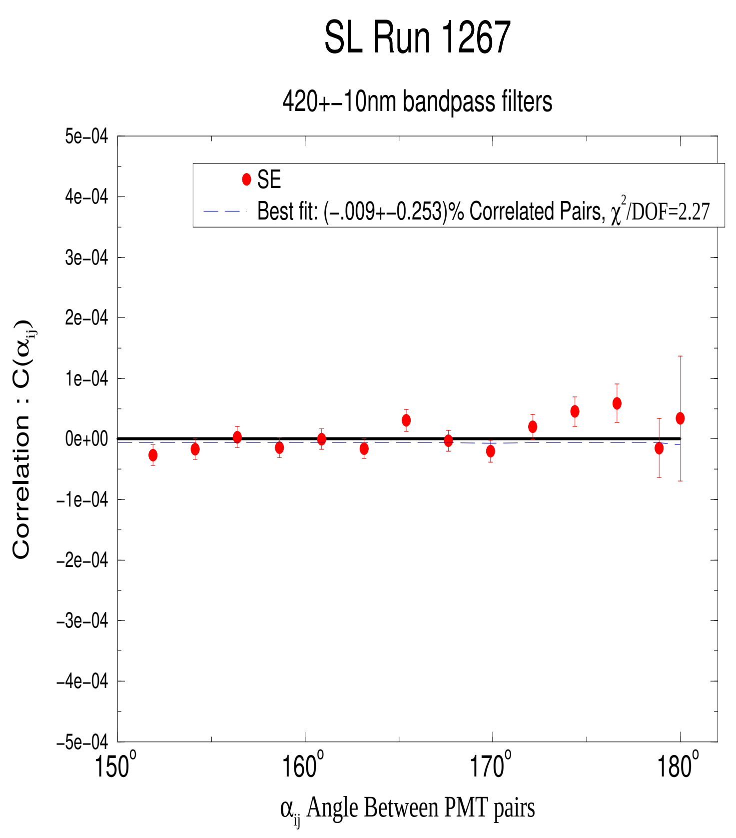


Figure 4.15: SL Run 1267: Same event and different events dynamic PMT hit correlation functions with unity subtracted and normalized by the correlation at zero lag. No significant back-to-back correlations are seen.

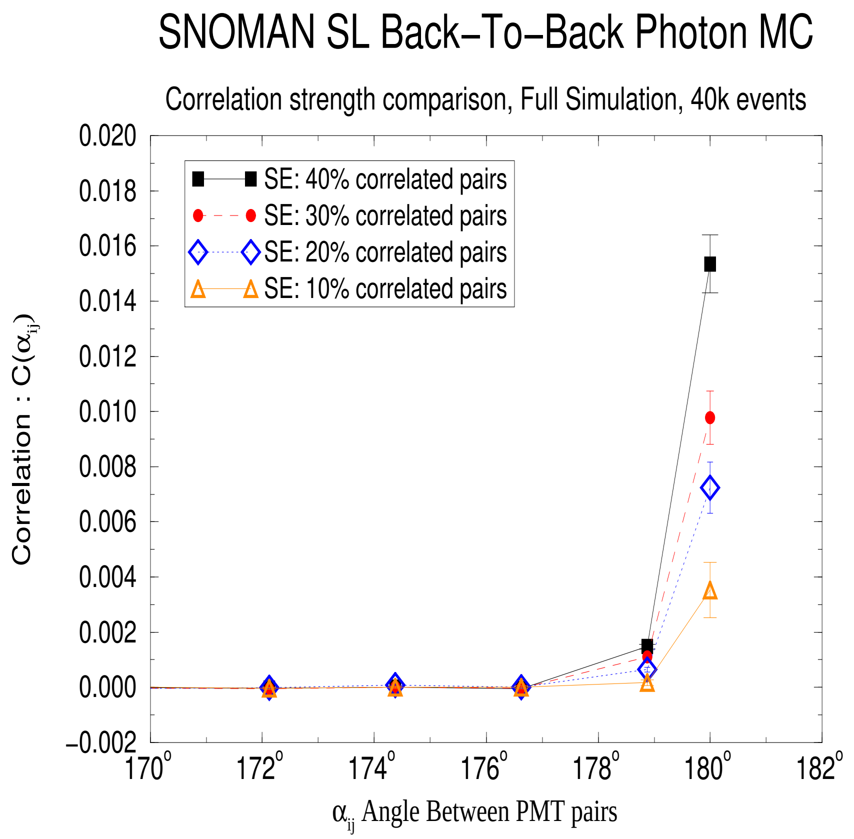


Figure 4.16: SNOMAN SL Monte Carlo simulation of 40%, 30%, 20% and 10% back-to-back pairs of photons with all photon collection inefficiencies included. The source location is $(x, y, z) = (10cm, -25cm, 0cm)$ in detector coordinates which is the reconstructed location of the source for the SL data sets described below.

data bins.

The theoretical value of the same event angular correlation as a function of correlation pair strength is determined from the full Monte Carlo simulations shown in Figure 4.16. As stated above, the SE angular correlation functions show a linear relationship between correlation strength and observed correlation. For the last two bins, the value of the correlation for 1% correlated pairs was determined by averaging the scaled results from each of the four MC data set correlation functions in Figure 4.16. These values were used to scale the theoretical correlation strength in the fits presented below.

Fits to the data are shown in Figures 4.14 and 4.15. Figures 4.17 and 4.18 show plots of the $\chi^2$ as functions of the fit correlated pair strength for fits to SL data runs 179 and 1267 respectively. The best fit value of both plots is less than $1\sigma$ from the null result of 0% correlation strength. Thus we interpret the data to be consistent with no photon pair correlations. The thick, dot-dashed lines on each plot delineate the 95% confidence level upper limit on the correlation strength. For unfiltered SL light from run 179, the upper limit is 3.1%. For filtered light of wavelength $\lambda = 420 \pm 10$ nm, the upper limit is 0.5%.

## 4.4 Angular Distribution of SL Photons

SNO, with its 9522 PMTs and spherical geometry, is an excellent detector for deterimining the angular distribution of a light source. Experiments were undertaken to measure the angular distribution of SL photons using the SNO detector. The data from SL run 179, described in Chapter 3, and above in regard to back-to-back photon correlations, was used in this analysis as well. As stated above, the SL source was deployed close to the center of the detector, $(x, y, z) = (10cm, -25cm, 0cm)$, and data were taken for 30 minutes. The analysis of these data in regard to the photon angular

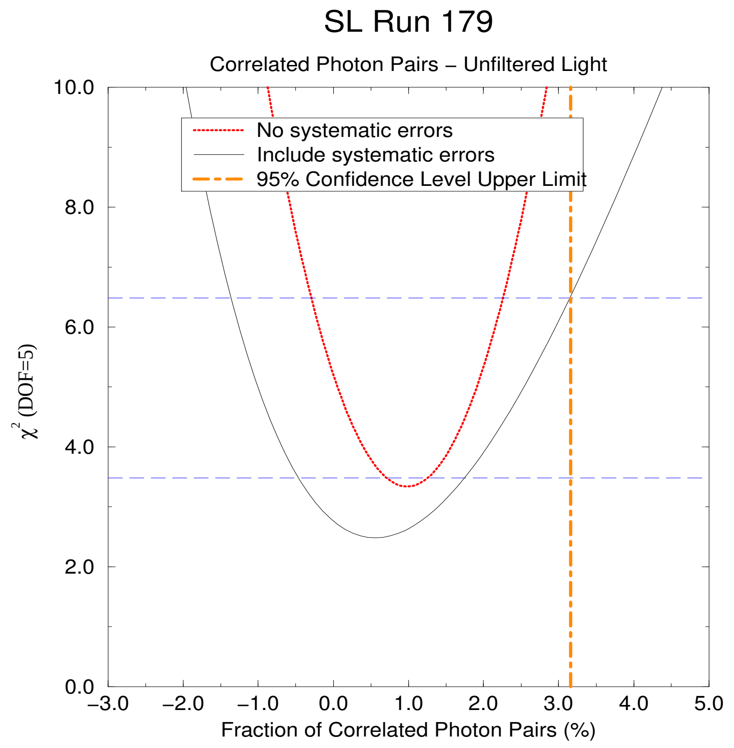


Figure 4.17: $\chi^2$ from a least squares fit of the last 5 data points of the SE correlation function from SL run 179 to Monte Carlo simulations of the effect. The strength of the correlation, or equivalently, the percentage of correlated pairs, is the fitting parameter. The 95% confidence level upper limit of the strength of correlated photon pairs is shown with a thick dot-dased line.

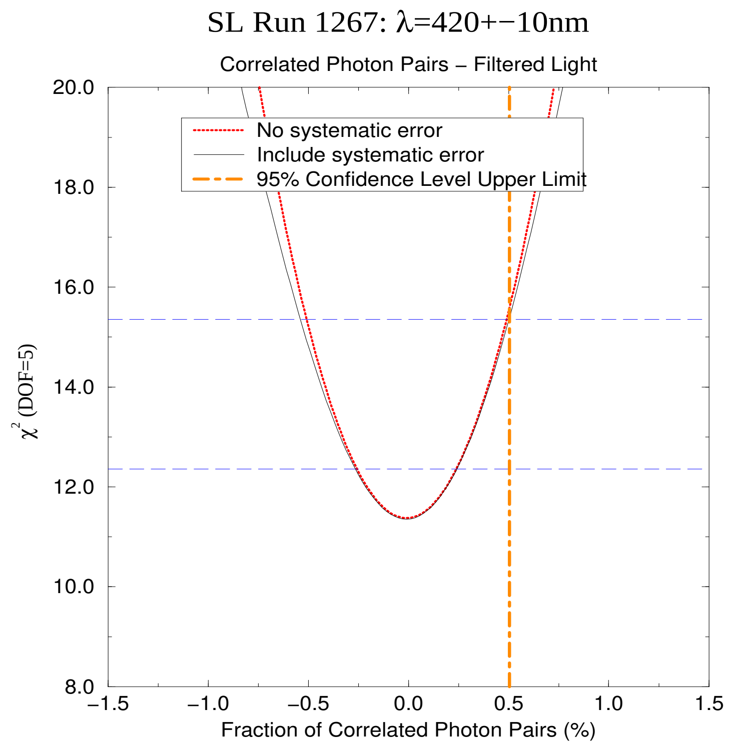


Figure 4.18: $\chi^2$ from a least squares fit of the last 5 data points of the SE correlation function from SL run 1267 ($\lambda$ = 420 $\pm$ 10 nm) to Monte Carlo simulations of the effect. The strength of the correlation, or equivalently, the percentage of correlated pairs, is the fitting parameter. The 95% confidence level upper limit of the strength of correlated photon pairs is shown with a thick dot-dased line.

distribution is presented below.

### 4.4.1 Monte Carlo Studies of Angular Distributions

Figure 4.19 shows the SE and DE analysis of a SNOMAN MC simulation of 20k SL events with a 10% dynamic dipole (see Chapter 3, Section 3.5) contribution to the otherwise isotropic angular distribution. The DE correlation is not quite flat as a function of angle but has a similar shape to that of the SE correlation function. This is due to the fact that the number of different events compared was $N_{compare} = 10$ rather than all different events. In the latter case, the function would have been flat. In the former case, there is still some "memory" of the dipole direction within 10 events from a given event. This behavior is repeated in the MC data set correlation function plots below.

A fit for the dipole and quadrupole strengths according to Equation 3.29 is also shown. Figure 4.20 shows the best fit point and $1\sigma$ and $3\sigma$ uncertainty ellipses in the parameter space of the dipole strength, $C_{10}^2$, and quadrupole strength, $C_{20}^2$. It is seen that the best fit dipole ($C_{10} = 10.0\%$) and quadrupole ($C_{20} \sim 0.0\%$) strengths are exactly equal to the generated values. The $\chi^2/DOF$ is 0.74 which is reasonable.

Figure 4.21 shows a similar plot for a 10% dynamic quadrupole ($Y_{20}$ only) simulation. The fit is again good with a $\chi^2/DOF$ of 0.73. The best fit point (asterisk) is roughly $1.5\sigma$ from the generated value (point where the dashed lines cross). Finally,

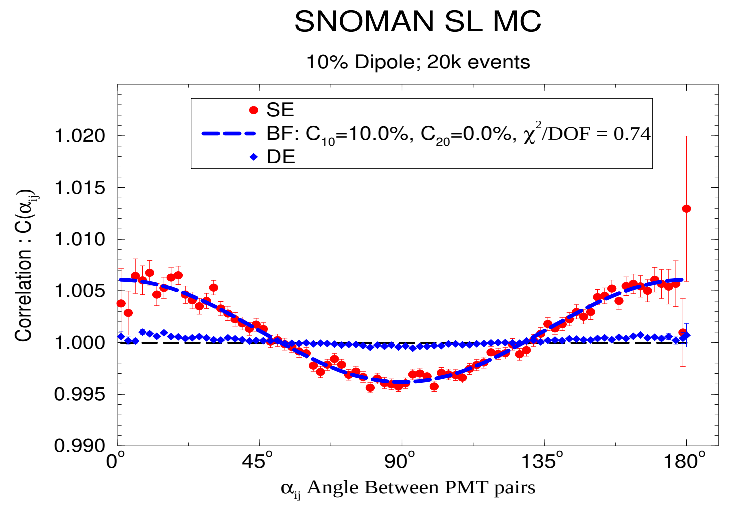


Figure 4.19: SNOMAN SL Monte Carlo simulation of a 10% "dynamic" dipole. Shown are the same event (SE) and different events (DE) correlation functions and a fit.

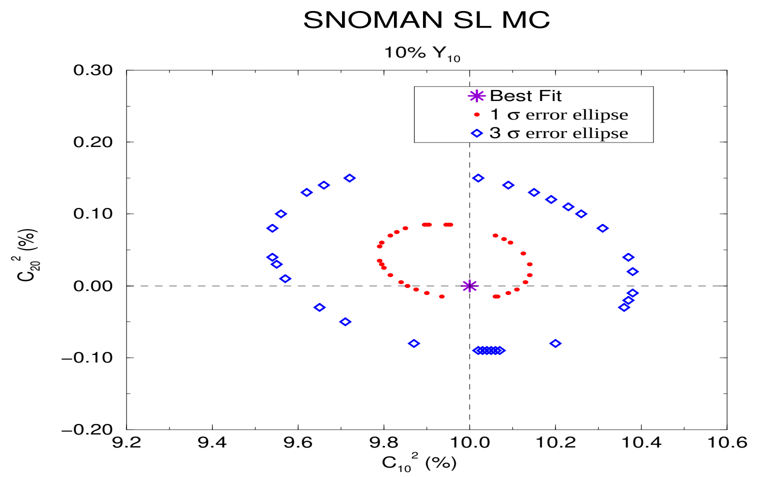


Figure 4.20: The best fit point and $1\sigma$ and $3\sigma$ error ellipses for the fit in the above plot are shown. The generated values are denoted by where the horizontal and vertical dashed lines cross.

a MC simulation of a coherent addition of 5% $Y_{10}$ and 5% $Y_{20}$ in the photon angular distribution is analyzed and shown in Figure 4.23. The uncertainty ellipses are shown in Figure 4.24. The best fit point is approximately $1.5\sigma$ from the generated value and the fit has a $\chi^2/DOF$ of 0.95. The analyses of these three MC simulations shows that the SNO detector has good sensitivity to multipoles with strengths at the $5-10\%$ level.

### 4.4.2 Experimental Results

#### Angular Distribution of Stable SL Data

Figure 4.25 shows the results of the angular correlation analysis for SL run 179 taken on May 5, 1998. Approximately 5500 electronics channels were calibrated and commissioned at that time, or $\sim 58\%$ of the full detector. There were some orange slice gaps on the PMT sphere from PMTs with uncommissioned electronics channels, but most of the coverage was fairly uniform. Also shown in Figure 4.25 are two fits. One to a coherently summed dipole and quadrupole, and one fit to the dipole only. Neither fit is good. Finally, the adjacent events and different events correlation functions are shown. Note that the detector trigger was prescaled by a factor of 1000 during SL run 179. Thus "adjacent events" are actually events that occured with an interval of 1000 times the SL period of $42\mu sec$, or $42msec$. Thus no correlations should be present for "adjacent events". It is seen that the adjacent events and different events

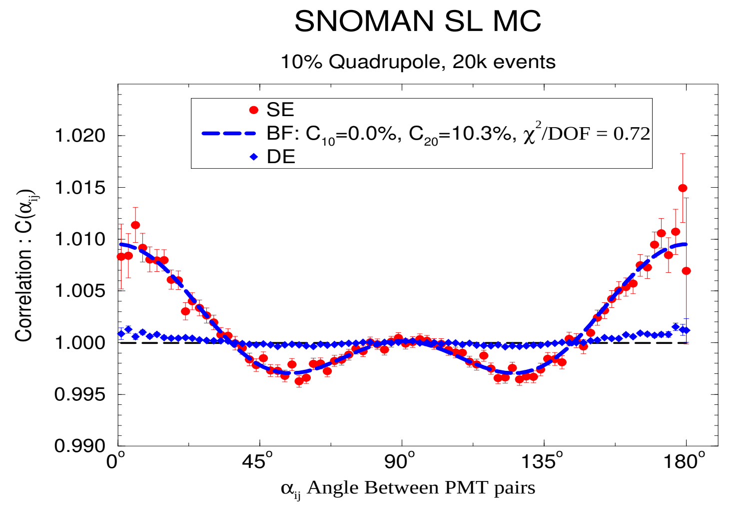


Figure 4.21: SNOMAN SL Monte Carlo simulation of a 10% "dynamic"quadrupole. Shown are the same event (SE) and different events correlation functions and a fit.

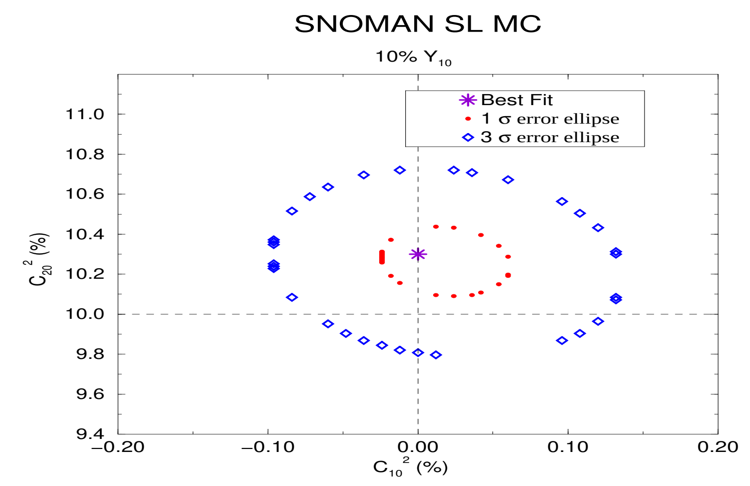


Figure 4.22: Best fit, $1\sigma$ and $3\sigma$ error ellipses for the fit in the above plot are shown. The generated values are denoted by where the horizontal and vertical dashed lines cross.

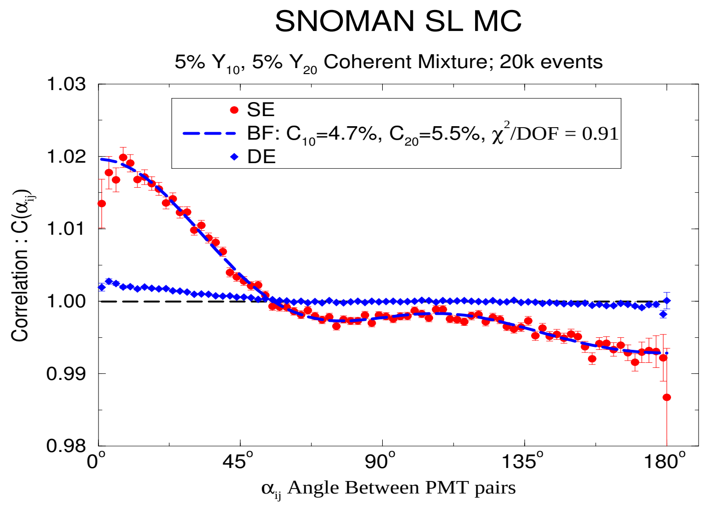


Figure 4.23: SNOMAN SL Monte Carlo simulation of a "dynamic", coherently summed, 5% dipole and 5% quadrupole angular distribution. The same event (SE) and different events (DE) correlation functions and a fit are shown.

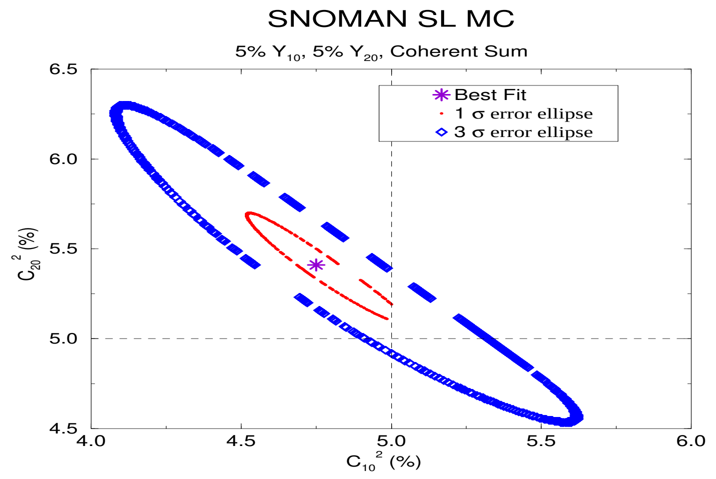


Figure 4.24: Best fit, $1\sigma$ and $3\sigma$ error ellipses for the fit in the above plot are shown. The generated values are denoted by where the horizontal and vertical dashed lines cross.

functions have a similar shape and offset. This behavior is not understood. However, it is assumed not to be true angular correlations. The DE correlation function is assumed to define uncorrelated signals.

Figure 4.26 shows the results of subtracting the DE function from the AE and SE functions and adding unity to both results. This preserves the strength of the correlation while bringing out the dynamic effects only. It is seen that the new AE function is uniform but the new SE function is not. A fit is shown which gives similar results to the fit for the uncorrected SE function in Figure 4.25. The best fit gives dipole and quadrupole strengths of $C_{10}^2 = (1.80 \pm 0.14)\%$ and $C_{20}^2 = (0.16 \pm 0.03)\%$ respectively. The $\chi^2/DOF$ is 1.8. The probability of obtaining a larger $\chi^2$ is $\sim 16\%$. This is interpreted to be a bad fit to the data. It is necessary to include more multipole components to the angular distribution to get a better fit. However, it is not clear what physical insight will be gained from such a fit. It is not clear from the data if the measured angular distribution is due to the true photon angular distribution or to diffraction of light at the SL bubble surface. If the surface is distorted from the spherical, it could cause the effects seen. This interpretation is consistent with interpretations of other, less sensitive, SL angular distribution measurements in the literature [1, 50].

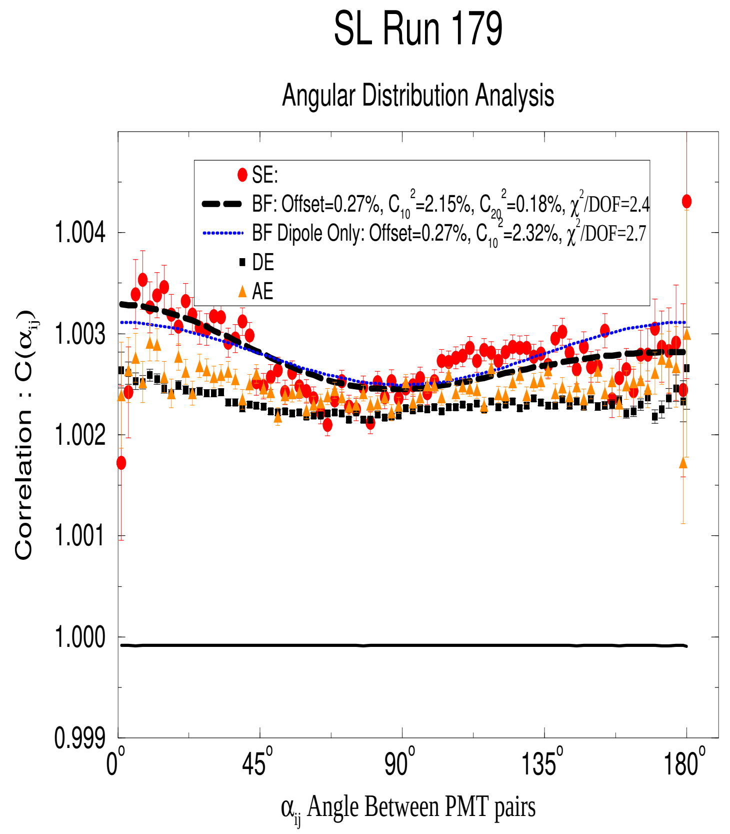


Figure 4.25: SL Run 179: Same event and different events dynamic correlation functions.

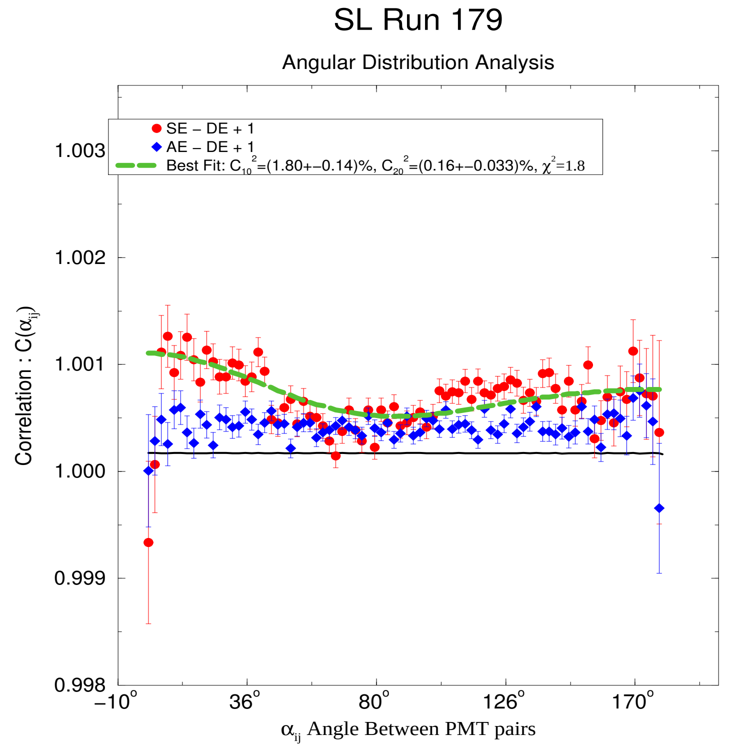


Figure 4.26: SL Run 179: Corrected same event and adjacent events dynamic correlation functions. Note that the AE correlation function is uniform while the SE function is not.

**Angular Distribution of Unstable SL Data**

To provide contrast to the relatively stable data of Figure 4.25, whose stability is seen from Figure 3.4 in Chapter 3, consider the plot shown in Figure 4.27. This SE correlation function was obtained from analyzing the first 3 minutes of SL run 1279 shown in Figure 3.5. The first 3 minutes of the run were relatively stable compared to the rest of the run but not compared to run 179. The SE correlation function has a similar shape to that of Figure 4.25 but the curve in Figure 4.27 is far more dramatic. A fit to the dipole and quadrupole strengths is shown. The dipole strength is $(6.5 \pm 0.6)\%$ and the quadrupole strength is $(0.28 \pm 0.05)\%$, and the fit has a $\chi^2/DOF = 1.7$. Thus light from unstable SL has larger dipole and quadrupole strengths than stable SL. This effect has been observed by others [1] who observe a dipole strength of $\sim 7\%$ in their data, consistent with this result. The run 1279 SE function was not corrected with the DE function as done for the run 179 SE function. This angular distribution is shown to provide contrast between stable and unstable SL light. Note that the angular distribution has a large positive correlation offset. There are also significant small and large angle anticorrelations relative to the correlation values at other angles. These anticorrelations are not understood.

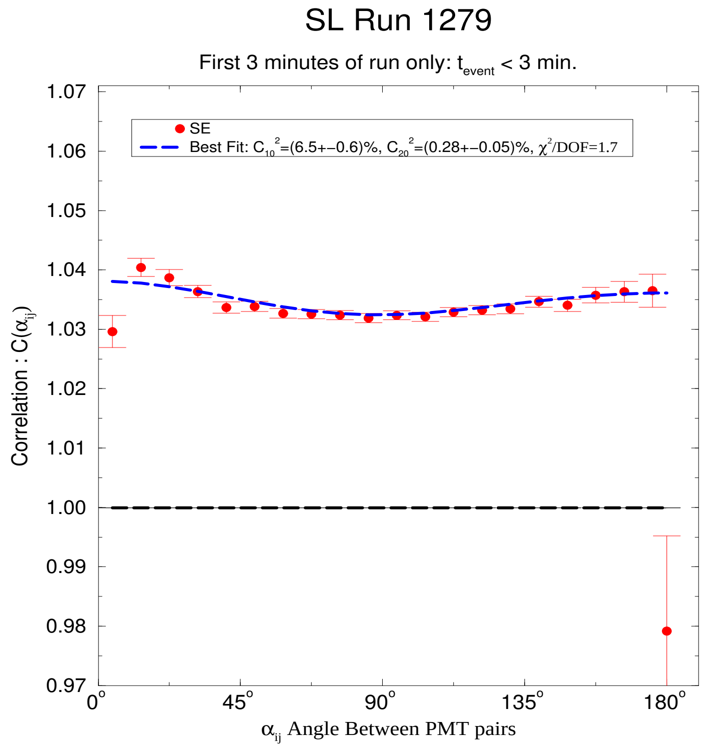


Figure 4.27: SL Run 1279: Same event dynamic correlation function for the “stable” portion of the run ($t_{event} < 3min.$, see Figure 3.5 in Chapter 3).

### 4.4.3 Discussion of Angular Distribution Experimental Results

The best fit values and their uncertainties shown in Figures 4.26 and 4.27 show that significant dipole and quadrupole contributions have been measured for both stable and unstable SL data. For the stable SL data set, the best fit dipole (quadrupole) strength is $13\sigma(5\sigma)$ from the null hypothesis of zero strength. For the unstable SL data set, the best fit dipole (quadrupole) strength is $11\sigma(5.2\sigma)$ from the null hypothesis. However, it is seen that the fits to the SE correlation functions are poor. The probability of getting a larger $\chi^2/DOF$ is approximately 16% (15%) for fits to the stable (unstable) data. A fit which includes contributions from other multipole moments would undoubtedly result in a better fit. However, it is not clear if physical insight would be gained from such a fit. We hypothesize that complex bubble motions may be contributing to the angular distribution - an interpretation consistent with previous results of lower sensitivity [1, 50]. These effects are extremely small but the experimental sensitivity is such that the effects are resolved.

## 4.5 Intensity Interferometry: The Method of Hanbury-Brown and Twiss

The method of Hanbury Brown and Twiss (HBT), dubbed “intensity interferometry”, has been used to attempt a measurement of the spot size of a SL source. This method was first used to measure the angular diameter of distant stars. Here, we calculate the same event PMT hit angular correlation function for number of data sets. By plotting the correlation as a function of $\alpha$ one can obtain, from Equation 3.38, the SL spot size, $R_{SL}$.

### 4.5.1 MC Simulations of Intensity Interferometry

The SNOMAN Monte Carlo and Analysis software package was modified such that it could generate photons with Bose-Einstein (BE) correlations. A simple routine was used which is similar to those in the references [82, 83]. The MC was used to check the analysis routine and to study the SNO detector's sensitivity to the effect.

Figure 4.28 shows the results of two SNOMAN SL Bose-Einstein Monte Carlos, one which had no Bose-Einstein correlations between the photons and one which did. In both cases the photons were generated from within a spherical region 200nm in radius at the center of the SNO detector and the photons are monoenergetic ($\lambda = 420nm$). One can see from the figure the shape expected in both instances. That is, there are significant correlations at small angles which reduce to an uncorrelated signal at larger angles. The width of the correlation in terms of angle gives the SL spot size for constant wavelength, as is seen from Equation 3.38. The amplitude of the correlation function which exhibits the intensity interferometry effect is not meaningful from these simulations as the SL Bose-Einstein MC does not reproduce the strength of the correlations properly - to do so would require thousands of times more computing time per event [83]. The shape of the curve, however, is not changed by the approximations

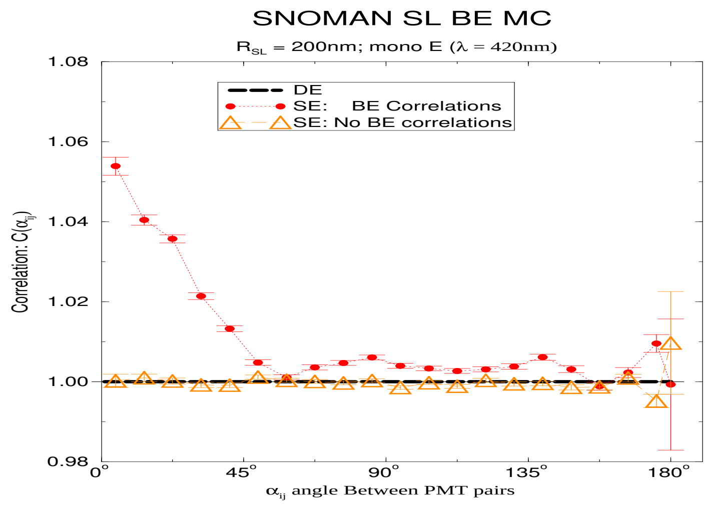


Figure 4.28: Analysis of two SL Bose-Einstein MCs - with and without Bose-Einstein correlations.

made in the MC.

Figure 4.29 shows the analysis of the SL spot size dependence and Figure 4.30 shows the wavelength dependence of the correlation function, using data generated with the SL Bose-Einstein Monte Carlo. The curves have the expected behavior: correlation peaking at zero opening angle ($\alpha = 0$), and widths that vary according to spot size and wavelength. This gives confidence that both the Monte Carlo and the analysis routine are correct.

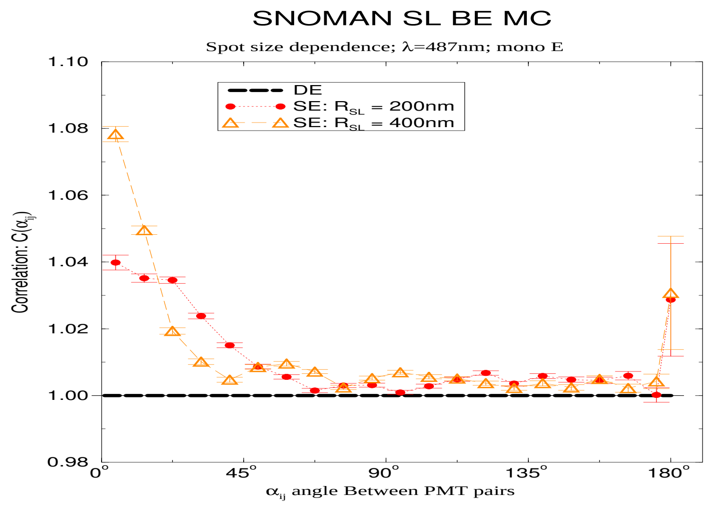


Figure 4.29: Analysis of a SL Bose-Einstein MC - SL spot size dependence.

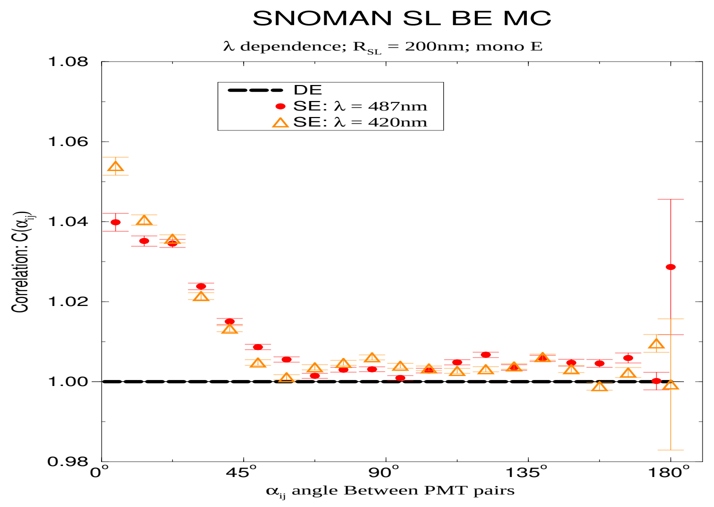


Figure 4.30: Analysis of a SL Bose-Einstein MC - wavelength dependence.

### 4.5.2 Experimental Results

Two experiments were undertaken to attempt to measure the SL spot size. For these experiments, three sets of narrow band pass filters of three different center wavelengths were attached to the exterior of the SL source. The filter wavelengths and band widths were: 1) $\lambda = 334 \pm 10$ nm, 2) $\lambda = 420 \pm 10$ nm, and 3) $\lambda = 487 \pm 1$ nm. The rest of the surface area was covered with dark material that absorbed all the photons striking it. Two small holes were cut in this material such that unfiltered SL light could escape. This light acted as a trigger for the source.

The first experimental run was run 1267. The second was run 1270 taken a few hours later. During the latter run, the trigger system was set to operate in "burst mode" such that adjacent SL pulses could be observed with long intervals of no triggers in between. The data cuts and analysis for these runs are presented below.

A special cut needed for this analysis is to demand that the light came through a filter. A plot of the number of hits in each PMT for direct light only vs. $\theta$ and $\phi$ (in detector coordinates) is shown in Figures 4.31 and 4.32. The approximate whereabouts of the filtered light was known by looking into the detector after the source was deployed. This acted as a check. The source was mostly covered allowing no light to escape except through the filters and two open holes. The plots of direct light Nhit vs. $\theta$ and $\phi$ (figures 4.31 and 4.32) show areas where the light is very intense which are the holes ($\theta \sim 36^\circ$ , $\phi \sim$ -40° ; $\theta \sim 100^\circ$ , $\phi \sim 40^\circ$ ; and a small

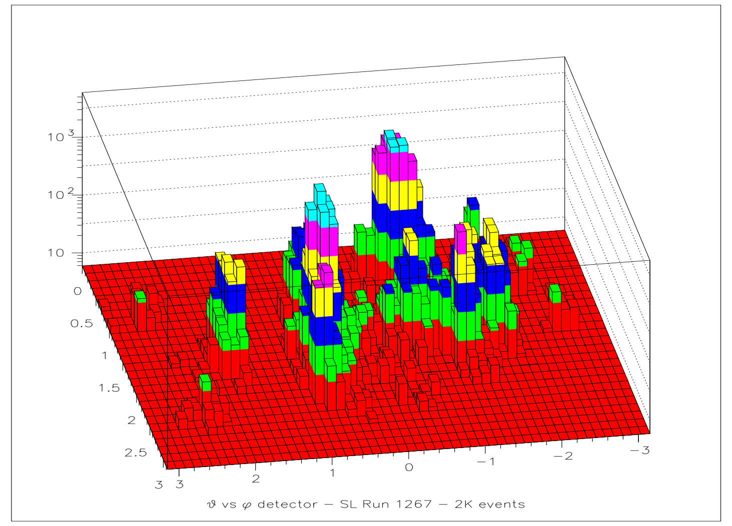

Figure 4.31: Run 1267: 3D Histogram of Nhit vs. $\theta_{detector}$ vs. $\phi_{detector}$ showing the regions of unfiltered light and regions of filtered light as well as some noise.

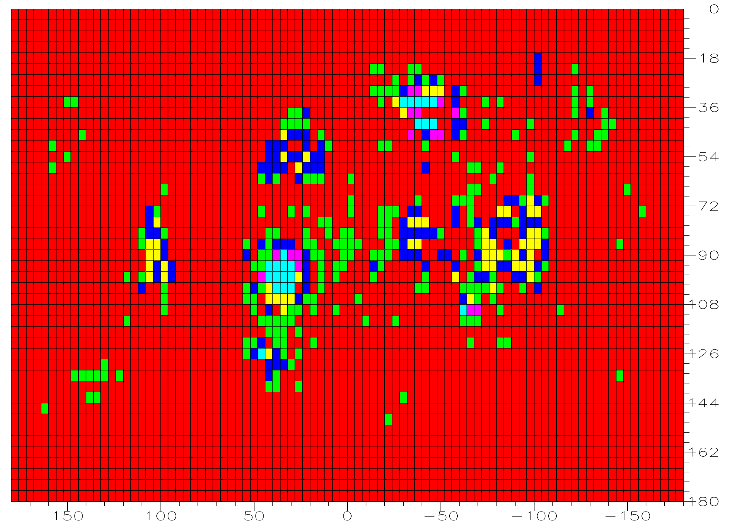

Figure 4.32: Top view of Figure 4.31 for clarity.

pinhole region near $\theta \sim 110^\circ$ , $\phi \sim$ -65° ) , areas of medium intensity which are the 10nm bandpass filters ($\theta \sim 90^\circ$ , $\phi \sim$ -30° , -80° and +100° ; and $\theta \sim 50^\circ$ , $\phi \sim 30^\circ$ ), areas of less intensity which are the 1nm bandpass filters (difficult to see, $\theta \sim 40^\circ$ , $\phi \sim$ -130, +150° ) and the background which is noise (all other regions). Note the logarithmic scale of the z-axis in Figure 4.31. A calculation of the angular acceptance of the filter given the source and detector geometries yields a region about 36° on a side which agrees with the plot. Only the filters near the center of these plots will look "square" (the shape of the filters) as the curvature of the detector has been projected onto the square space.

Other cuts that are not mentioned in Chapter 3, Section 3.3 are: cuts to remove out of sequence triggers and certain groups of triggers during seismic events and a minimum cut on the number of hits through all of filters and holes in a given event. All of the cuts eliminated about 8% of the total number of events. Table 4.1 summarizes the cuts used in run 1267 and the number left after each cut, although some events may have failed more than one cut.

The SE and DE correlation functions (see Equations 3.9 and 3.13 respectively) were calculated for three different sets of data, each set being the group of PMTs illuminated by: 1). the (single) 334±10 nm BP filter, 2). the set of three 420±10 nm BP filters, and 3). the set of two 487±1 nm BP filters. Figures 4.33 through 4.35 show plots of the correlations as a function of angle for the 3 data sets respectively.

| Cut description | # events left | Percentage cut |
|---|---|---|
| Total events | 2045711 | 100.0% |
| GTID = 0 (Orphan Cut) | 2018833 | 1.3% |
| Out of sequence triggers | 2018763 | 0.003% |
| Events during seismic activity | 1968765 | 2.4% |
| $N_{HIT} < 20$, $N_{HIT} > 200$ | 1930788 | 1.9% |
| $N_{HIT}$ (fltr & holes) $< 12$ | 1926096 | 0.2% |
| Asynchronous events | 1868970 | 2.8% |
| Total events cut | 176741 | 8.6% |
| Total events left | 1868970 | 91.4% |

Table 4.1: SL Filter Run 1267: event cuts and statistics.

None of the three plots shows the expected shape if Bose-Einstein correlations were present. The plots are all consistent with flat (although they all seem to dip at small angles) and would be consistent with no correlations at all except for the fact that the 334nm and the 420nm filter data sets are about 4% above where they should be if no correlations were present. This is not yet understood.

The statistics on the 487nm data set are poor as less light came through those filters and there just was not enough data. However, all data points are consistent with no correlations although the curve does appear to have a shape to it.

The different events correlation functions have offsets and are not flat as a function of angle but they will be assumed to define uncorrelated signals. The procedure is to subtract the DE function from the SE function and then add unity. This preserves all of the characteristics of the SE function, while removing any shape bias which is probably due to filter characteristics and not physics. Figures 4.36, 4.37 and 4.38 show the result of such corrections for the $334 \pm 10$ nm, $420 \pm 10$ nm and $487 \pm 1$ nm band pass filter data sets respectively.

### 4.5.3 Systematic Checks

Some simple systematic checks can be performed on the data and will be described in this section. Some of them required separate experiments and some merely different analyses.

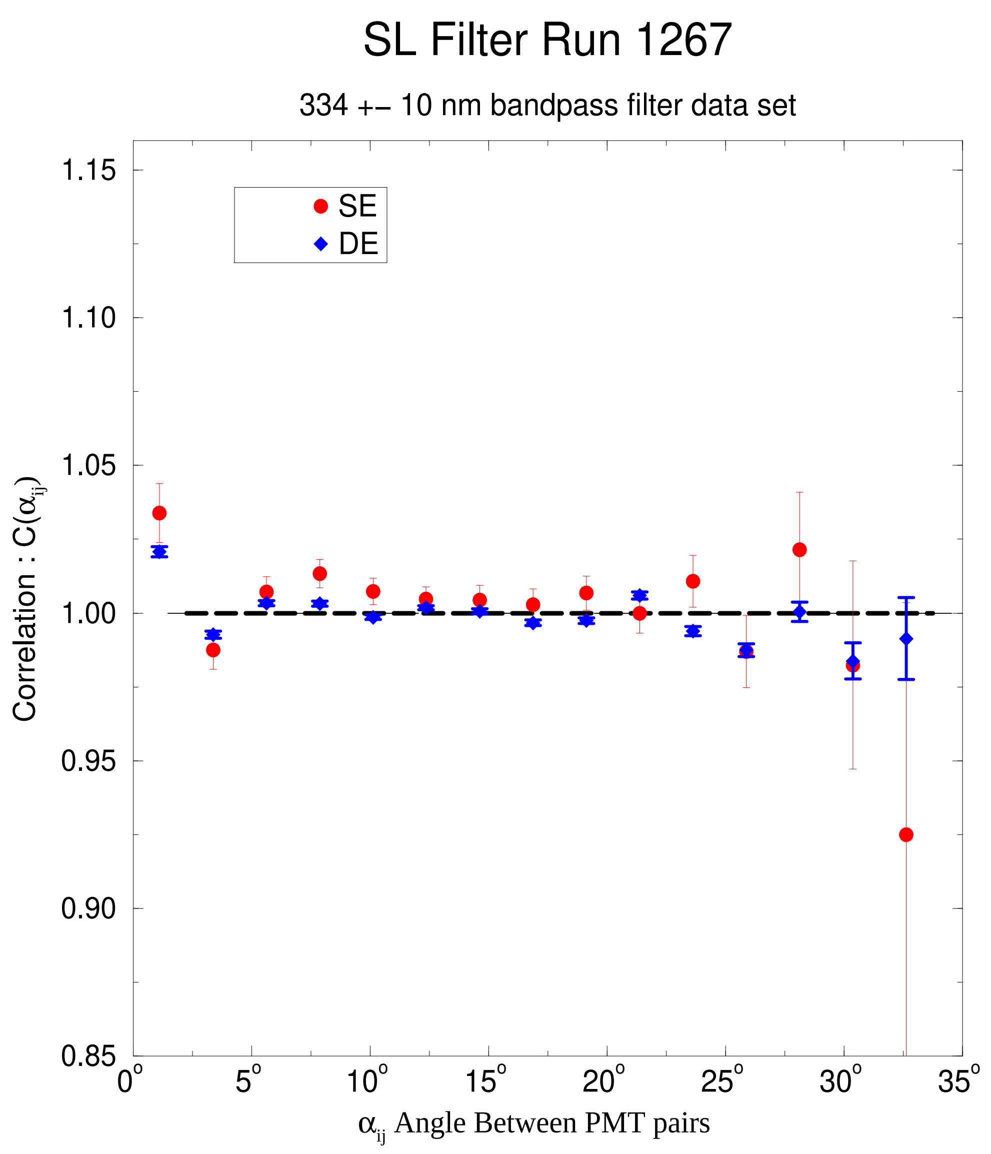


Figure 4.33: SE and DE vs. $\alpha$ for the 334±10 nm BP filter data set.

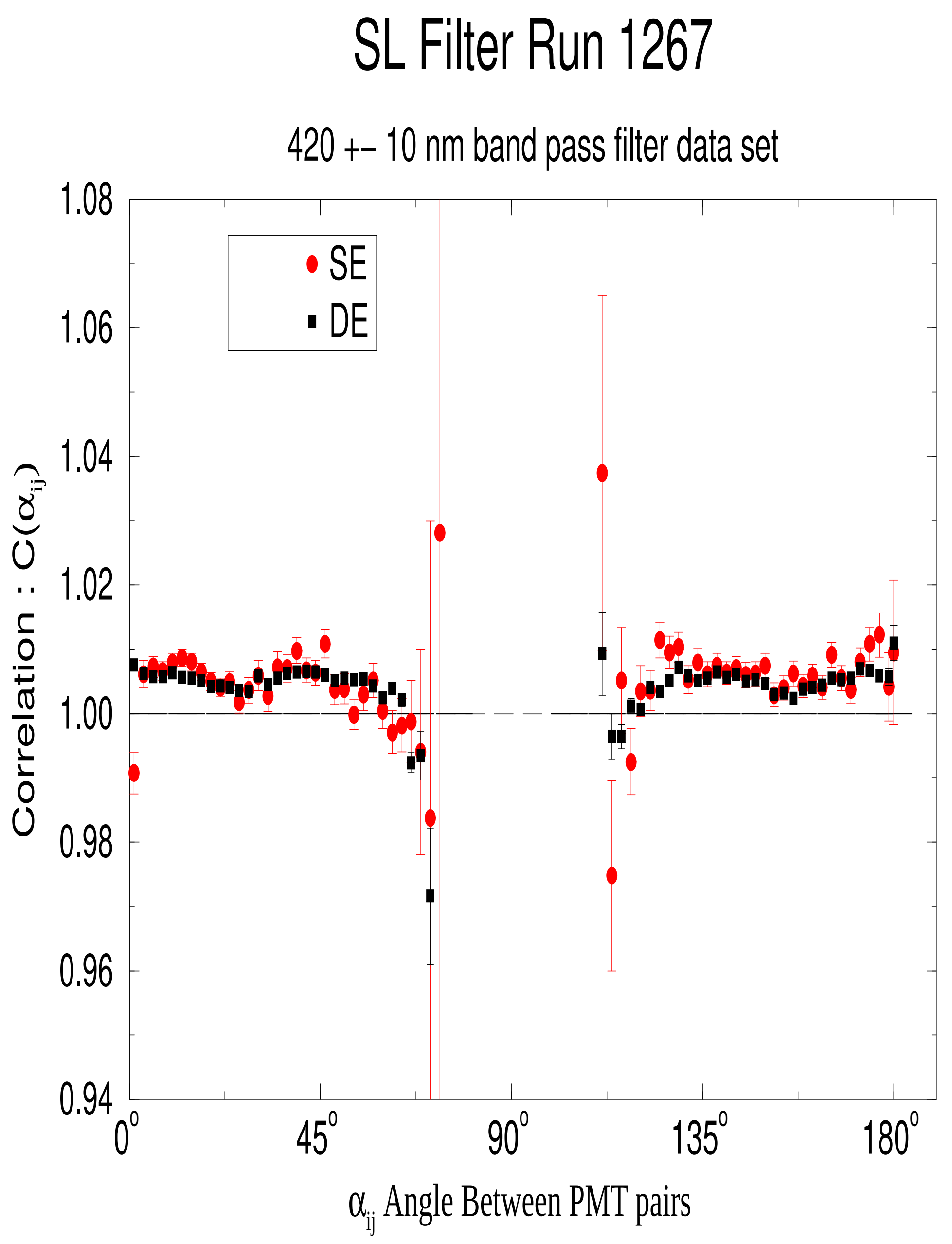


Figure 4.34: SE and DE vs. $\alpha$ for the 420±10 nm BP filter data set.

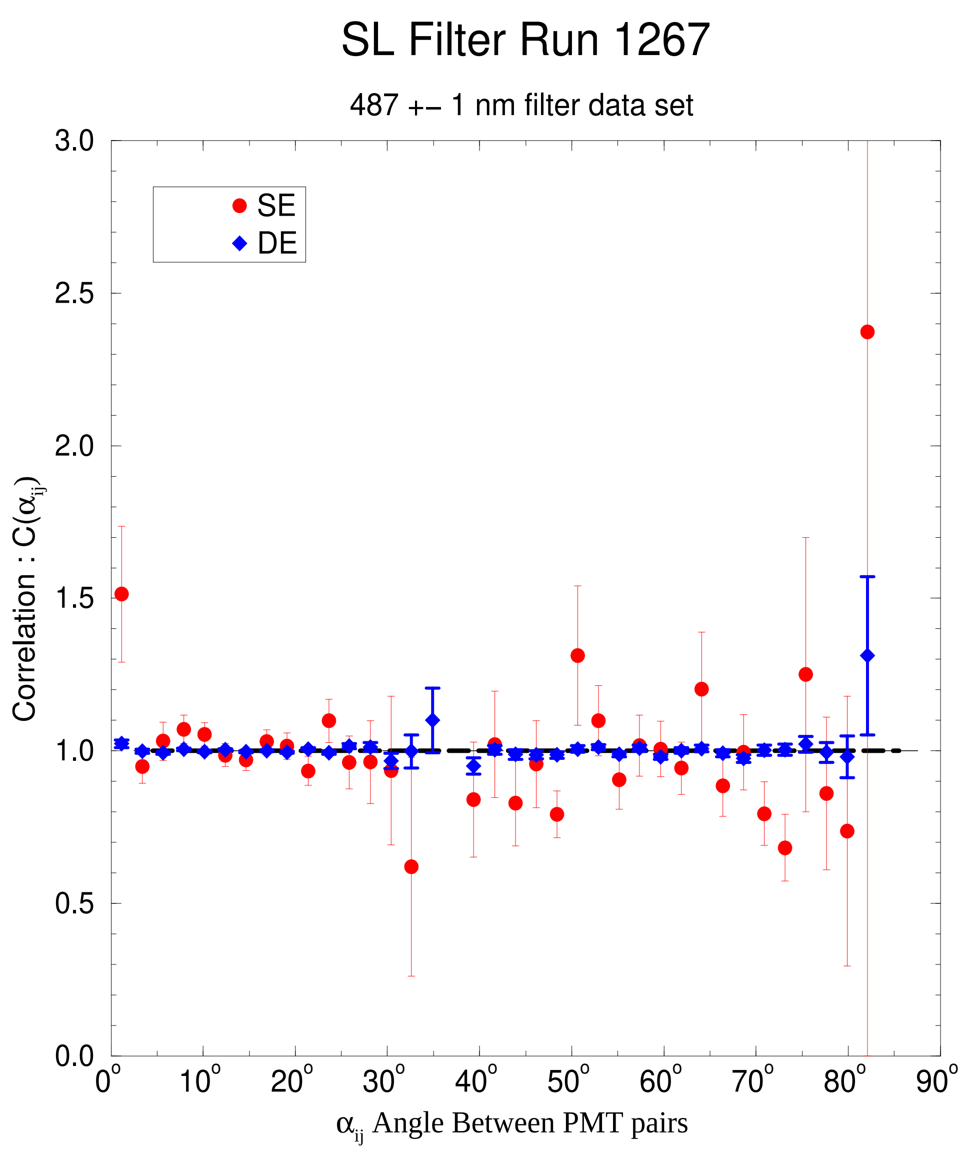


Figure 4.35: SE and DE vs. $\alpha$ for the 487±1 nm BP filter data set.

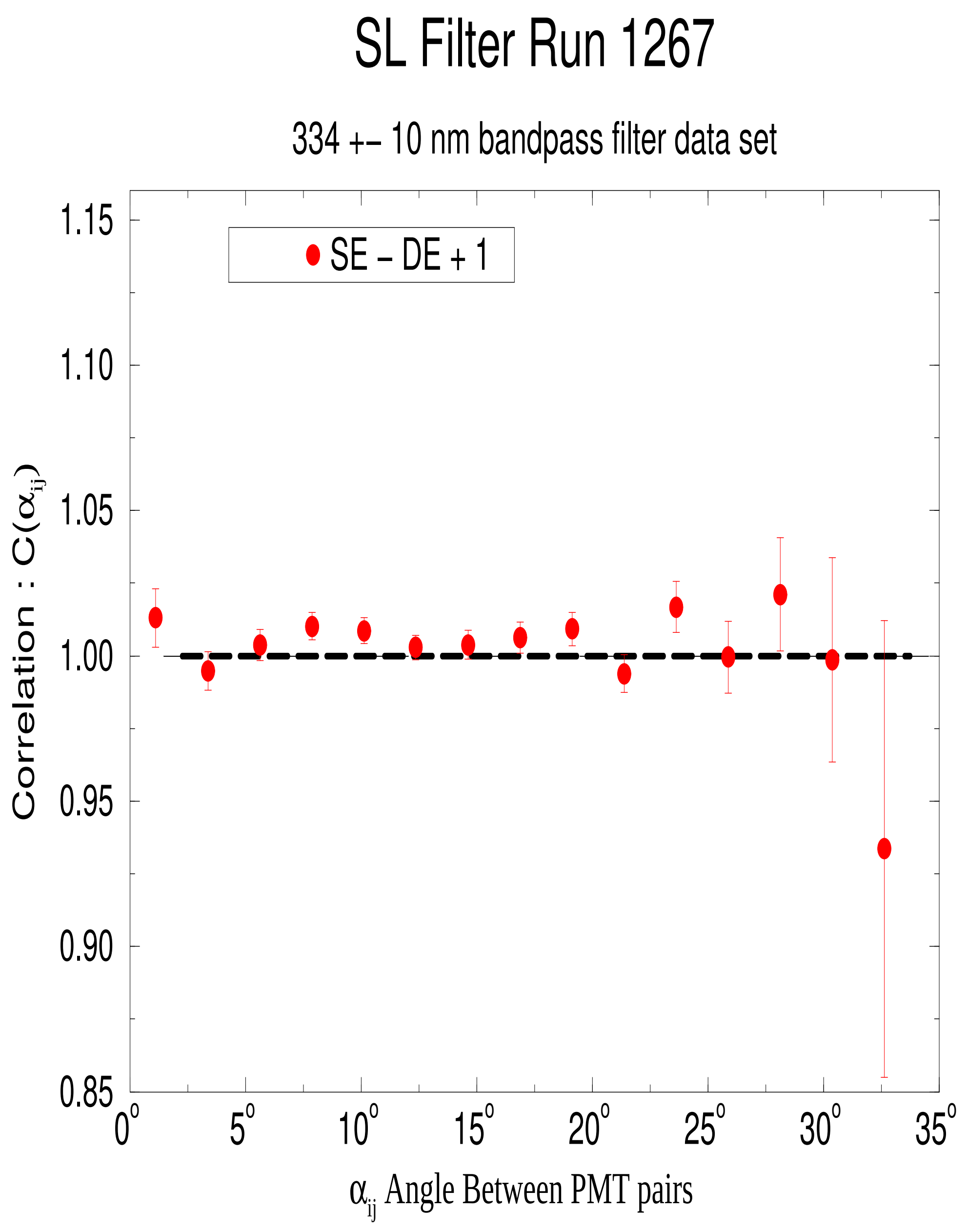


Figure 4.36: Corrected SE function vs. $\alpha$ for the 334±10 nm BP filter data set.

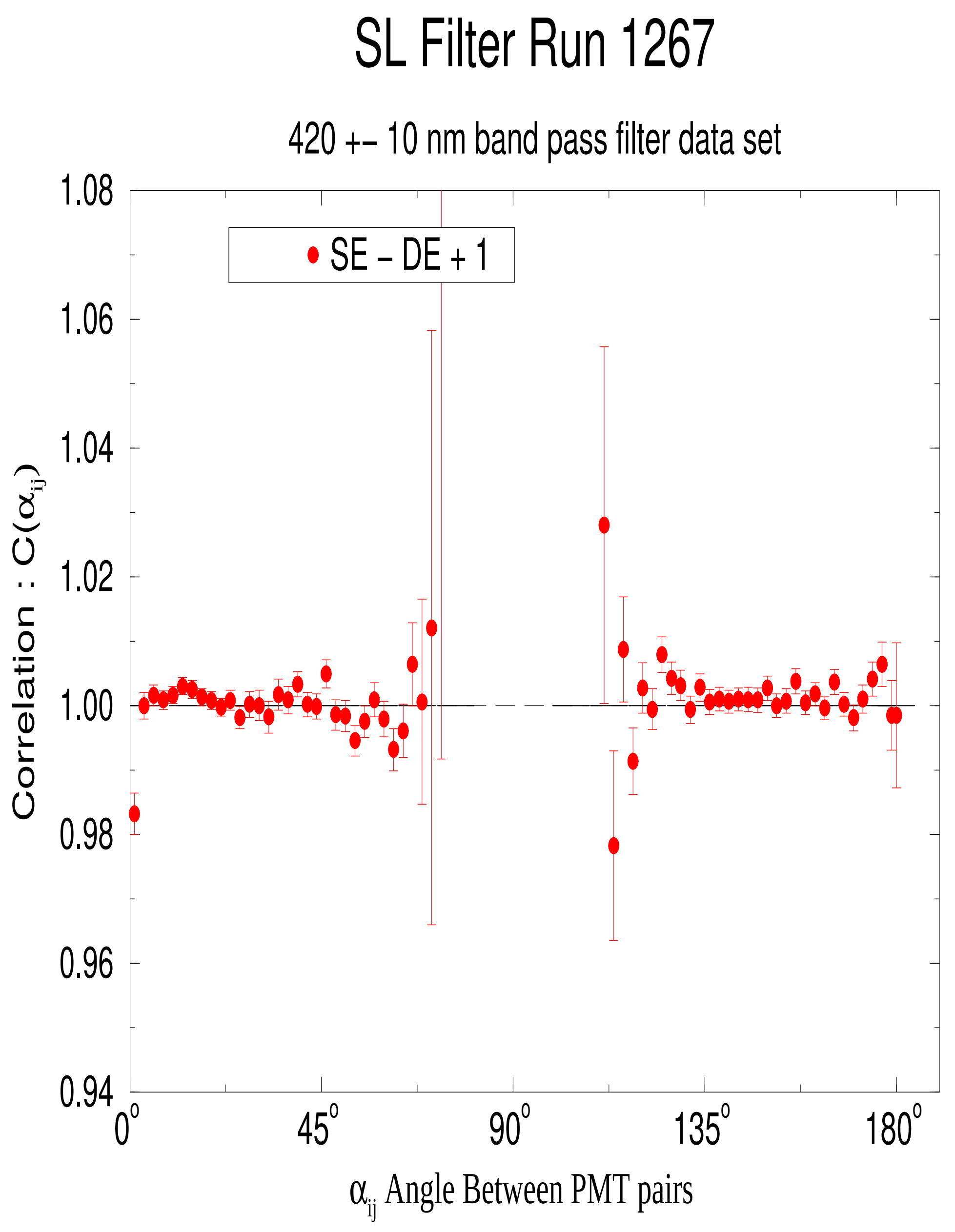


Figure 4.37: Corrected SE function vs. $\alpha$ for the 420±10 nm BP filter data set.

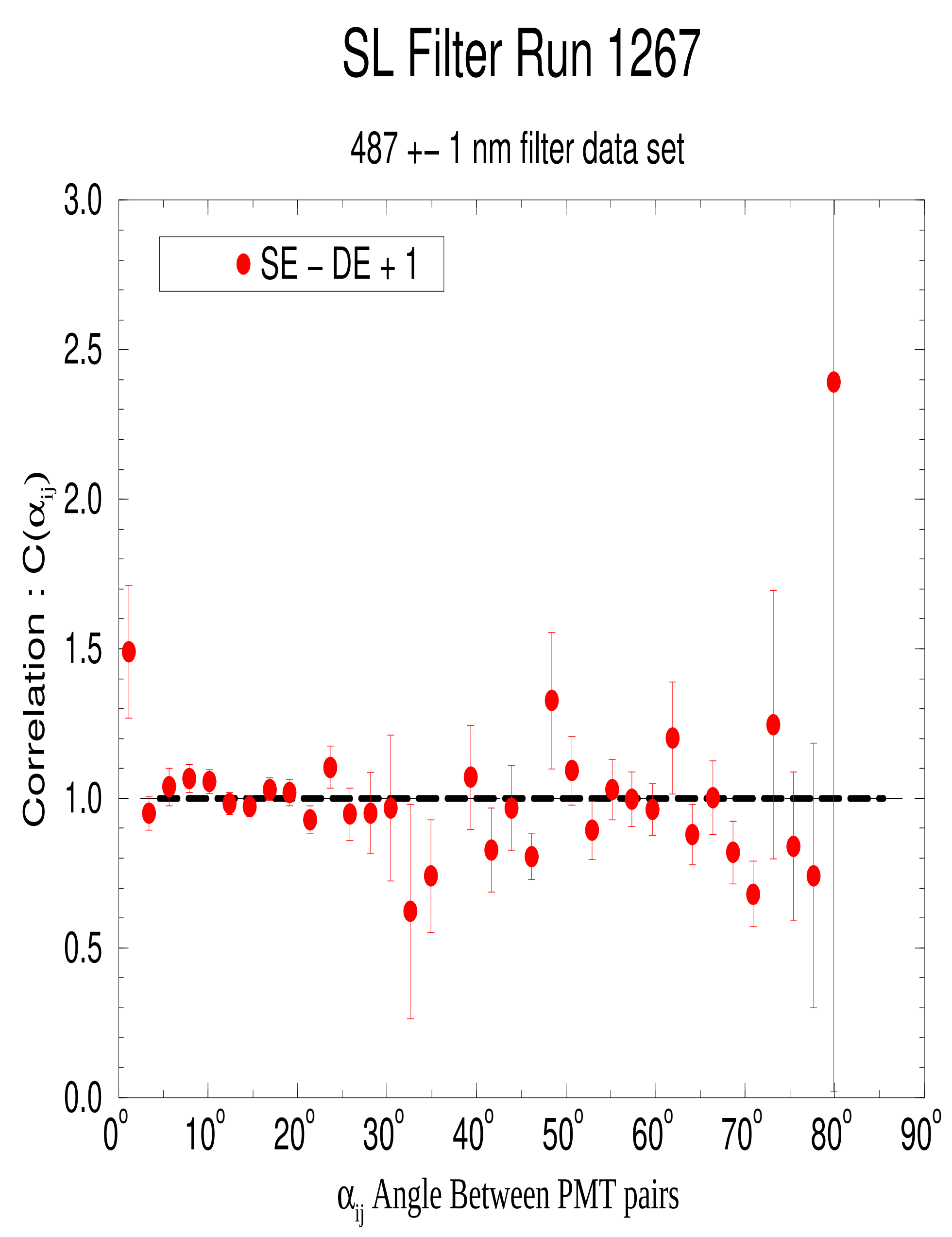


Figure 4.38: Corrected SE function vs. $\alpha$ for the 487$\pm$1 nm BP filter data set.

### Different Event (DE) Coincidences

One simple systematic check is the fact that in all of the data shown, the different events (DE) correlation functions are perfectly flat. On all plots the error bars are shown but are too small to be seen due to the excellent statistics.

### Comparison Between Different Filter Runs

A second filter run, run 1270, was performed a few hours after run 1267. In run 1270, the triggering was modified such that it was operating in "burst mode". Data were saved in groups of ten successive SL pulses with 1000 SL pulses in between the data groups being ignored. Otherwise, the run is exactly as run 1267 with the same filters and geometry.

Figure 4.39 shows a comparison of the SE correlation functions for the $420 \pm 10nm$ band pass filter data sets of runs 1267 and 1270. It is seen that the two data sets are consistent with each other. Only the first data points from each plot differ by a significant amount.

### Consistency Between Filters of the Same Type

Since three 420nm filters were used during the SL filter runs, the data from each filter can be analyzed separately to check for consistency between them. Each filter illuminates different sets of PMTs and may have slight manufacturer variations. It is

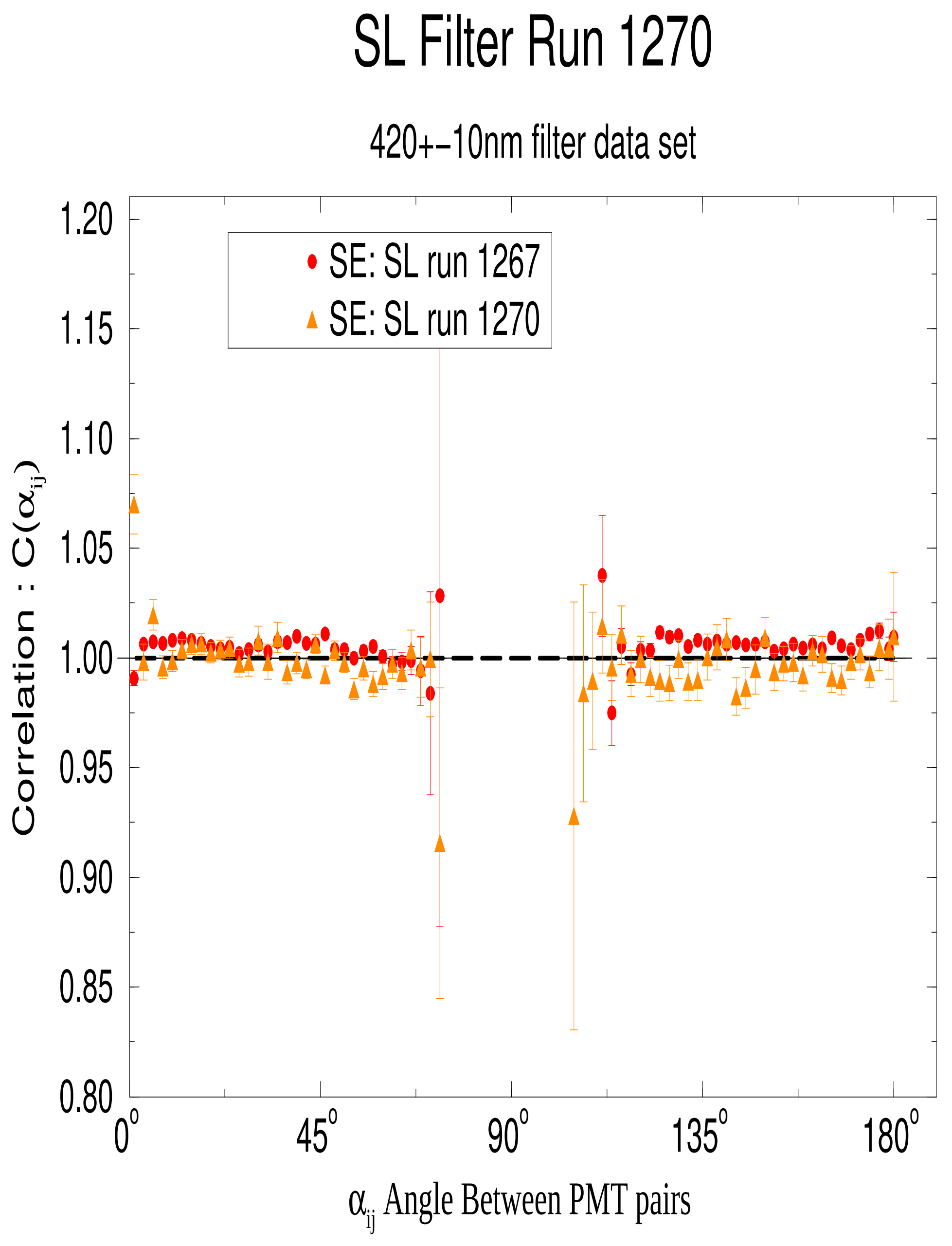


Figure 4.39: A comparison of the 420$\pm$10 nm data sets fromm SL filter runs 1267 and 1270. The SE correlation functions of the data sets from the two runs are consistent with each other.

important to show that such effects do not systematically change the results. Figure 4.40 show just such analyses for the PMTs illuminated by the three 420nm filters. It is seen that in the former plot, all three filters are totally consistent.

**Comparison Between Filters of Different Types**

Figure 4.41 shows the correlation functions for all three filter types plotted together. There does not appear to be a wavelength dependence to the correlation functions. All three filter types are consistent with uncorrelated data at all angles shown.

### 4.5.4 Quantitative Results For SL Intensity Interferometry

A fit to the data for the $420 \pm 10$ nm data set of run 1267 has been performed. The $1\sigma$ and $5\sigma$ uncertainty contours are shown in Figure 4.42 in the parameter space of the SL pulse width, $\tau_{SL}$, and the SL spot size, $R_{SL}$. The area below and to the left of the $5\sigma$ contour is excluded by the data. This exclusion is not competitive with other measurements of the SL pulse width [51, 52, 53] which has been well measured. The best fit SL spot size, or size of the light emitting region of the SL bubble, is approximately equal to the measured size of the SL bubble during light emission [49, 50]. However, we do not claim to have measured the two quantities. The only information of relevance from this plot is the exclusion region.

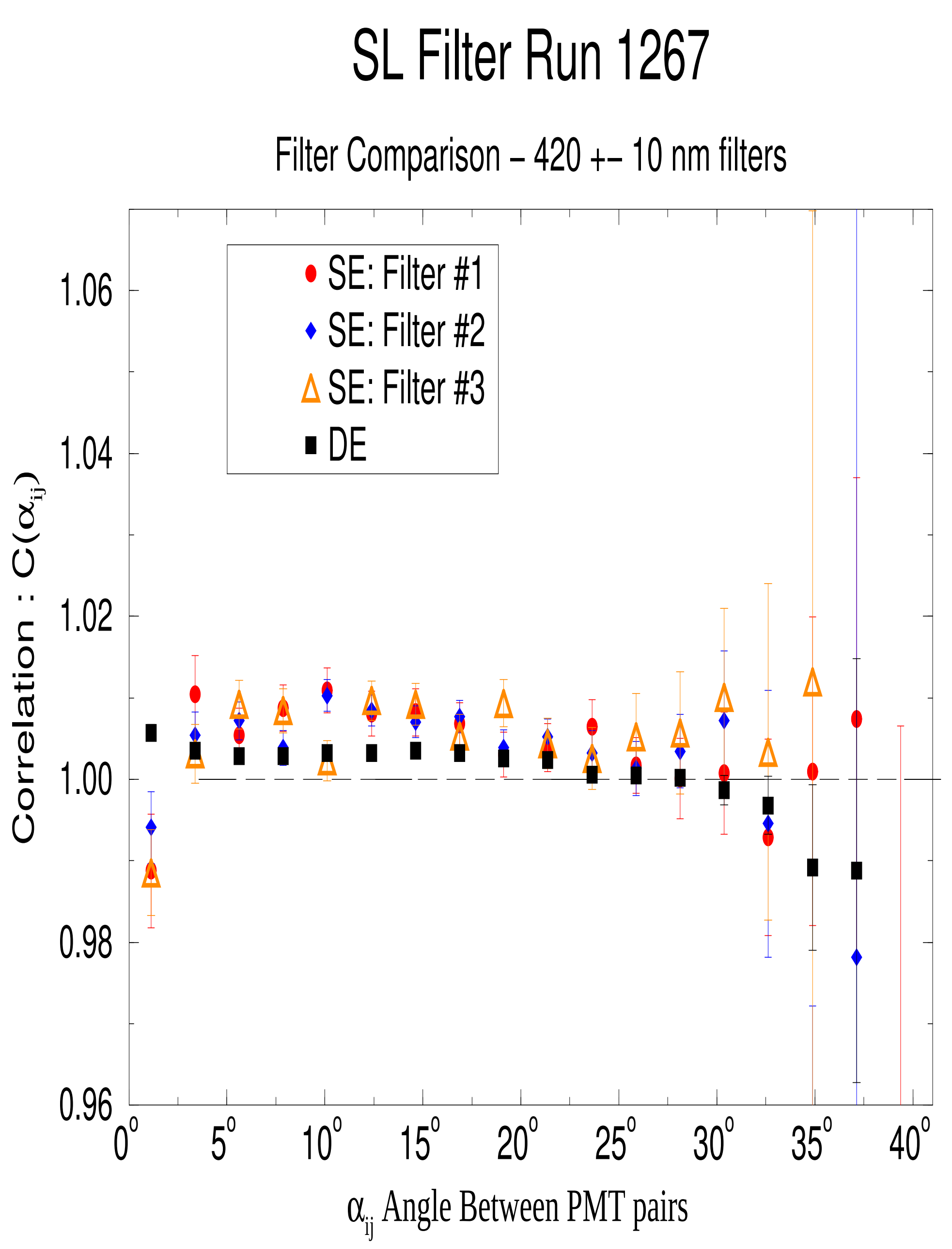


Figure 4.40: SL Filter Run 1267 - 420±10 nm filter comparison

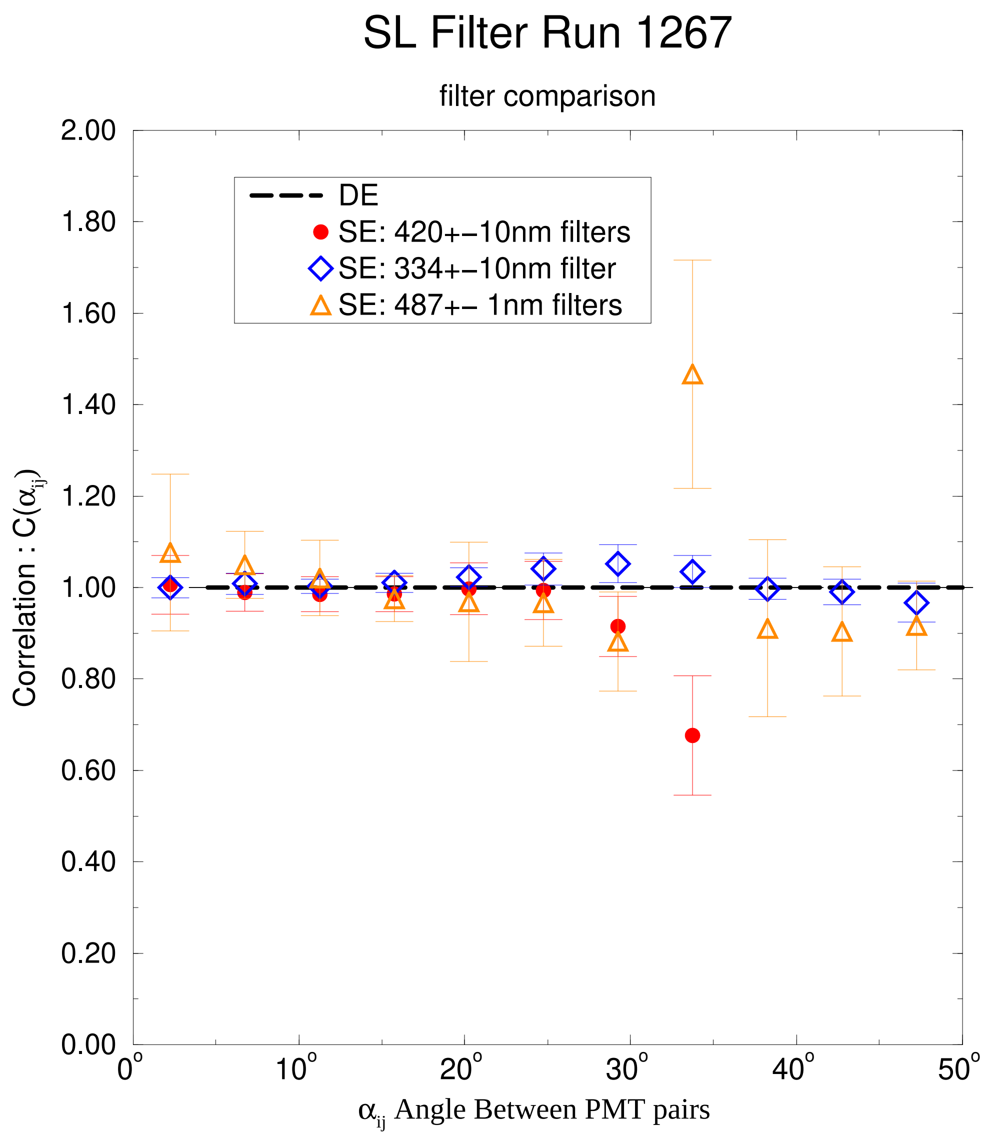


Figure 4.41: SL Filter Run 1267 - filter comparison

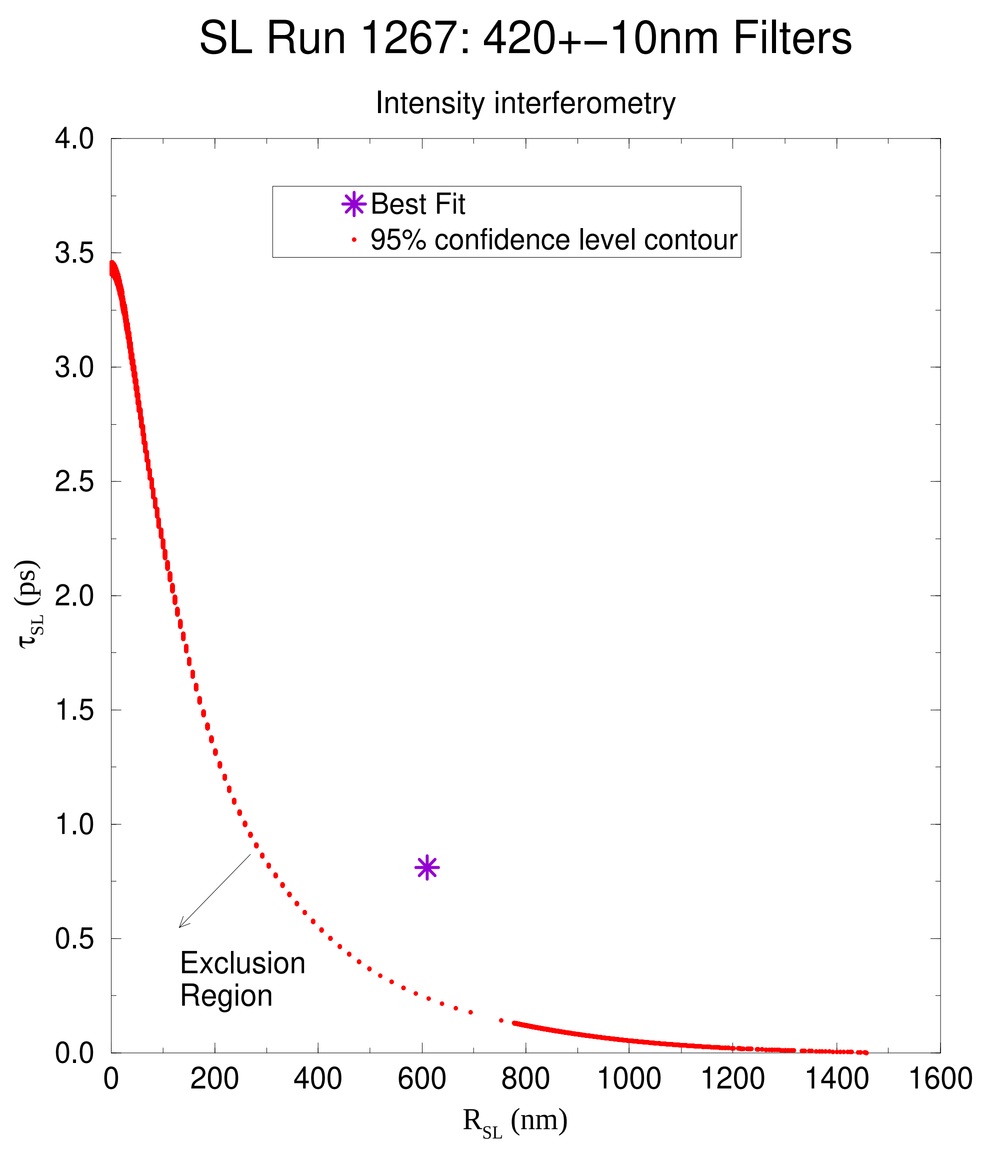


Figure 4.42: A fit to a theoretical model [2] of SL intensity interferometry has been performed on the $420 \pm 10$ nm band pass filter data set of SL run 1267. The best fit point is shown as an asterisk and the 95% confidence contour is shown. The contour excludes a region of small SL pulse width, $\tau_{SL}$ and spot size, $R_{SL}$.

### 4.6 Summary and Discussion of Results

Systematic effects due to the electronics and an effect with an unknown cause have been uncovered as a result of the analyses presented in this chapter. An efficient cut has been developed for the electronic crosstalk systematic which was used in the data presented here and can be used by SNO in future analyses. The crosstalk effect is small but does lead to false PMT hits. The second electronics systematic, a small anticorrelation between the charges on the same daughter card, has been shown to affect only the PMT charges and not the number of photons collected. By using "PMT hit" correlation functions rather than "charge" correlation functions, the systematic effect was eliminated from the data analyses presented above. This systematic will not affect solar neutrino analyses as they rely on the number of PMT hits and not the PMT charge. The positive correlation offset is due to fluctuations in the light intensity over time. The effect will not affect solar neutrino analyses.

An analysis of SL data in a search for back-to-back photon correlations was presented. The experiment was shown to be extremely sensitive to the effect. A null result has been observed. The data are consistent with no back-to-back correlations and the 95% confidence level upper limit for the percentage of correlated pair photons is 3.1% and 0.5% for unfiltered SL light and SL light at a wavelength of $\lambda = 420 \pm 10nm$ respectively. The latter result is more stringent and also more significant as theories which predict back-to-back photon correlations predict the photons will be correlated in energy.

A measurement of the SL photon angular distribution has been carried out. The analysis showed a complex, asymmetric correlation vs. angle. A fit for the dipole and quadrupole strengths showed significant measurements of those parameters but the fit is poor. The probability of getting a larger $\chi^2/DOF$ is less than 0.01%. We hypothesize that complex bubble motions lead to very small multipole contributions to the angular distribution. Similar effects have been shown to be dependent on experimental conditions by others [1, 50]. The experiments carried out here are more sensitive to the effects but the results do not give physical insight into the SL mechanism.

Intensity interferometry was used in an attempt to measure the SL spot size. A null result was observed. No angular correlations were seen at $\lambda = 334 \pm 10nm$, $\lambda = 420 \pm 10nm$ and $\lambda = 487 \pm 1nm$. Thus it was not possible to measure the spot size. However, a fit to the $420 \pm 10nm$ bandpass filter data set, yields a small excluded region at the 95% confidence level. These results are consistent with other measurements [51, 52, 50] but the limitations on the SL pulse width, $\tau_{SL}$ and spot size, $R_{SL}$ from the previous measurements in the literature are not improved by the results presented here.

A summary of the experimental results will be presented in chapter 5.

# Chapter 5

# Conclusions

## 5.1 Sonoluminescence Studies of the SNO Detector

The motivation for the Sudbury Neutrino Observatory (SNO) has been presented. SNO may provide direct evidence of neutrino oscillations in the solar neutrino sector explaining the deficit of solar neutrinos observed at earth compared to predictions from standard solar models. This is possible due to the use of heavy water as a target and detection medium. Calibrating and understanding the SNO detector is crucial to the analysis of solar neutrino data. Due to construction delays, it was not possible for the author to study solar neutrinos as part of this thesis. Instead, two sonoluminescence (SL) sources were developed to use as calibration sources for the SNO detector. The "water fill" source is designed to be used when the detector is full of heavy and light water. This source has not been used due to time constraints but is ready to be used in the future. All experiments undertaken for this thesis used the "air fill" SL source.

This SL source has been used to perform measurements of the time response of the SNO detector photomultiplier tubes (PMTs). The uncertainty on the timing of light from the SL source, corrected for known photon path lengths from a reconstructed source vertex, is measured to be $1.6ns$, the time resolution of the PMTs. This result is equivalent to the PMT transit time spread obtained from the PMT manufacturer. Thus the SL source shows the PMT response to delta function light signals. This is due to the short pulse width of SL ($30 - 300ps$ [51, 52, 53]), compared to the PMT response time of a $\sim 5ns$. The same measurement has been carried out using the standard SNO optical calibration source, a nitrogen laser and diffuser ball system. When measured with this "laserball" (LB), the uncertainty in the timing is $2.0ns$ or 25% larger than the value obtained with the SL source.

During the course of analyzing SL and LB data of experiments carried out for this thesis, two systematic effects in the SNO electronics were observed. The first is crosstalk between adjacent electronics channels, which occurs with a probability of approximately 2.5% times the probability of adjacent electronics channel photon coincidences when the charge in a given PMT is greater than $\sim 5$ photoelectrons. This effect is not unexpected at such low levels. An efficient cut has been developed which eliminates much of this background. Without the cut, the crosstalk background will slightly bias solar neutrino analyses as it falsely increases the observed number of photons in a given event. The upper limit on the lost signal due to the cut is $< 0.4\%$

of the adjacent electronics channel coincidence probability.

The second systematic effect is a slight anticorrelation of the charge measurements for electronics channels on the same SNOINT integrator chip and a slightly smaller anticorrelation for channels on adjacent SNOINT chips on the same daughter card. This effect has been shown not to decrease the number of photons detected, but only affects the charge in some unknown way. Thus it will not bias solar neutrino analyses.

## 5.2 Fundamental SL Investigations

Three separate experiments were undertaken to study fundamental properties of sonoluminescence using the SNO detector. These are: 1) back-to-back photon correlations, 2) the angular distribution of SL photons, and 3) an attempt to measure the SL spot size.

### Back-To-Back Photon Correlations

Two sets of data were taken to study back-to-back photon correlations. The first, and less sensitive, used unfiltered SL light. The more sensitive data set used $420 \pm 10nm$ band pass filters attached to the exterior of the SL source to attempt a measurement of back-to-back correlations over a narrow band of wavelengths. No evidence for back-to-back photon correlations is seen in either data set. The 95% confidence level upper limits on the strength of back-to-back photon correlations are 3.1% for unfiltered SL light and 0.5% for SL light in the wavelength range $420 \pm 10nm$. This can be interpreted as limits on the percentage of photon pairs which have back-to-back correlations.

### Angular Distribution of SL Photons

The SL photon angular distribution has been measured using angular correlation functions. Attempts to fit the data to distributions with: 1) a small dipole component, and 2) a coherent sum of a dipole and a quadrupole, give poor fits. The best fit yields dipole and quadrupole strengths of $1.80 \pm 0.14\%$ and $0.16 \pm 0.03\%$ respectively. The angular distribution may be due to complex bubble motions rather than motions of charges in the bubble interior.

### SL Intensity Interferometry

Intensity interferometry, the method of Hanbury Brown and Twiss, has been used to attempt a measurement of the size of the light emitting region of a SL bubble. No angular correlations were observed at three different wavelengths ($\lambda = 334$, 420 and $487nm$) so the measurement was not possible. The best fit to the data gives a SL pulse width of $\tau_{SL} = 0.8ps$ and a spot size of $R_{SL} = 610nm$. The former result is inconsistent with previous measurements [51, 52, 53] of the SL pulse width. The latter result is consistent with previous measurements of the SL bubble size during light emission [49, 50]. A small region of parameter space is excluded at the 95%

confidence level. No new limitations on the SL pulse width and SL spot size are obtained from this analysis. The experimental technique is unproven by this work.

### 5.3 Future Work and Experiments

Improvements that can be made to the experimental setup are:

(1) A means of monitoring the partial pressure of air in the water is needed as the intensity and stability of SL light has been shown to depend sensitively on this quantity [56, 50].

(2) A separate filament with a DC current can be used to heat the water. Increasing the water temperature decreases the intensity of the light which is necessary for some applications.

(3) A means of remotely degassing the source is necessary as the source will be stored inside the cover gas glove box. The umbilical for the source has a tube in it for this purpose. A means of connecting it to the source and external pump must be devised.

The high repetition rate of the SL source can be exploited to test the response of the SNO detector to high data rates. This was done on a preliminary basis by the author, but should be performed again because the data acquisition system has since been improved. At issue is the readiness of the electronics and data acquisition systems in the event of a nearby supernova.

Of the three fundamental SL studies performed as part of this thesis, only the angular distribution measurement should be attempted again in the SNO detector. The SNO detector is ideal for such a measurement. With the improvement in the experimental apparatus described above, careful experiments can be done over a wide range of parameter space and experimental conditions. Examples are measuring the angular distribution:

(1) as a function of the partial pressure of air in the water of the SL source,

(2) as a function of the intensity of the light,

(3) as a function of the stability of the SL light,

(4) for single events,

(5) changes from pulse-to-pulse.

Back-to-back photon correlation and intensity interferometry experiments can best be done in small laboratories where more control over the equipment and data taking time is possible.

# Appendix A

# SNO Neutrino Physics

## A.1 Scientific Motivation

Chapter 1 discussed the Solar Neutrino Problem and five major neutrino experiments. The experiments were compared and their merits and shortcomings were specified. A shortcoming that all of the six experiments share is that none can provide information on the contribution to the solar neutrino flux from $\nu_\mu$or $\nu_\tau$. The concept of neutrino oscillations was shown to lead to contributions from one or more of $\nu_\mu$, $\nu_\tau$or $\nu_s$.

SNO is designed to measure both the total flux of $^8$B neutrinos emitted by the sun, and at the same time, to measure the flux of $^8$B electron neutrinos. This is possible through the use of heavy water ($D_2O$) as opposed to light water ($H_2O$). SNO is the first (and only as of this writing) *heavy* water Cerenkov detector. The reasons for using heavy water are several:

(1) there is a Charged Current (CC) interaction of $\nu_e$with the deuteron which preserves the flavor of the incident neutrino: $\nu_e + d \longrightarrow p + p + e^-$,

(2) there is a separate, Neutral Current (NC), interaction of $\nu_e$, $\nu_\mu$and $\nu_\tau$which disintegrates the deuteron and has the same cross section for each neutrino flavor: $\nu_x+d \longrightarrow n+p+\nu_x$,

(3) the CC and NC interactions can be separated on a statistical basis,

(4) both the CC and NC cross sections are relatively large.

The idea that the NC signal from a heavy water solar neutrino experiment would measure the full (high energy) solar neutrino flux was put forward by the late Herb Chen in an important paper [84].

$D_2O$ is very expensive and not readily available in large quantities. The Canadian government does have large quantities available. It is used to cool the Canadian deuterium-uranium (CANDU) fission reactors. AECL Canada loaned SNO one kilotonne of $D_2O$ for the experiment, an amount worth $\sim$ 300 million Canadian dollars. The availability of the heavy water, and the necessity of operating in a deep mine made Canada the unique site for the experiment.

SNO will measure the $\nu_e$flux from the CC interactions and the total neutrino flux, the flux from the sum of the $\nu_e$, $\nu_\mu$and $\nu_\tau$components, via the NC interactions. The latter measurement is a measurement of the total $^8$B solar neutrino flux. This will be the first such measurement if active species solar neutrino oscillations do in fact occur. To determine the important issue of neutrino oscillations, the ratio of the CC and NC flux measurements (CC/NC) can be calculated from the SNO results.

If that ratio is 1 then either all of the neutrinos are of the electron type or some electron neutrinos have oscillated into sterile neutrinos, $\nu_s$. If the ratio is less than 1, then some of the $\nu_e$have oscillated into $\nu_\mu$or $\nu_\tau$providing direct evidence of neutrino oscillations in the solar neutrino sector. The CC/NC ratio is independent of solar models and its theoretical uncertainties.

SNO has greater physics potential than stated above. Section A.5 will delve into this topic but first the neutrino interactions in the SNO detector and their backgrounds are discussed.

## A.2 Neutrino Interactions In SNO

The possible interactions in SNO are listed in table A.1 along with the interesting physics of each. The interactions are described individually.

### A.2.1 CC Interaction

In the CC interaction (reaction #1 in table A.1) the incoming $\nu_e$interacts with a deuteron in the heavy water producing an electron. The electron's energy is strongly correlated with the neutrino energy. The energy response of electrons to 5 MeV neutrinos is shown in Figure A.1 which was generated using Monte Carlo. By analyzing events which were caused by the CC interaction, the solar $\nu_e$flux and energy spectrum can be obtained.

| # | Interaction | Crs sctn | Physics |
|---|---|---|---|
| 1 | CC: $\nu_e$+ d $\longrightarrow$ p + p + e$^-$ | 2x10$^{-42}cm^2$ | Solar $\nu_e$flux & spectrum |
| 2 | NC: $\nu_x$+ d $\longrightarrow$ p + n + $\nu_x$ | 6x10$^{-43}cm^2$ | Solar total $\nu$ flux |
| 3a | ES (CC): $\nu_e$+ e$^-$ $\longrightarrow$ $\nu_e$+ e$^-$ | 6x10$^{-44}cm^2$ | Solar $\nu$ consistency check |
| 3b | ES (NC): $\nu_x$+ e$^-$ $\longrightarrow$ $\nu_x$+ e$^-$ | 9x10$^{-45}cm^2$ | with CC, NC |
| 4 | ($\overline{\nu_e}$ -d): $\overline{\nu_e}$ + d $\longrightarrow$ n + n + e$^+$ | 7x10$^{-43}cm^2$ | supernovae, reactor $\overline{\nu_e}$ |
| 5 | ($\overline{\nu_e}$ -p): $\overline{\nu_e}$ + p $\longrightarrow$ n + e$^+$ | 4x10$^{-42}cm^2$ | supernovae, reactor $\overline{\nu_e}$ |

Table A.1: SNO neutrino interactions and physics. The cross sections at 10 MeV neutrino energy are given.

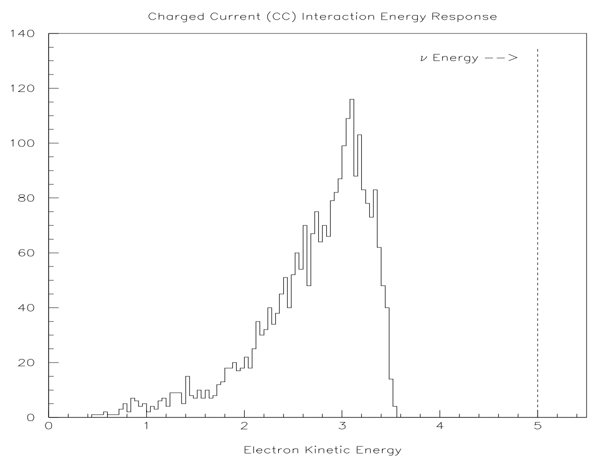


Figure A.1: Energy response of the SNO detector to 5 MeV neutrinos with the CC interaction. The figure was obtained using the SNOMAN Monte Carlo generator.

The electron produced in the CC interaction has a definite angular correlation with the neutrino direction. The angular distribution of the electron daughter is $C(\theta) = 1 - \frac{1}{3}\cos\theta$ where $\theta$ is the angle between the neutrino and electron directions. Here, $\beta$, is the velocity of the neutrino compared to that of light in a vacuum. One can use the energy and angular information to separate the CC events from events in the data set produced by other reactions.

SNO expects 42 CC events per day assuming the Bahcall-Pinnsonault Solar model of 1995 (with $He$ diffusion). For the small angle MSW solution, stated in chapter 1, (and the same SSM) the CC rate is 13 per day.

### A.2.2 NC Interaction

The NC interaction (reaction #2 in table A.1) distinguishes SNO from the five other major neutrino experiments. A neutrino of any flavor collides with and breaks up the deuteron. The deuteron has a binding energy of 2.2 MeV, the minimum energy required by a neutrino to induce this interaction. None of the final state particles produce Cerenkov light. The neutron thermalizes and is captured by a nucleus which emits one or more $\gamma$ after a short delay. The $\gamma$ then (most likely) Compton scatters off electrons; some of these electrons have enough energy to produce Cerenkov radiation which is detected by the PMTs. There is no way to obtain the incoming neutrino energy distribution and there is no angular correlation of the Cerenkov radiation direction with the direction of the incoming neutrino.

If the neutron is captured by a deuteron, it produces tritium. The tritium nucleus emits a single 6.25 MeV $\gamma$ . A $\gamma$ of this energy will produce, on average, approximately 20% fewer Cerenkov photons than an electron of the same energy. This number is obtained from the well tested and understood Electron Gamma Shower ("EGS4") [85, 68]. See Section 2.8 for a discussion of this calibration.

If the neutron is captured by hydrogen, a 2.2 MeV $\gamma$ results. If the $\gamma$ could give all its energy to the Compton electron, the electron would not produce enough Cerenkov photons to be detected above the detection threshold of the SNO detector, even if that threshold were as low as 2 MeV. Thus neutron captures on $H$ decrease the NC detection efficiency. The cross section for neutron capture on $H$ is a factor of 638 larger than capture on $D$ [86]. For an isotopic purity of 99.85%, the neutron capture probability on $H$ and $D$ in the $D_2O$ are equal. The $D_2O$ used in SNO is kept at a purity higher than this lower limit.

Neutrons that capture on Oxygen result in a low energy $\gamma$ , also decreasing the NC efficiency. The neutron capture cross section for $^{16}O$ is down by a factor of $\sim 2.5$ from that of the deuteron [86]. There are twice as many deuterons per molecule of heavy water as there are oxygen nuclei leading to a deuteron-to-oxygen neutron capture probability ratio of 5.

The neutron mean free path in pure $D_2O$ is large enough that many of the neutrons escape the heavy water before being captured. There are two ways to enhance the capture probability of neutrons. One is by doping the $D_2O$ with Chlorine in the form of $MgCl_2$ salt and the other is through the use of $^3He$ proportional counter neutral current detectors (NCDs). In these modes of operation the NC signal is enhanced to improve the measurement of the total neutrino flux independent of neutrino flavor. These two methods are described below.

### Adding $MgCl_2$ Salt

The neutron capture cross section on $^{35}Cl$ is a factor of $8.3\times10^5$ larger than that of the deuteron and a factor of $1.3\times10^3$ larger than that of hydrogen. Adding small amounts of $^{35}Cl$ in $MgCl_2$ salt to the heavy water has two advantages. First, the larger cross section dramatically reduces the number of neutrons that capture on the hydrogen impurities in the $D_2O$ and that escape the $D_2O$ before being captured. Second, the $Cl$ emits one or more gamma rays with a total energy of 8.6 MeV. The total $\gamma$ energy is 30% larger than the $\gamma$ from neutron capture on the deuteron, resulting in more Cerenkov light being emitted. Thus both the efficiency for neutron capture and the efficiency for detection of the resultant Cerenkov light increase.

The disadvantage of the salt option is that the radial dependence of the neutron capture gammas for pure $D_2O$ can be used to separate CC and NC events, without the need for discriminating electrons from gammas. This advantage is lost with salt

+ $D_2O$ as the radial dependence is then quite similar to the CC radial dependence.

The heavy water system has been designed to permit salt doping as discussed below in Section 2.5.2.

**Neutral Current Detectors**

SNO will deploy a Neutral Current Detector (NCD) array into the volume of the heavy water at some time during the operation. This array is made up of $\sim 100$, 5cm diameter proportional counters with a total length of $\sim 800m$. The counters are filled with $^3He$ which has a large $(n,p)$ cross section, $\sim 10^7$ times the neutron capture cross section of the deuteron and a factor of 12 larger than that of $^{35}Cl$ [86]. The neutrons capture reaction is:

$$n +^3 He \longrightarrow p + t. \tag{A.1}$$

The NCDs will be laid out on a lattice with 1m separation yielding a neutron capture efficiency of 45%. This configuration is optimized to balance the desire for large neutron capture probability with the need to minimize the decrease of Cerenkov light detection efficiency for the CC interactions due to the presence of the NCDs. Comparisons of the mean neutron mean free path and lifetime are 1.1 m and 16 ms for the NCDs and 48 cm and 4 ms for the salt additive at a concentration of 0.2%.

Extreme care has been taken to use clean room methods and low radioactivity materials in the fabrication of the NCDs. Cosmogenic radioactivity in the materials of the NCDs requires that they be taken underground long before deployment so the cosmogenic radiation can decay away. The NCDs will be deployable early in the year 2000.

#### Comparison of the Three NC Measurement Methods

SNO expects 16 NC interactions per day assuming the neutrino fluxes calculated in the BP SSM of 1998 [17]. The fraction detected depends on the method used and its efficiency. For 99.85% isotopically pure $D_2O$ , 50% of the neutrons escape the heavy water and 25% each capture on hydrogen and deuterium. As stated above, only the latter have sufficient energy to generate enough Cerenkov light to be detected. The number of detected Cerenkov photons from the 6.25 MeV neutron capture gamma has a broad distribution and the detection efficiency depends on the energy threshold of the detector which is not yet known. The total NC detection efficiency is therefore less than 25%.

When adding salt at a concentration of 0.2%, the number of neutrons that escape the AV is reduced to 10%. The capture probabilities are 84%, 3% and 3% for $Cl$, $H$ and $D$ respectively. These numbers also assume a $D_2O$ purity of 99.85%. The efficiency for detection of the Cerenkov light also increases so the total NC efficiency is more than 84%/25% $\sim$ 3.3 times larger than the pure $D_2O$ case.

The NCD array has a neutron capture probability of 45% in pure $D_2O$ . The efficiency of the proportional counters themselves has yet to be determined but should be substantially better than the efficiency for detection of Cerenkov light from the other two processes. Thus the salt and NCD configurations have higher overall NC detection efficiencies compared to the pure $D_2O$ one. NC measurements from all three configurations will provide redundancy and consistency checks on the NC flux measurement with different systematic errors.

### A.2.3 ES Interactions

The elastic scattering (ES) reactions, reactions 3a and 3b in table A.1, are experimentally indistinguishable. Elastic scattering of $\nu_e$has both CC and NC contributions, while elastic scattering of $\nu_\mu$and $\nu_\tau$is purely a NC process. The cross section of the $\nu_e$reaction is roughly a factor of 7 larger than that of the $\nu_\mu$, $\nu_\tau$reaction and this relation is approximately independent of neutrino energy. The energy distribution of the scattered electrons is close to flat from the Cerenkov threshold energy to the the neutrino energy where it drops to zero. This is shown in Figure A.2 which is obtained from Monte Carlo simulations of elastic scattering in the SNO detector. The lower cutoff in the figure is an enforced Monte Carlo cutoff to save computing time. The energy information is not as good as for the CC interaction but distortions in the neutrino energy distribution can be determined with careful analysis. This has been studied by Kamiokande and Superkamiokande as the ES interaction is the sole inter-

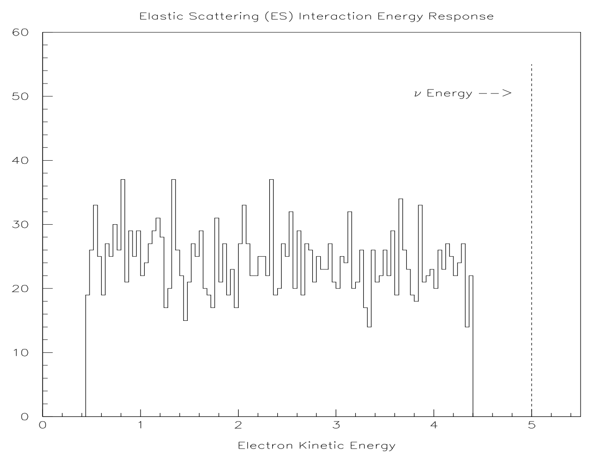


Figure A.2: Energy response of the SNO detector to 5 MeV neutrinos with the ES interaction in the heavy water. The figure was obtained using the SNOMAN Monte Carlo generator.

action to which those experiments are sensitive. It has already been noted that the electron from this reaction is highly correlated with the incoming neutrino direction so the source of the neutrinos can be determined.

### A.2.4 $\overline{\nu_e}$ Interactions

SNO can also detect $\overline{\nu_e}$ from supernovae and other possible astrophysical sources via reactions 4 and 5 from table A.1: inverse $\beta$-decays of the deuteron and proton respectively. These $\overline{\nu_e}$ interactions both have relatively large cross sections. The kinematics of these interactions are similar to that of the CC interaction (reaction 1 in table A.1) but the Q-value for the positron energy is $-4.03 MeV$ for reaction

4 and $-1.8 MeV$ for reaction 5. The positron energy is strongly correlated with the incoming neutrino energy. Both reactions will yield a Cerenkov event from the positron. Additionally, since reaction 4 occurs in the $D_2O$ , it can yield one or possibly two neutron capture events in delayed coincidence with the first depending on the NC efficiency. The neutron from reaction 5 will generally be captured on hydrogen in the $H_2O$ and go undetected. Occasionally the neutron is captured by a deuteron in the $D_2O$ and some fraction of those will result in a detected Cerenkov event. The positron angular distribution is almost isotropic with respect to the incoming neutrino direction in both reactions.

### A.3 Distinguishing The Interactions

Distinguishing between the different interactions is important. Except in the case of the NCDs, the final product of every one of the five interactions is a Cerenkov electron (or positron) which creates detectable light. How can the different interactions be distinguished?

All of the separation schemes are statistically based. The schemes are developed using MC simulations of the two interactions and take advantage of geometrical differences in their behavior. One of the schemes uses neural networks that have been trained using Monte Carlo CC and NC events [87].

ES events can look like CC or NC events but the interaction rate is less for the former due to its smaller cross section. CC, NC and ES events can be distinguished by knowledge of the observed energy and angular distributions. As stated in Section A.2, the angular distribution is flat for NC events, but has well defined different shapes for CC and ES events.

A $\overline{\nu_e}$ interaction will most probably lead to only one Cerenkov event, even if they occur in the $D_2O$ . These events will then look exactly like CC events. However, at solar neutrino energies, it is expected that there will be no flux of $\overline{\nu_e}$ unless a supernova occurs. Supernovae neutrinos arrive in bursts over a time period of a few seconds. There is essentially no solar neutrino "background" during this time. Since no directional information exists for $\overline{\nu_e}$ interactions, the angular distribution cannot be used to distinguish them from NC events, but that can be done for CC and ES on a statistical basis.

### A.4 Sources of Background

SNO has some significant sources of background that have to be carefully understood. The most significant backgrounds to the CC and NC interactions are described individually below. Backgrounds to the ES events are the same as for CC events. In the discussion of the detector components and systems in chapter 2 (see Sections 2.1 to 2.9), it is described how these backgrounds are minimized and measured.

### A.4.1 Backgrounds To CC Events

Beta and gamma rays from radioactive isotopes in or near the detector will be backgrounds to the CC interaction if they are detectable. The most significant of these are gammas from the cavity wall surrounding the detector and beta-gammas from the PMTs and other detector materials.

#### Cavity Gammas

The rock walls of the cavity contain radioactive nuclei which can emit radiation in the form of betas and gammas. The majority of betas will stop a few cm from the cavity wall. The gammas have a mean free path in water of 20-30cm. A small number of them can travel the 5 mean free path lengths or longer and get inside the PSUP to be detected. The precautions taken to minimize this background are described in Section 2.1.

#### PMT and Internal Beta-Gammas

The most significant background at the lowest energies, are the PMT $\beta - \gamma$ events. These come from radioisotopes in the PMT glass and housing. The only way to reduce this background is to carefully choose the materials - and this was done. However, even with the best materials, the problem is not eliminated. The majority of PMT beta gamma events will reconstruct outside the acrylic vessel and thus not be confused with events from $\beta - \gamma$ in the $D_2O$ (internal) that mostly reconstruct inside the $D_2O$ volume. Reconstruction cuts should be enough to control this source of background. It is expected that this background will not be dominant near the energy threshold. Instead, $\beta - \gamma$ events from the water and materials making up the detector will dominate [81].

### A.4.2 Backgrounds To NC Events

#### Photodisintegration of the deuteron

A $\gamma$ with an energy above 2.2 MeV, the NC interaction threshold, can photodisintegrate the deuteron and mimic a NC event. If this $\gamma$ comes from a NC event itself, and the neutron from the photodisintegration event leads to a detected NC event, the reconstructed vertex will be misleading. This scenario is unlikely to occur, however. If the $\gamma$ is from a background event, and the photodisintegration event leads to a detected NC event, it is counted as a true NC event incorrectly. Both situations are detrimental to the NC measurement. Photodisintegration in SNO occurs due to two nuclei, $^{208}Tl$ and $^{214}Bi$, both of which emit gammas above the NC interaction threshold. These nuclei occur as part of the uranium and thorium decay chains. Radon, which occurs in both chains, $^{208}Tl$ and $^{214}Bi$ all have short half lives and decay away on the scale of weeks or less. However, uranium and thorium have half lives on the order of millions of years. Contamination from $U$ and $Th$ will act as a constant source of $^{208}Tl$ and $^{214}Bi$ causing photodisintegration events. Radon and $U$ and $Th$ are discussed below.

#### Uranium and Thorium Chains

Many precautions have been taken to eliminate uranium ($U$) and thorium ($Th$). Any contamination due to these is permanent except possibly in the light and heavy water where it can be partially removed via chemical means (see Section 2.5). A calibration source has been developed to study this background and is described in Section 2.8.

#### Radon

Mine air contains radon, a naturally occurring radioactive element, at a concentration of $3pC/l$. A cover gas system has been developed to act as a buffer between the $H_2O$ and $D_2O$ and the mine air containing $Rn$. It is described in Section 2.5.

### A.4.3 Muons

The SNO site, at 6800 feet below ground and roughly 6 km of water equivalent, is very deep compared to most neutrino experiments. The muon flux is small at that depth. The estimated SNO muon event rate is roughly 3 events per hour. Most muons are through going and leave small areas of large charge at the PMTs near the entrance and exit points. The Cerenkov ring is extended because the muon is Cerenkov radiating along the entire trajectory through the detector. This geometrical information determines the direction of the muon. A study of muon events can aid in understanding the detector.

## A.5 SNO Physics

In the previous sections the SNO experiment was motivated and the signals and their backgrounds were described. This section describes the physics potential of SNO. The major motivation for SNO is to determine whether neutrino flavor mixing can account for the observed deficit of solar neutrinos. This is accomplished by measuring the Charged-to-Neutral Current ratio (CC/NC) and the $\nu_e$energy spectrum. Another important measurement is the day-night asymmetry of interaction rates. Each of these topics are discussed separately.

### The CC/NC Ratio

The CC/NC ratio will verify or refute the hypothesis that solar $\nu_e$oscillate to another active neutrino flavor ($\nu_\mu$, $\nu_\tau$or both). This measurement is virtually independent of total solar neutrino flux. The number of CC and NC events over a given time period are counted. The cross sections for each interaction are known as a function of energy to an accuracy of 5% and the uncertainty of CC/NC ratio due to the cross sections is 3%. From this information, and taking into account the measured efficiencies and detector angular and energy resolution, the $^8$B flux is determined. There are two general scenarios depending on what is occurring to the solar neutrinos.

(1) Both the CC and NC flux measurements are consistent with the flux measured by Kamiokande and Superkamiokande resulting in a CC/NC ratio of unity. This would imply that either the solar models are incorrect, neutrino oscillations to sterile neutrinos are occurring, or both.

(2) The flux obtained from the NC measurement is larger than that of the CC measurement leading to a CC/NC ratio less than unity. This would be direct evidence that neutrino oscillations between solar $\nu_e$and one or more active neutrino species is occurring. The NC flux would be the first measurement of the full solar neutrino flux from active neutrinos. A check on this result would be to calcualte the expected flux for the Kamiokande and Super-Kamiokande experiments given the fraction of electron neutrinos and active non-electron neutrinos obtained from the CC and NC measurements, with the total active neutrino flux obtained from the NC flux measurement.

**$\nu_e$Energy Spectrum**

The $\nu_e$energy spectrum using the CC interaction is the next most important thing SNO can measure. This crucial measurement is needed to help distinguish between the vacuum oscillation solutions, the small angle MSW solution and the large angle MSW solution. The small angle and vacuum oscillation solutions can have significant

$\nu_e$spectrum distortion while the LA solution does not [21, 88]. Hata *et. al.* [21] and others [88, 89, 90] have carried out detailed theoretical simulations of the SNO and Super-Kamiokande experiments including the effects of $\nu_e$spectrum distortions. Figures A.3 and A.4 show the expected distortions for 2 years of data in each experiment for a number of different solar neutrino problem solutions. Also shown are the statistical errors for the small angle solution over that time period. Energy resolution estimates from the experiments are included in the calculations but backgrounds are not. It is seen that all the solutions can be distinguished from this measurement alone assuming the *systematic* errors are of the order of the statistical errors or less and assuming a threshold near 5 MeV can be approached. This is true for both experiments.

Super-Kamiokande [70] has published their measurement of the $\nu_e$energy spectrum after 2 years of running. They have not been able to measure a $\nu_e$distortion of this kind. The spectrum is consistent with no distortions except for the last three bins at the highest energies. The last bin is a sum of all events above 14 MeV where the $^8$B signal contributes very little. The MSW distortions are most prominent at low energies and the errors are not small enough to detect it.

However, the distortion at high energies has caused speculation that perhaps *hep* neutrinos (see figure 1.1) are contributing much more than expected. This would require a much larger cross section, $S_{13}$, which has a large (in fact not even currently

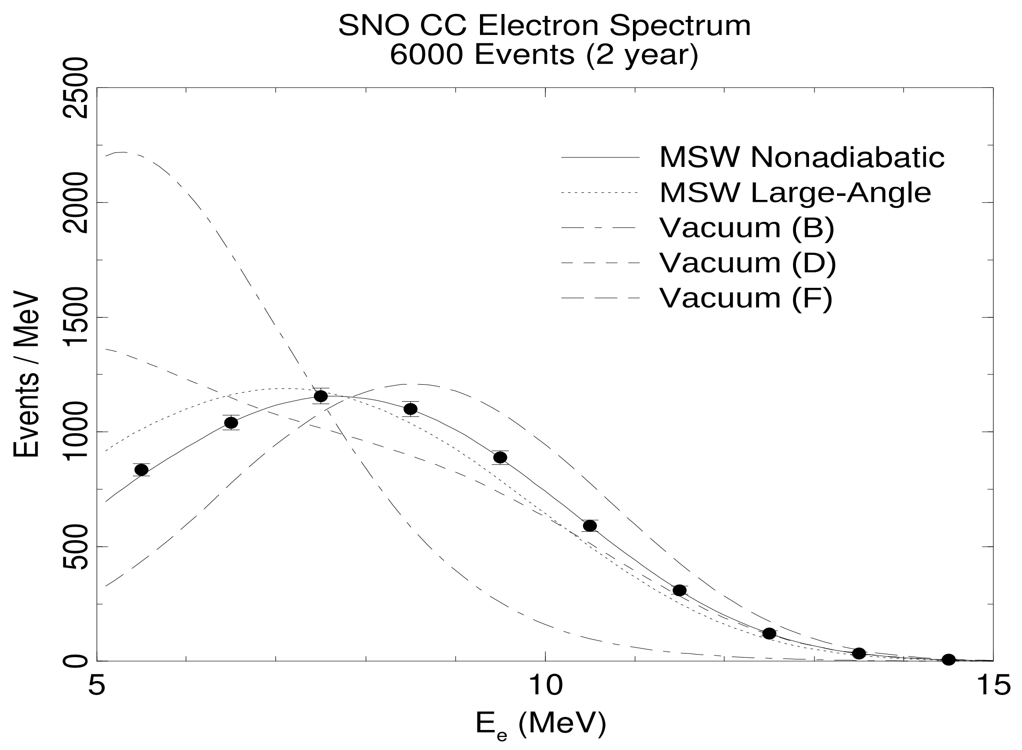


Figure A.3: SNO expected $\nu_e$spectrum distortion for various solar neutrino problem solutions [21]. (The author thanks N. Hata for the use of this figure.)

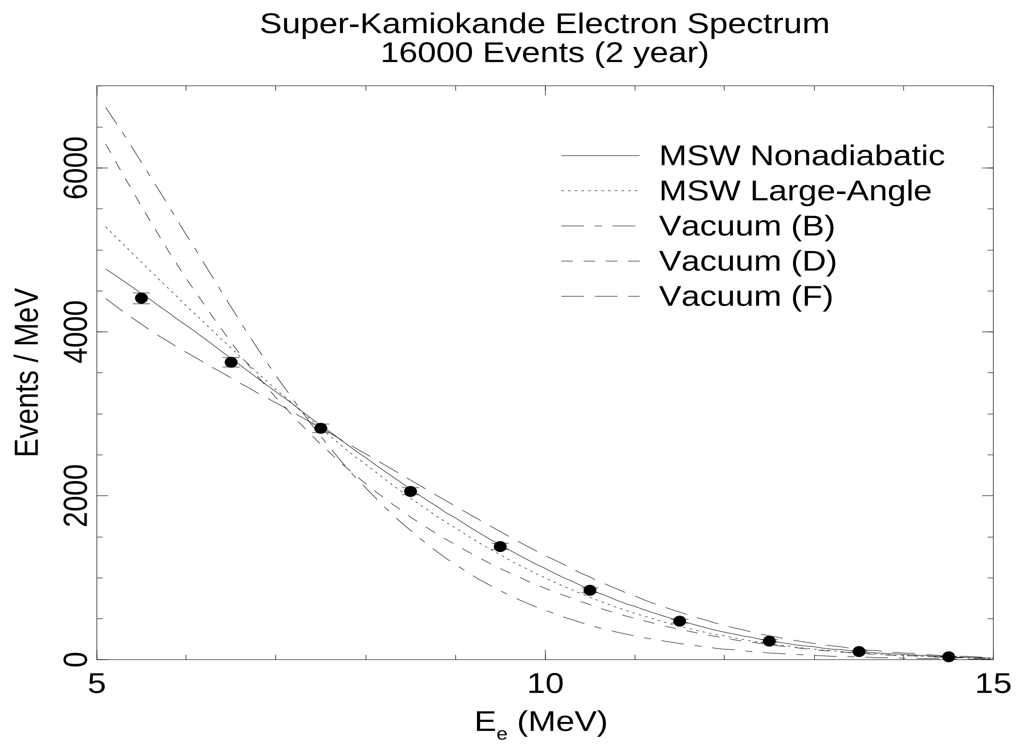


Figure A.4: SuperK expected $\nu_e$spectrum distortion for various solar neutrino problem solutions [21]. (The author thanks N. Hata for the use of this figure.)

estimated) uncertainty as of this writing. Bahcall *et. al.* [91] have recently done a calculation in which they allowed the hep flux to vary as a free parameter, while keeping all other fluxes fixed at their SSM values, and including MSW oscillations. The authors find that allowing the hep flux to increase by a factor of 20-30 yields significantly better fits to the SuperKamiokande energy spectrum compared to the same fits with the standard value of the hep flux. They state that there is no reason to believe the cross section could not be misestimated by as much as that.

**Day/Night Effect**

Consideration of matter oscillations in the sun leads one to consider if the same phenomenon can happen in the earth as well. In fact, when models of the electron density profile of the earth are considered and the calculations are done, certain regions of MSW parameter space show a measurable effect [92, 93]. The largest effect that is commensurate with all of the experiments is near the large angle MSW solution. In that regime the overall effect is that some of the solar $\nu_\mu$or $\nu_\tau$, which have come about through MSW oscillations in the sun, oscillate back into $\nu_e$as they traverse a large part of the earth. This effect is strongest at night and imperceptible during the day because of the insignificant distances traveled through matter by a neutrino during the day. This increase in the $\nu_e$flux at night (equivalently a decrease in the $\nu_\mu$or $\nu_\tau$flux) is known as the "earth effect" or "day/night effect" [92, 93]. Detailed analysis (not shown here) shows that both SNO and SuperKamiokande should be able to distinguish an increase in the $\nu_e$flux at night compared to the day if the large angle MSW solution is the correct one [93]. Both the Kamiokande and SuperKamiokande [94] experiments have done analyses in an attempt to measure a day-night asymmetry but failed to see an effect within statistical accuracy. However, some of the parameter space for MSW oscillations near the large angle solution can be excluded based on this result [93].

### A.6 Summary of SNO Physics

In the above sections, the motivation for the SNO experiment has been given. Physics signals, backgrounds and the physics potential have been described. The measurement of the CC and NC interactions together make SNO a unique neutrino experiment. In the absence of a sterile neutrino component to solar neutrino oscillations, the CC/NC ratio will provide unambiguous proof of the existence or non-existence of neutrino oscillations for solar neutrinos. Other physics investigations that can be done with SNO which have not been described are supernova and atmospheric neutrino studies. In the event of a nearby supernova, SNO will have a rich data set of all active species of neutrinos, the $\nu_e$and $\overline{\nu_e}$ energy spectra, and the relative timing of different neutrino types. This will place significant restrictions on supernova theories. A unique contribution to the study of atmospheric neutrinos is also possible.

# Appendix B

## The SNO PMT Interface and High Voltage System

This appendix describes the SNO PMT interface and high voltage system in detail. The system uses 20 high voltage(HV) power supplies to power 9522 inward looking and 91 outward looking PMTs in the SNO detector. A custom designed printed circuit board, the PMT interface card (PMTIC), provides the HV connection to the PMTs as well as accepting and terminating the PMT signal before passing it to the signal processing circuitry on the SNO front end card (FEC).

The design criteria of the entire system is presented in Section B.1. The PMTIC will be described in detail in Section B.2, including the HV path, PMT base current measurement circuitry, signal path, and charge injection circuitry. A custom designed HV distribution backplane, the high voltage backplane (HVBP), is the subject of Section B.3. The HV power distribution system is described including the architecture of the system in Section B.4. Special systems for outward looking PMTs (Section B.5), and low gain PMTs (Section B.6) are described. PMTIC testing procedures are given in Section B.7. Finally, the performance of the system is presented in Section B.8.

The SNO HV system was designed, built and tested, largely, by the author. However, it should be noted that much of the design work was performed by Rick Van Berg and the charge injection circuitry was designed by F. Mitch Newcomer. This project would not have been possible without their continued support and expertise throughout the project.

## B.1 Design Criteria

The design criteria for the SNO PMT Interface and High Voltage system are enumerated below. The sections that follow will describe how these criteria were implemented into the system.

**High Voltage:**

(1) Provide HV to all 9522 inward-looking and 91 outward-looking PMTs

(2) Operation of each PMT at $10^7$ gain; requires unique voltage for each PMT

(3) Input protection for front end circuitry

(4) Provide a high voltage interlock system for safety

(5) Provide maximum HV switching resolution balanced against cost

**PMT Signal:**

(1) PMT Cable interface and signal acceptance

(2) Impedance matching physical termination of PMT cable

(3) Deliver clean, low noise signal to front end circuitry

**Charge Injection System:**

(1) Provide charge injection capability for each channel

(2) Externally selectable: one, or any combination of channels at a time

(3) Large dynamic range: 0-100 pe, externally controllable

**PMT Base Current Readout:**

(1) Provide a measurement of the PMT base current for each channel

(2) Externally selectable: one channel at a time

**Outward Looking PMTs:**

(1) Conform to the constraint that outward looking PMTs use separate trigger lines

**Low Gain Channels:**

(1) Provide separate coupling for the dynode tap signals on the 49 low gain channels

**Other Issues:**

(1) Single cable system: HV and signal on one coaxial cable

(2) Conform to the geometrical layout of the electronics crate and other electronics boards

(3) Conform to the geometrical layout of the electronics racks on the SNO detector deck

(4) Provide robust anchoring of PMT cables - cables are extremely stiff

(5) Capability of switching HV with no FEC attached to PMTIC

(6) Install a board ID chip on each PMTIC which is externally selectable and readable and has a unique identification number

(6) Minimization of complexity and cost

## B.2 PMT Interface Card (PMTIC)

Each PMT interface card (PMTIC) provides the capability of connecting to 32 PMTs, delivering HV to them, accepting and terminating the signals, and passing the signals to the front end circuitry for processing. Furthermore, each of the 32 channels has programmably selected circuitry for reading the PMT base current (with limited resolution), and for injecting a pulse of charge into the signal path simulating a PMT pulse. Each channel acts as an independent system. There are approximately 300 PMTICs in use in the SNO detector at a given time connected to 9522 inward looking and 91 outward looking PMTs. Each PMTIC has a unique identification number (Board ID) programmed into a PROM chip located on the PMTIC with address and data lines enabling access by an external computer. This ensures that the PMTIC is in the correct location - they are not fully identical as will be described below.

**Connectors and Connections**

Each PMTIC has a 12 pin central connector, which connects to the high voltage backplane (HVBP), and two 96 pin connectors which connect to the associated front end card (FEC). The central connector provides the HV signal and some digital switching signals for HV control. The 96 pin connectors are for the 32 (analog) channels of PMT signals, and some digital switching signals for the charge injection and PMT base current measurement circuits. The PMT cables connect to The PMTIC via four paddlecards with eight channels each. This system provides a strong, robust connection and allows the cables to be removed when the PMTICs need servicing. Afterward they are easilly replaced. The paddlecards have an internal ground layer in a mesh-like arrangement. The ground layer is connected to a the paddlecard's 24 pin connector providing three ground pins for each channel. The outer shield of the PMT coaxial cable is also connected to this 24 pin connector defining PMT ground.

The center conductor of the cable connects to an 8 pin connector on the paddlecard. This conductor carries both the PMT signal and the high voltage. The 8 and 24 pin connectors of the paddlecards connect to mating connectors on the PMTICs and four plastic fittings anchor the paddlecard to the PMTIC allowing little movement. For extra strength, each PMTIC has a rigid $3/4 \times 1 \times 16$ inch aluminum bar attached to the rear of the PMTIC with screws directly connected to the PMTIC ground planes. Groups of eight cables are clamped to this bar (and therefore the PMTIC) providing extra resistance to cable movement which can degrade the PMT connection. The aluminum bars are then screwed into the crate providing not only extra strength, but also a good ground connection from the crate to the PMTIC ground planes. Such a connection was found experimentally to minimize pickup from ambient sources.

### DC Voltages

The PMTIC is a six layer circuit board. It has routing layers on the top and bottom surfaces, while two ground planes and two power plane make up the internal layers. The power planes are the innermost layers and the ground planes provide shielding between them and the two surface layers which carry the analog PMT signals. The DC voltages ($V_{cc}$=+5V, $V_{EE}$=-5.2V, and $\pm$15V) for powering most of the active electronic components come from the FEC via the two 96 pin connectors and are distributed to the components via large, isolated conducting surfaces on the power plane layers.

The shapes of the ground plane conducting surfaces were designed to maximize the path length of any pickup currents from analog signal lines to digital signal lines. Seperate $V_{cc}$ and ground level signals come from the HVBP across the 12 pin central connector, supplying only the HV switching circuitry. This separate system is used in case it is desired to look at PMT signals while the associated FEC is not connected. There is a special board designed for this purpose which connects to the PMTIC in place of the FEC and has a BNC connector for each PMT channel. The raw PMT signal from each PMT can be seen by connecting to an oscilloscope.

### B.2.1 High Voltage Path

The PMTIC accepts high voltage (HV) via a 12 pin connection to the HV backplane (described below). It passes through a filtering circuit and is delivered to four programmably selected relays, one relay for each paddlecard. A large value ($> 200k\Omega$) resistor couples the HV to each channel of PMTIC signal connector. HV switching is possible for each paddlecard *i.e.* for groups of eight PMTs. This limitation is influenced by both cost and size considerations. However, further, albeit cruder resolution is possible by installing or removing external resistors in series with the HV signal for each channel. This requires shutting down the HV system and removing the PMTIC. In practice, this is done only when a PMT fails and is no longer usable.

Each PMTIC has 32 resistors ($R_{channel}$) in series with the HV signal of each channel, 4 resistors ($R_{paddlecard}$) in series with the HV signal from each relay (*i.e.* for each paddlecard), and 1 resistor ($R_{slot}$) in series with the HV for all channels on the PMTIC. The latter resistor is part of the aforementioned filter circuit. The values of these resistors are customized to provide the specific $10^7$ gain voltage for the PMT connected to a given channel. The distribution of the $10^7$ gain voltages is between 1600V and 2500V with a mean of approximately 2000V. A set of computer programs were written by the author to calculate the resistor values once the $10^7$ gain voltages of each PMT and the mapping of PMTs to channels was known. This is a complex task with only one or two HV supplies per crate (16 PMTICS) to work with. From time-to-time, PMTs may be switched from one channel to another, requiring recalculation of that channel resistor ($R_{channel}$). A table of the resistor values and $10^7$ gain voltages for each electronics channel is in a red binder at the SNO detector site and is available in a central directory of the Penn SNO group computer system.

A 4.7nF, 2000V capacitor on each channel is used to decouple the HV from the signal. They are only rated for 2000V but in practice can handle at least a factor of two higher voltage. The relays used are rated for 3500V.

All of the surfaces near the HV signal on the PMTIC were coated with conformal coating in order to prevent surface breakdown. The coating, in liquid form, was painted on. The entire PMTIC was baked in an oven before and after the coating was put on. Before to bake off excess moisture on the PMTIC and after to help seal the coating to the G10 surface. All PMTICs which passed HV testing were able to withstand at least 2500V, and as much as 3500V for some boards, for a sustained period of time without any breakdowns. PMTICs with relatively low breakdown voltages were used in slots with low supply voltages and all PMTICs have operating voltages of at least 700V less than their breakdown voltages.

### B.2.2 PMT Base Current

A circuit is provided on each channel for reading the PMT base current. The outer conductor (braid) of the PMT coaxial cable is connected to ground via a 100Ω resistor. The voltage across this resistor is proportional to the base current. This signal for each channel is delivered to one input of a 32 channel multiplexer which can be programmably selected by external computer. The output of the multiplexer is converted to a digital value and is stored in a single register on the associated FEC. This register can then be read out by computer. The channel currents can therefore be read one at a time per PMTIC.

The resolution of the circuit is poor due to the small signals involved. The voltage across the resistor is (for a typical PMT base current of $140\mu A$): $\sim 140\mu A\ /100\Omega \sim 1.4\mu V$. To distinguish changes in this small voltage requires the ability to detect changes in fractions of mV. In practice, the system is used as a binary indicator of whether a PMT is functioning or not.

### B.2.3 Signal Path

Aside from HV decoupling, the input circuit consists of: input protection diodes on the signal and ground lines, 75Ω impedance matching, and a 1:1 isolation transformer. The input protection assures that high voltage breakdowns, either on the PMT base or on the PMTIC, don't damage the front end circuitry on the FEC. The isolation transformers, obtained at low cost, have imperfect turns ratio. That is the ratio is not exactly 1:1. This manufacturers defect was not realized until after the purchase had been made and the time constraints at that point made it undesirable to reject the transformers and wait for another production run. The results are: slightly imperfect impedance matching (*i.e.* not exactly 75Ω), and a small decrease in the value of the integrated charge over time. The approximate drop is 7% in 400 ns. This effect has been calibrated and corrected for.

After the isolation transformer, the signal passes through connectors to the FEC. The physical etches on the PMTIC which carry these signals have been carefully routed for impedance matching and maximum isolation. Care was taken to match the impedance between the signal layers and the ground layers to the 75Ω impedance of the PMT signal cables. Separate ground etches run parallel to the signal etches on either side of them to further isolate each channel from each other. Furthermore, all digital switching lines are routed well away from these analog signal lines as much as possible, especially near the connector which both are connected to.

### B.2.4 Charge Injection

Each PMTIC channel contains a programmably selected and controllable circuit capable of injecting a pulse of charge into the signal path. The injection can be done for any combination of channels simultaneously. Both the width and amplitude of the pulse are programmable with a dynamic range of $\sim 0-80$pC. This is equivalent to $\sim 0-100$ photoelectrons given the $10^7$ gain of the PMTs and considering the factor of two loss due to back termination of the PMT cable.

The circuit consists of a bipolar differental pair of transistors, acting as a switch. A current mirror circuit provides programmable control of the amplitude while the pulse width is set by setting the width of the "pedestal" pulse on the Master Trigger/Digital card (MTC/D). Integrated charge is proportional to changes in the amplitude as well as the pulse width.

Charge injection is used to check for faulty electronics channels, to do electronics time slope calibrations, and to check the linearity of the charge integration system on the front end. The absolute charge injected is known fairly well. However, the charge calibration is not done using this system. Instead, it is done using a light source at varying intensities. The time slope calibrations are accomplished by injecting charge synchronous with the pedestal pulse, and varying the delay between the beginning of the pedestal pulse and the global trigger. Similarly, the charge slope calibration is done by injecting charge over most of the dynamic range. These tasks are done periodically (every hour or so) on every channel in the system. Many channels can be calibrated simultaneously.

### B.3 High Voltage Backplane (HVBP)

A custom made backplane, the High Voltage Backplane (HVBP), was designed, to provide connectivity betweem the PMTICs and the HV supplies, and to deliver digital switching signals for switching the PMTIC relays. Each HVBP has two separate HV supply paths. In many of the crates, one supply is used and zener diodes are connected between paths to provide the second voltage. This reduces the number of supplies required by a factor of two. Both of the HV inputs have a filter circuit. There is one 4 pin connector which connects to one or two SHV connectors mounted at the rear of the crate which the HV supply (or supplies) are connected to. The HVBP has 16 twelve pin connectors to mate with each PMTIC center connector. The HV and HV return pins of these connectors can be connected to either HV input via external jumpers. The HVBP is attached in “piggyback” to the SNOBUS backplane. Half inch standoffs screw into the SNOBUS backplane and provide mouting screws for the HVBP. A layer of Kapton over the entire face of the HVBP nearest the SNOBUS backplane provides extra HV shielding. This configuration was tested with 4kV on the HVBP for three hours without a single breakdown.

## B.4 HV Power Distribution and Architecture

Digital switching information is transferred from the timing rack VME crate through the XL1 and XL2 translator cards to the HVBP. An external computer communicating with the XL2 shifts switching signals, via buses on the HVBP, serially through registers on each PMTIC and out to the adjacent one. When the correct PMTIC is reached, a separate load bit loads the local HV control register switching the relays for that PMTIC. The system can operate as few as one or as many as all 64 relays in the crate with a single operation. The DAQ system also acts as a control system for the HV supplies. The information for turning on the supply, ramping up the voltage as well as monitoring the HV value is passed to the HV supply via a cable from the XL2 card. Each crate has its own PMT high voltage (HV) supply and there is a separate supply for the 91 outward looking (OWL) PMTs, for a total of 20 HV supplies. The supplies are fully controlled by external computer allowing switching, ramping of voltage, and readout of the supply voltage and current. There are three read or read/write registers on the XL2 for these purposes. A HV interlock system is in place for each crate individually. There is a +5V signal sent from the crate's XL2 to its HVBP. Plugging a PMTIC into the HVBP completes part of the chain and sends the +5V signal to the adjacent PMTIC. If all 16 PMTICs are plugged in, or special jumpers are used in their place, the entire chain is complete back to the XL2 and an enable signal is sent from the XL2 to the HV supply for that crate. If the chain is not complete, no enable signal is sent and the HV supply cannot be turned on. If a PMTIC is removed while the HV is on, the enable signal is removed (disabled) and the HV supply automatically and immediately shuts off. Thus a worker who accidentally removes a PMTIC cannot get a shock from HV. The special jumpers are necessary for two reasons. First, not all crates require 16 PMTICs. Second, when debugging a HV problem on a PMTIC, it is often necessary to remove the adjacent PMTICs to give room to probe. Care must be taken when operating this way and only qualified personnel should attempt it. The jumpers are modified versions of the PMTIC central 12 pin connector. Two sets of pins are soldered together: the pins which complete the interlock signal, and the pins which move the digital HV switching selection signal. Care must be taken to install the jumpers with the correct polarity.

### B.5 Outward Looking PMTs

The outward looking PMTs (OWL) use separate trigger lines. These lines are assigned to slot 15 in four crates (Crates 3, 13, 17 and 18). All of the OWL PMT cables are grouped together on three PMTICs in slot 15 of crates 3, 13 and 18 (Crate 17 is used for calibration devices). There are 91 OWL PMTs so the 96 channels available on these three PMTICs are sufficient, with a few spare channels in case some are damaged over the course of the experiment. The OWL PMTs are all powered from a single HV supply which resides in rack 6, a single crate rack with crate 16 in it.

This enables easy rampdown of the outer detector independent of the inner detector and vice versa. In order to implement this, the output of the OWL HV supply is split and long SHV cables are run from rack 6 to the three crates with OWL PMTs. The HV interlock system does not function properly for the OWL HV supply. When an OWL PMTIC is removed on one of the three OWL crates, the HV supplies in that crate are automatically shut off as usual. However, the OWL HV supply is *not* shut off and there is still HV from this supply on the HVBP of the OWL crate. The same situation occurs if one of the non-OWL PMTICs in an OWL crate is removed. Finally, if one of the PMTICs in crate 16 is removed, the OWL HV supply is shut off automatically even though that supply is not connected to crate 16.

### B.6 Low Gain PMT Channel Modification

Some 49 PMTs in the SNO detector have dynode taps which read the PMT signal at the 2nd dynode. These taps go to separate channels which are called low gain channels. Each of these 49 special PMTs has a normal and low gain channel associated with it. The low gain channels require special modifications in the PMTIC coupling circuitry. First, these channels don't have high voltage so the HV signal paths and the HV decoupling capacitor have been removed. Second, the polarity of the PMT pulse is reversed in such a configuration. To correct for this, the signal and return lines on the PMTIC were crossed with external wires. Finally, the transformer was removed since it is unnecessary. The low gain signals will be used to extend the dynamic range of the detector for rare, extremely energetic events (not due to solar neutrinos).

## B.7 Testing

### B.7.1 PMTIC Testing

Testing of the PMTIC was done half at TRIUMF in Van Couver, British Columbia and half at the SNO site. The process was organized in the following manner:

(1) Visual inspection

(2) Digital component testing

(3) Conformal coating process

(4) External resistor stuffing

(5) HV testing

(6) Repair

Checklists were used at various stages of the process and a system of keeping track of which PMTICs were at which stage was devised. The entire process took approximately 6 months from start to finish.

The visual inspection stage was done board by board using a microscope as well as the unaided eye. Approximately ten to fifteen minutes was alloted per board not counting any required repairs. A group of testing scripts were written by James Beck, then of the University of Washington, to automate the digital component testing. When optimized, the test of all the digital systems required approxmately 10 minutes for one PMTIC. The results of the digital test for each PMTIC were generated automatically and hardcopies are available in binders at the SNO site. The conformal coating process has been described above. External resistors had to be stuffed by hand. This laborious task was further hampered by the care needed to make sure the custom resistor values were in the correct locations.

HV testing was the most time consuming and difficult part of the process. Imperfections in the conformal coating and unclean surfaces sometimes caused external breakdown. The process of installing PMTICs in a crate, ramping up the HV, waiting for ten minutes at full test voltage, and ramping down was time consuming, especially when a breakdown occured. Tests of the PMT base current digital system were done at this stage and required installing external resistors for each channel. This process, although the measurement part of it was computer automated, was also very time consuming. Repairs of faulty PMTICs was yet another time consuming task and made the logistics of keeping track of the PMTICs difficult.

The author would like to express a warm thanks to Barry and Peter from Oxford University, and especially Rich Helmer (and his team at TRIUMF), Sid Barry and Karin Hayward of Sudbury, Ontario for their help in PMTIC testing. Without their

help, it never would have been completed and I am forever in their debt.

### B.7.2 System Testing

Once the PMTICs were tested, they were installed in their correct locations in the crates. Once the testing of the other electronics caught up, an entire crate of electronics was tested extensively. This was done above ground at the SNO site. A set of software routines organized by the Penn SNO group spearheaded by Paul Keener, was used to perform these tests. This was the first point at which PMTs were used in the testing, but few channels were tested with PMTs at this point. A few PMTICs which had passed the entire test process were found to be faulty at this stage and repairs had to be made. Once the entire crate (actually rack) of electronics was tested, it was sent underground to be installed.

## B.8 PMTIC and HV System Performance

The entire HV system, with 20 HV supplies and 304 PMTICs, has been in use at the SNO site for over a year. With the exception of routine maintenance and a few blown components, there have been no problems with the system. During the past year, the HV has been ramped up and down a large number of times as other systems of the SNO detector required attention. The operating voltage was set to 200V above the original $10^7$ gain voltage (for many of the crates) for part of this time. This kind of operation stresses the system far more than ramping up to HV and leaving it there for months at a time as in normal operation. The system has proven to be quite robust and is operating according to design.

# Bibliography


[1] K. Wenninger, S. J. Putterman, and B. P. Barber, *Angular correlations in sonoluminescence: Diagnostic for the sphericity of a collapsing bubble*, Phys. Rev. E **54**, 2205 (1996).

[2] C. Slotta and U. Heinz, *Resolving the space-time structure of sonoluminescence by intensity interferometry*, Phys. Rev. E **58**, 526 (1998).

[3] J. K. Rowley, B. T. Cleveland, and R. Davis, in *Solar Neutrinos and Neutrino Astronomy*, edited by M. L. Cherry, W. A. Fowler, and K. Lande (American Institute of Physics, New York, 1985), Vol. 126.

[4] K. S. H. *et. al.*, —, Phys. Rev. **D44**, 2241 (1991).

[5] P. A. *et. al.*, —, Phys. Lett. **B285**, 376 (1992).

[6] A. I. A. *et. al.*, —, Phys. Rev. Lett. **67**, 3332 (1991).

[7] Y. Totsuka, in *Proceedings of Seventh Workshop on Grand Unification, ICOBAN '86*, edited by J. Arafune (World Scientific, Singapore, 1987).

[8] H. Frenzel and H. Schultes, —, Z. Phys. Chem. **B27**, 421 (1934).

[9] D. F. Gaitan, *Ph.D. Thesis*, Ph.D. thesis, University of Mississippi, 1990.

[10] D. F. Gaitan, L. A. Crum, C. C. Church, and R. A. Roy, —, J. Acoust. Soc. Am. **91**, 3166 (1992).

[11] R. Davis, —, Phys. Rev. Lett. **12**, 303 (1964).

[12] J. N. Bahcall and R. K. Ulrich, —, App. J. Lett. **160**, L57 (1970).

[13] J. N. Bahcall, *Neutrino Astrophysics* (Cambridge University Press, Cambridge, 1989).

[14] J. N. Bahcall and R. K. Ulrich, —, App. J. **170**, 593 (1971).

[15] D. D. Clayton, *Principles of Stellar Evolution and Nucleosynthesis* (The University of Chicago University Press, Chicago, 1968).

[16] H. A. Bethe, —, Phys. Rev. **55**, 434 (1934).

[17] J. N. Bahcall, S. Basu, and M. H. Pinsonneault, —, Phys. Lett. **B433**, 1 (1998).

[18] I. R. B. *et. al.*, in *Solar Neutrinos and Neutrino Astronomy*, edited by M. L. Cherry, W. A. Fowler, and K. Lande (American Institute of Physics, New York, 1985), Vol. 126.

[19] T. Kirsten, —, Inst. Phys. Conf. Ser. **71**, 251 (1984).

[20] K. S. H. *et. al.*, —, Phys. Rev. Lett. **65**, 1297 (1990).

[21] N. Hata and P. Langacker, *Solutions to the Solar Neutrino Anomaly, Spring 1997*, Phys. Rev. **D56**, — (1997).

[22] J. N. Bahcall and W. C. Haxton, —, Phys. Rev. D **55**, 1 (1989).

[23] J. N. Bahcall, S. Basu, and M. N. Pinsonneault, *How Uncertain Are Solar Neutrino Predictions?*, Phys. Lett. **B433**, 1 (1998).

[24] S. B. *et. al.*, —, Nucl. Phys. **B374**, 373 (1992).

[25] V. C. *et. al.*, —, Astrophys. J. **402**, 574 (1993).

[26] H. *et. al.*, —, Phys. Lett. B **388**, 384 (1996).

[27] A. *et. al.*, —, Phys. Rev. Lett. **77**, 4708 (1997).

[28] W. K. Kwong and S. P. Rosen, —, Phys. Rev. Lett. **73**, 369 (1994).

[29] N. Hata, S. Bludman, and P. Langacker, —, Phys. Rev. **D49**, 3622 (1994).

[30] T. Kajita, *Atmospheric neutrino results from Super-Kamiokande and Kamiokande - Evidence for $\nu_\mu$ oscillations*, Preprint hep-ex/9810001 —, — (1998).

[31] V. Barger, K. Whisnant, S. Pakvasa, and R. J. N. Phillips, —, Phys. Ref. D **22**, 2718 (1980).

[32] V. Barger, R. J. N. Phillips, and K. Whisnant, —, Phys. Ref. D **34**, 980 (1986).

[33] P. Langacker, S. T. Petcov, G. Steigman, and S. Toshev, —, Nucl. Phys. **B282**, 589 (1987).

[34] L. Wolfenstein, —, Phys. Rev. D **17**, 2369 (1978).

[35] L. Wolfenstein, —, Phys. Rev. D **20**, 2634 (1979).

[36] H. A. Bethe, —, Phys. Rev. Lett. **56**, 1305 (1986).

[37] S. J. Parke, —, Phys. Rev. Lett. **57**, 1275 (1986).

[38] W. C. Haxton, —, Phys. Rev. Lett. **57**, 1271 (1986).

[39] S. T. Petcov, —, Phys. Lett. **B191**, 299 (1987).

[40] S. P. Mikheyev and A. Y. Smirnov, —, Sov. J. Nucl. Phys. **42**, 913 (1986).

[41] X. Shi, D. N. Schramm, and J. Bahcall, —, Phys. Rev. Lett. **69**, 717 (1992).

[42] P. I. Krastev and S. T. Petcov, —, Phys. Lett. **B299**, 99 (1993).

[43] W. Richards and A. Loomis, *The Chemical Effects of High Frequency Sound Waves I. A Preliminary Survey*, J. Am. Chem. Soc. **49**, 3086 (1927).

[44] F. Schmitt, C. Johnson, and A. Olson, *Oxidations Promoted by Ultrasonic Radiation*, Am. Chem. Soc. **51**, 370 (1929).

[45] Mecke (unpublished).

[46] L. Crum and G. Reynolds, *Sonoluminescence Produced by 'Stable' Cavitation*, J. Acoust. Soc. Am. **78**, 137 (1985).

[47] R. Hiller, S. J. Putterman, and B. P. Barber, —, Phys. Rev. Lett. **69**, 1182 (1992).

[48] D. F. Gaitan, A. A. Atchley, S. D. Lewis, J. T. Carlson, X. K. Maruyama, M. Moran, and D. Schweider, —, Phys. Rev. E **54**, 525 (1996).

[49] B. P. Barber and S. J. Putterman, —, Phys. Rev. Lett. **69**, 3839 (1992).

[50] B. P. Barber, R. A. Hiller, R. Lofstedt, S. J. Putterman, and K. R. Wenninger, *Defining the Unknowns of Sonoluminescence*, Phys. Rep. **281**, 65 (1997).

[51] B. Gompf, R. Gunther, G. Nick, R. Pecha, and W. Eisenmenger, *Resolving Sonoluminescence Pulse Width with Time-Correlated Single Photon Counting*, Phys. Rev. Lett. **79**, 1405 (1997).

[52] R. Hiller, S. J. Putterman, and K. R. Wenninger, *Time-Resolved Spectra of Sonoluminescence*, Phys. Rev. Lett. **80**, 1090 (1998).

[53] M. J. Moran and D. Sweider, *Measurements of Sonoluminescence Temporal Pulse Shape*, Phys. Rev. Lett. **80**, 4987 (1998).

[54] J. D. N. Cheeke, *Single-bubble sonoluminescence: 'bubble, bubble, toil and trouble'*, CAn. J. Phys. **75**, 77 (1997).

[55] C. C. Wu and P. H. Roberts, —, Phys. Rev. Lett. **70**, 3424 (1993).

[56] B. P. Barber, *Synchronous Picosecond Sonoluminescence*, Ph.D. thesis, University of California - Los Angeles, 1992.

[57] R. L. K. Wenninger, S. J. Putterman, and B. P. Barber, —, Phys. Rev. E **51**, 4400 (1995).

[58] J. Schwinger, —, Proc. Nat. Acad. Sci. **89**, 4091 (1992).

[59] J. Schwinger, —, Proc. Nat. Acad. Sci. **90**, 958 (1993).

[60] J. Schwinger, —, Proc. Nat. Acad. Sci. **91**, 6473 (1994).

[61] S. Liberati, F. Belgiorno, M. Visser, and D. W. Sciama, *Sonoluminescence as a QED vacuum effect*, submitted preprint: quant-ph/9805031 —, — (1998).

[62] C. E. Carlson, C. Molina-Paris, J. Perez-Mercader, and M. Visser, —, Phys. Lett. **B395**, 76 (1997).

[63] C. E. Carlson, C. Molina-Paris, J. Perez-Mercader, and M. Visser, —, Phys. Rev. **D56**, 1262 (1997).

[64] K. Milton and J. Ng, *Casimir energy for a spherical cavity in a dielectric: Applications to Sonoluminescence*, submitted preprint: hep-th/9607186 —, — (1996).

[65] I. H. Brevik, V. V. Nesterenko, and I. G. Pirozhenko, *Direct mode summaation for hte Casimir energy of a solid ball*, submitted preprint: hep-th/9710101 —, — (1997).

[66] C. Eberlein, *Sonoluminescence as quantum vacuum radiation*, Phys. Rev. Lett. **76**, 3842 (1996).

[67] C. Eberlein, *Theory of quantum radiation observed as sonoluminescence*, Phys. Rev. A **53**, 2772 (1996).

[68] T. S. Collaboration (unpublished).

[69] R. Ford, —, Ph.D. thesis, Queens University, 1998.

[70] Y. F. *et. al.* The Super-Kamiokande Collaboration, *Measurement of the Solar Neutrino Energy Spectrum Using Neutrino-Electron Scattering*, preprint to be published —, — (1998).

[71] R. H. Brown and R. Q. Twiss, *A new type of interferometer for use in radio-astronomy*, Phil. Mag. **45**, 663 (1954).

[72] R. H. Brown, *The Intensity Interferometer, its Application to Astronomy* (Taylor Francis Ltd., London, 1974).

[73] D. Lohse, M. P. Brenner, T. F. Dupont, S. Hilgenfeldt, and B. Johnston, *Sonoluminescing Air Bubbles Rectify Argon*, Phys. Rev. Lett. **78**, 1359 (1997).

[74] R. Ford, Private Communication.

[75] A. A. Michelson and F. G. Pease, *Measurement of the diameter of $\alpha$ Orionis with the interferometer*, Astrophys. J. **53**, 249 (1921).

[76] L. Mandel and E. Wolf, *Progress in Optics* (North-Holland, Amsterdam, 1963).

[77] R. H. Brown, R. Davis, and L. R. Allen, *The angular diameters of 32 stars*, Mon. Not. R. astr. Soc. **167**, 121 (1974).

[78] F. M. Newcomer, Private Communication.

[79] F. M. Newcomer and R. V. Berg, *A Wide Dynamic Range Integrator-Discriminator-Timer Chip Set for PMT Applications*, IEEE Nuclear Science Symposium, Transactions on Nuclear Science **42**, 925 (1995).

[80] M. D. Lay, *Creaation and Detection of Cerenkov Light in the Sudbury Neutrino Observatory*, Ph.D. thesis, Oxford University, 1994.

[81] T. S. Collaboration (unpublished).

[82] W. A. Zajc, in *Hadronic Multiparticle Pruduction*, edited by P. CARRUTHERS (World Scientific Press, —, 1987).

[83] K. Fialkowski, R. Wit, and J. Wosiek, *The Bose-Einstein effect in Monte Carlo generators: weight methods*, preprint to be published: hep-ph/9803399 —, — (1998).

[84] H. H. Chen, —, Phys. Rev. Lett. **55**, 1534 (1985).

[85] W. Nelson, H. Hirayama, and D. W. O. Rogers, *The EGS4 Code System*, SLAC Report 265 —, — (1985).

[86] E. Browne, J. M. Dairiki, and R. E. Doebler, *Table of Isotopes, 7th Edition* (John Wiley and Sons, Inc., New York, 1978).

[87] S. J. Brice, —, Ph.D. thesis, Oxford University, 1996.

[88] J. N. Bahcall, P. I. Krastev, and E. Lisi, *Neutrino Oscillations and Moments of Electron Spectra*, Phys. Rev. **C55**, 494 (1997).

[89] S. P. Mikheyev and A. Y. Smirnov, —, Yad. Fiz. **42**, 1441 (1985).

[90] S. P. Mikheyev and A. Y. Smirnov, —, Sov. J. Nucl. Phys. **42**, 913 (1986).

[91] J. N. Bahcall and P. I. Krastev, *Do* hep *neutrinos affect the solar neutrino energy spectrum?*, preprint to be published —, — (1998).

[92] A. J. Baltz and J. Weneser, —, Phys. Rev. **D35**, 528 (1987).

[93] N. Hata and P. Langacker, —, Phys. Rev. **D48**, 2937 (1993).

[94] K. S. H. *et. al.*, —, Phys. Rev. Lett. **66**, 9 (1991).